Vol. 2 No. 1 (2022): ENP Engineering Science Journal

DOI: https://doi.org/10.53907/enpesj.v2i1

Power Transformer Fault Prediction using Naive Bayes and Decision tree based on Dissolved Gas Analysis

Yassine Mahamdi, Ahmed Boubakeur, Abdelouahab Mekhaldi, and Youcef Benmahamed

Abstract− Power transformers are the basic elements of the power grid, which is directly related to the reliability of the electrical system. Many techniques were used to prevent power transformer failures, but the Dissolved Gas Analysis (DGA) remains the most effective one. Based on the DGA technique, this paper describes the use of two of the most effective machine learning algorithms: Naive Bayes and Decision Tree for the identification of power transformer's faults. In our investigation, 9 different input vectors have been developed from widely known DGA techniques. 481 samples have been used and 6 types of faults have been considered. The evaluation result of the implementation of the proposed methods shows an effectiveness of 86.25% in power transformer's fault recognition.

***Keywords*− Decision Tree, Naive Bayes, DGA, Input vectors, Power transformer faults, Accuracy rate.**

NOMENCLATURE

DGA	Dissolved Gas Analysis
DT	Decision Tree
NB	Naive Bayes
PD	Partial Discharges
D1	Low Energy Discharges
D2	High Energy Discharges
T1	Thermal Faults < 300 °C
T2	Thermal Faults of 300 °C to 700 °C
T3	Thermal Faults > 700 °C

I. INTRODUCTION

The Dissolved Gas Analysis (DGA) is the most common and effective method for detecting transformer faults [1]. It can immediately prevent internal transformer failures, which generally avoids huge economic losses. The DGA uses the values of the concentrations of the various gases released in the transformer oil due to the decomposition of the oil and the insulating paper.

In-service transformer is exposed to two types of stresses: electrical and thermal [2]. Due to these stresses, the transformer oil and paper decompose, releasing a set of gases that reduce their dielectric strength. The nature and quantity of each dissolved gas produced in transformer oil can indicate the internal condition of the transformer.

The most common gases produced by the decomposition of oil are: ethane (C2H6), ethylene (C2H4), acetylene (C2H2), methane (CH4) and hydrogen (H2) [3-4]. In addition to carbon dioxide (CO2) and carbon monoxide (CO) that are formed as a result of the decomposition of the insulating paper [5-6], while, the nitrogen (N2) and the Oxygen (O2) are the non-fault gases.

Manuscript received October 22, 2021; revised December 29, 2021.

Y. Mahamdi, A. Boubakeur, A. Mekhaldi, and Y.Benmahamed are with Ecole Nationale Polytechnique (e-mail: yassine.mahamdi@g.enp.edu.dz, ahmed.boubakeur@g.enp.edu.dz, abdelouahab.mekhaldi@g.enp.edu.dz, youcef.benmahamed@g.enp.edu.dz).

Digital Object Identifier (DOI): 10.53907/enpesj.v2i1.63

The main three conditions that can cause gas generation in a transformer are:

1) Corona (partial discharge)
2) Thermal heating
3) Arcing

These differ mainly in the intensity of the energy that is dissipated by the default [2], [7].

There are many approaches developed for the analysis of dissolved gases in transformer oil and interpret their meaning including IEC Ratios, DORNENBURG Ratios, Rogers Ratios, Duval Triangle and Pentagon, and, Key Gas method [2], [7-10]. However, these techniques have certain limitations such as the existence of non-decision areas and erroneous results [11-12]. To overcome this situation, several artificial intelligence techniques have been used to improve the diagnostic accuracy of power transformers.

Recently, intelligent methods, such as fuzzy logic inference systems [13], artificial neural networks [4], [14-15], support vector machines (SVM) [16-19], K-nearest neighbors [16], [20], Bayesian neural networks [21], hybrid grey wolf optimization technique [5], and some other machine learning algorithms have been applied to diagnosis the power transformer faults and have impressive performances [22-24].

In this paper, the Naive Bayes and the Decision Tree algorithms were used in faults identification. The originality comes from the introduction of several input vectors. These input vectors have been constructed using widely known DGA techniques, so that the most suitable input data that gives the best performance of each algorithm and achieves the best prediction of fault in power transformers can be identified.

This article is arranged as follows: in the Second Section, the principle of our methodology for identifying power transformers faults has been described. The process and the results of implementing the two algorithms using our proposed

input vectors are discussed in the third section, where, the best-input vector for each technique has been identified. Finally, the conclusions from this work were summarized and potential future work was mentioned.

II. METHODOLOGY

A. Data collection:

The construction of our proposed input space needs gas concentration values, for this purpose, transformer oil samples are periodically taken for the DGA test using gas chromatography analysis [25-26]. Generally, mixtures of all gases are present in an oil sample, where the relative amount of each, could be an indicator of the existing faults, such as, partial discharges (PD), thermal faults > 700 °C (T3), thermal faults of 300 °C to 700 °C (T2), thermal faults < 300 °C (T1), high energy discharges (D2) and low energy discharges (D1) [7].

In this work, a database of 481 samples has been used in training and testing the proposed methods. This database has been extracted from the literature [27]. The distribution of the training and the testing samples according to their fault type is shown in Table 1.

Table. I
DISTRIBUTION OF TRAINING AND TESTING DATASET SAMPLES

Fault Types	Samples For Training	Samples For Testing
Partial Discharge	32	16
Thermal Faults > 700 °C	57	28
Thermal Faults of 300 °C to 700 °C	32	16
Thermal Faults < 300 °C	63	32
High Energy Discharges	84	42
Low Energy Discharges	53	26
TOTAL	321	160

B. Proposed Input vectors:

The following attributes have been considered in the construction of our proposed input vectors:

1) Using the concentration of the usual five key gases in ppm:

$$X = [C_2H_6, C_2H_4, C_2H_2, CH_4, H_2] \quad (1)$$

2) Using the ratios between key gases (The IEC Ratios):

$$X = [\frac{C_2H_4}{C_2H_6}, \frac{C_2H_2}{C_2H_4}, \frac{CH_4}{H_2}] \quad (2)$$

3) Using the relative percentages of gases:

$$X = [\%C_2H_6, \%C_2H_4, \%C_2H_2, \%CH_4, \%H_2] \quad (3)$$

4) Using ROGER's four-ratio:

$$X = [\frac{C_2H_6}{CH_4}, \frac{C_2H_4}{C_2H_6}, \frac{C_2H_2}{C_2H_4}, \frac{CH_4}{H_2}] \quad (4)$$

5) Using DORNENBURG's four-ratios:

$$X = [\frac{C_2H_2}{CH_4}, \frac{C_2H_4}{C_2H_6}, \frac{C_2H_2}{C_2H_4}, \frac{CH_4}{H_2}] \quad (5)$$

6) Using Duval's triangle coordinates:

$$X = [C_a, C_b] \quad (6)$$

Where

$$C_a = \frac{1}{3}\frac{\sum_{i=0}^{k-1}(a_i+a_{i+1})(a_ib_{i+1}-a_{i+1}b_i)}{\sum_{i=0}^{k-1}(a_ib_{i+1}-a_{i+1}b_i)} \quad (7)$$

And

$$C_b = \frac{1}{3}\frac{\sum_{i=0}^{k-1}(b_i+b_{i+1})(b_ia_{i+1}-b_{i+1}a_i)}{\sum_{i=0}^{k-1}(b_ia_{i+1}-b_{i+1}a_i)} \quad (8)$$

The a_i are calculated by the equations:

$$\begin{aligned} a_0 &= \%CH_4 \cos\left(\frac{\pi}{2}\right) \\ a_1 &= \%C_2H_4 \cos\left(\frac{\pi}{2}+\varphi\right) \\ a_2 &= \%C_2H_2 \cos\left(\frac{\pi}{2}+2\varphi\right) \end{aligned} \quad (9)$$

And the b_i could be obtained by replacing "*cos"* with "*sin*" in the last equations with $\alpha = 2\pi/3$

7) Using Duval's pentagon coordinates:

$$X = [C_a, C_b] \quad (10)$$

Where

$$C_a = \frac{1}{6}\frac{\sum_{i=0}^{k-1}(a_i+a_{i+1})(a_ib_{i+1}-a_{i+1}b_i)}{\sum_{i=0}^{k-1}(a_ib_{i+1}-a_{i+1}b_i)} \quad (11)$$

And

$$C_b = \frac{1}{6}\frac{\sum_{i=0}^{k-1}(b_i+b_{i+1})(b_ia_{i+1}-b_{i+1}a_i)}{\sum_{i=0}^{k-1}(b_ia_{i+1}-b_{i+1}a_i)} \quad (12)$$

The a_i are calculated using the following equations:

$$\begin{aligned} a_0 &= \%H_2 \cos\left(\frac{\pi}{2}\right) \\ a_1 &= \%C_2H_6 \cos\left(\frac{\pi}{2}+\varphi\right) \\ a_2 &= \%CH_4 \cos\left(\frac{\pi}{2}+2\varphi\right) \\ a_3 &= \%C_2H_4 \cos\left(\frac{\pi}{2}+3\varphi\right) \\ a_4 &= C_2H_4 \cos\left(\frac{\pi}{2}+4\varphi\right) \end{aligned} \quad (13)$$

Also, the b_i could be obtained by replacing "*cos"* with "*sin*" in the last equations with $\alpha = 2\pi/5$

8) In this case, a combination of two of the previously mentioned input vectors has been done, Roger's and DORNENBURG's ratios:

$$X = [\frac{C_2H_6}{CH_4}, \frac{C_2H_2}{CH_4}, \frac{C_2H_4}{C_2H_6}, \frac{C_2H_2}{C_2H_4}, \frac{CH_4}{H_2}] \quad (14)$$

9) To further improve fault recognition by expanding the proposed input space , another combination was made in the case of this input vector, Duval's triangle-pentagon coordinate's combination:

$$X = [C_{a1}, C_{b1}, C_{a2}, C_{b2}] \quad (15)$$

Where *{Ca1, Cb1}* are calculated using the triangle method, while *{Ca2, Cb2}* are calculated according to the pentagon one.

C. AI techniques:

1) Naive Bayes

The Naive Bayes algorithm is a simple probabilistic classifier based on Bayes theorem that calculates a set of probabilities by counting the frequency and combinations of values in a given data set. The algorithm assumes that all variables are independent considering the value of the class variable [28], which is rarely existent in real-world applications, so it is characterized as Naive, but the algorithm tends to learn quickly in a variety of controlled classification problems [29]. Bayes theorem is a mathematical formula used to determine the posterior probability $P(x|y)$ from $P(x)$, $P(y)$, and $P(y|x)$:

$$P(x|y) = \frac{P(y|x)\times P(x)}{P(y)} \quad (16)$$

Where $P(x|y)$ refers to the subsequent possibility of the

hypothesis x conditioned by some evidence y and $P(x)$ is the prior probability of x; $P(y|x)$ is the likelihood for y given x, and $P(y)$ is the prior or marginal probability of y. Therefore, Bayes theorem can be clearly interpreted as an alternative form in (17) with respect to each item in (16):

$$Posterior\ Probability = \frac{Likelihood \times Prior\ Probability}{Probability\ of\ Evidence} \quad (17)$$

2) Decision tree

The decision tree algorithm is a non-parametric supervised machine learning's classifier used to split data into a set of branches. The construction of the tree is conducted from top to bottom in a recursive divide-and-conquer manner [30]. Decision tree classifiers are easier to interpret than other classification methods because decision tree is able to break down complex decision-making process into multi union of simpler decisions [31]. Generally, decision tree classifier training is based on finding the best split at each node as long as the complete data set is not analyzed [32]. The said principle leads to the idea of partitioning the feature space until the interrupt criterion is satisfied in each list, or until all points in a given leaf belong to one class. In order to meet the criteria, it is necessary to select the most common class among the data in the list or the one with the highest information gain. Figure 1 illustrates the basic structure of a decision tree.

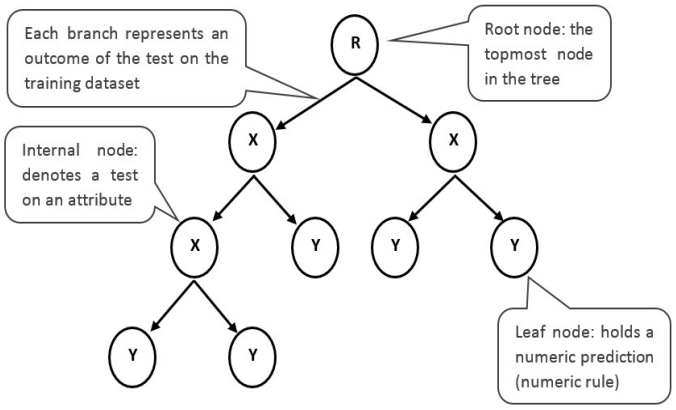

Fig. 1: Decision Tree general structure

Among other classification algorithms, Decision Tree have the following advantages:

- Good performance with large data sets
- Requires little data preparation
- Able to handle both numerical and categorical data
- Easy to display graphically
- Easy to understand and interpret

Construction of decision tree:

In order to select the best variable to split, the Decision Tree uses the information gain. The equation for calculating information gain is as follows:

$$Gain(T, A) = Entropy(T) - \sum_{i=1}^{n} \frac{T_i}{T} Entropy(T_i) \quad (18)$$

Where $Gain(T, A)$ is the information gain of set T (training data) on an attribute A, and T_i is a subgroup of T for which: A has value i.

The Entropy of node T is defined as:

$$Entropy(T) = -\sum_{i=1}^{n} p(i) \log p(i) \quad (19)$$

Where $p(i)$ is the proportion of T belonging to a class i.

III. Results and Discussion

To evaluate the performance of Naïve Bayes and Decision tree algorithms using our proposed input vectors according to six types of transformer faults, namely, they are categorized into partial discharges (PD), low energy discharge (D1), high energy discharge (D2), low thermal fault (T1), medium thermal fault (T2), and high thermal fault (T3), a set of 481 samples has been used to train and test the two methods; 67% of the dataset were used for the training and 33% for the testing, using the MATLAB software. Figure 2 illustrates a brief description of the proposed method.

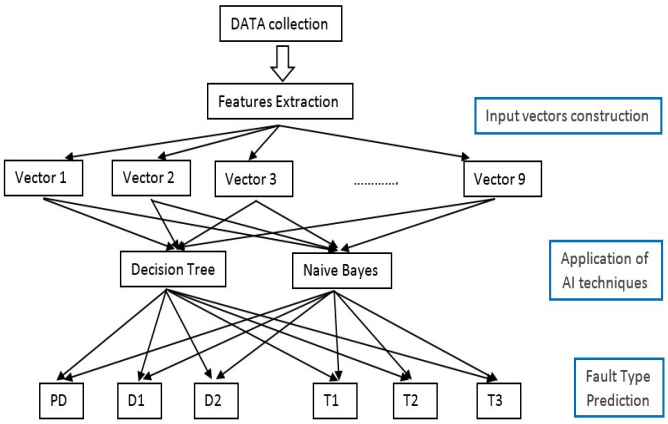

Fig. 2: The general structure of transformer fault recognition using the Naïve Bayes and the Decision Tree Algorithms

Table 2 shows the results of the implementation of the two classifiers using the proposed input vectors.

Table. II
FAULTS DIAGNOSIS ACCURACIES USING THE NAÏVE BAYES AND THE DECISION TREE ALGORITHMS WITH ALL THE PROPOSED INPUT VECTORS

Input vector	Naïve Bayes	Decision tree
Vector 1	25.62	75.62
Vector 2	81.87	80.62
Vector 3	13.75	83.12
Vector 4	11.25	83.75
Vector 5	28.75	77.50
Vector 6	58.25	45.00
Vector 7	42.50	78.75
Vector 8	28.75	76.25
Vector 9	86.25	78.75

From Table 2, it is easy to see that the highest prediction accuracy is obtained using Vector 9 (combined Duval's pentagon and triangle) with the Naïve Bayes algorithm (86.25%). Whereas, in the case of the Decision Tree, the input Vector 4 (Roger's four-ratio method) gives the highest prediction accuracy, up to 83.75%.

In order to deepen the study, the performance of each algorithm with its appropriate input vector was evaluated based on the accuracy of each fault type diagnosis (Figure 3).

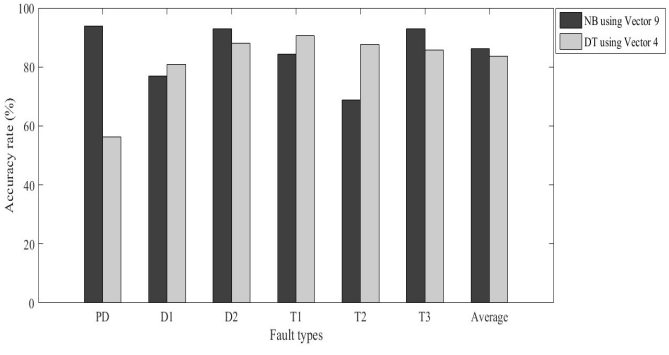

Fig. 3: Histogram of accuracy rate

From Figure 3, it is clear that the performance of each algorithm differs depending on the type of fault. For example, in the case

Table. IV
TANSFORMER FAULTS DIAGNOSIS USING THE TRADITIONAL DGA METHODS AND OUR PROPOSED METHODS

Sample	H2	CH4	C2H6	C2H4	C2H2	Ref.	Duval	Rogers Ratios	IEC Ratios	NB - Vector 9	DT - Vector 4	Act.
01	120	140	30	0	120	[33]	D1	UD*	UD	T2	T1	T1
02	3700	6400	2400	10	7690	[33]	D1	UD	UD	T3	T1	T2
03	125	680	290	20	900	[33]	D1	UD	UD	T3	T1	T3
04	120	10	30	25	5	[33]	T3	UD	PD	D1	PD	D1
05	140	95	10	80	60	[33]	D2	D2	D2	D2	D2	D2
06	240	17	0	5	40	[33]	D1	UD	UD	PD	PD	PD
07	650	53	20	0	34	[33]	D1	PD	UD	PD	PD	PD
08	1076	95	71	231	4	[33]	T3	UD	UD	PD	PD	PD
09	6454	2313	121	6432	2159	[34]	D2	UD	D2	D2	D2	D2
10	305	100	33	541	161	[34]	D2	UD	D2	D2	D2	D1
11	1230	163	27	692	233	[34]	D2	UD	D2	D1	D2	D2
12	33046	619	58	0	2	[34]	PD	PD	UD	PD	PD	PD
13	796	999	234	31	1599	[34]	D1	UD	UD	T3	T1	T3
14	34	21	4	56	49	[34]	D2	D2	D2	D2	D2	D2
15	960	4000	1290	6	1560	[34]	D1	UD	UD	T2	T1	T2
16	6	2990	29990	67	26076	[34]	D1	UD	UD	T1	T1	T1
17	2500	10500	4790	6	13500	[34]	D1	UD	UD	T3	T1	T2
18	300	700	280	36	1700	[34]	D1	UD	UD	T3	T1	T3
19	37800	1740	249	8	8	[34]	PD	PD	PD	PD	PD	PD
20	1450	940	211	61	322	[34]	D1	UD	UD	PD	T1	T1

UD* (Undefined): the method used is unable to determine the type of the fault

of the partial discharges (PD), the Naïve Bayes has the best performance, while, in the case of medium thermal fault (T2), the Decision Tree has the superiority in such fault recognition. Overall, the Naïve Bayes algorithm remains the one with the greatest precision. Table 3 shows the overall result of transformer fault diagnosis using our proposed input vectors with the two used classification algorithms.

Table. III
THE OVERALL RESULTS OF DIAGNOSTIC ACCURACIES USING NAÏVE BAYES AND DECISION TREE CLASSIFIERS

Fault	Vector 1		Vector 2		Vector 3	
Type	NB	DT	NB	DT	NB	DT
PD	25	37.5	87.5	75	93.75	62.5
D1	57.69	73.07	80.76	84.61	3.84	84.61
D2	11.9	69.04	80.95	73.80	2.38	83.33
T1	40.62	100	81.25	84.37	3.12	93.75
T2	0	62.50	68.75	75	25	87.5
T3	14.28	89.28	89.28	89.28	0	78.57

Fault	Vector 4		Vector 5		Vector 6	
Type	NB	DT	NB	DT	NB	DT
PD	0	56.25	81.25	87.5	0	18.75
D1	50	80.76	92.30	80.76	0	50
D2	2.38	88.09	2.38	85.71	97.61	59.52
T1	3.12	90.62	3.12	81.25	84.37	56.25
T2	18.75	87.50	43.75	50	0	31.25
T3	0	85.71	3.57	67.85	89.28	28.57

Fault	Vector 7		Vector 8		Vector 9	
Type	NB	DT	NB	DT	NB	DT
PD	93.75	68.75	81.25	87.50	93.75	87.50
D1	0	69.23	92.30	76.92	76.92	73.07
D2	80.95	85.71	0	85.71	92.85	83.33
T1	59.37	81.25	6.25	87.50	84.37	90.62
T2	0	62.50	37.5	31.25	68.75	68.75
T3	14.28	89.28	89.28	89.28	0	78.57

For the validation stage, the results of Table 3 confirm that the optimal choice of classification algorithm with appropriate input data is critical in the diagnosis of transformer faults.
In order to assess the improvement in fault prediction using our proposed methods, Table 4 presents the diagnosis accuracies of the most common traditional DGA methods (Duval's triangle, Rogers's ratios and IEC ratios) and our proposed methods using a random dataset. The results in Table 4 shows the superiority of the NAÏVE BAYES algorithm with the 9th input vector and the DECISION TREE algorithm with the 4th input vector in transformer fault diagnosis (70% and 60% respectively), while, the other three methods developed poor diagnostic accuracies, Duval triangle (30%), Rogers's ratios (25%), and IEC Ratios (30%).

IV. CONCLUSION

The Naïve Bayes and the Decision Tree classification algorithms were used to identify power transformer faults. A dataset of 481 samples was employed and 9 different input vectors were considered. The Naive Bayes algorithm achieved a diagnostic accuracy of 86.25% when using the 9th input vector (Duval's triangle-pentagon coordinates combination), compared to 83.75% in the case of the Decision Tree using the 4th input vector (ROGER's four-ratio). These diagnostic results show an improvement in the identification of transformer faults over other traditional DGA methods. Significant differences in diagnostic accuracy were obtained when using the same classification algorithm with different input vectors, this investigation shows the appropriate input vector for the diagnosis of power transformers using the Naive Bayes and the Decision Tree algorithms. In a future work, we will extend the proposed input space using other input vectors with an improved machine learning algorithm.

REFERENCES

[1] S. S. M. Ghoneim, I. B. M. Taha, and N. I. Elkalashy, "Integrated ANN-based proactive fault diagnostic scheme for power transformers using dissolved gas analysis", IEEE Transactions on Dielectrics and Electrical Insulation, vol. 23, no. 3, pp. 1838–1845, Jun. 2016.

[2] ''Mineral Oil-Filled Electrical Equipment in Service - Guidance on the Interpretation of Dissolved and Free Gases Analysis'', IEC Standard IEC 60599, IEC, Geneva, Switzerland, Edition 2.1, May 2007.

[3] F. Jakob and J. J. Dukarm "Thermodynamic estimation of transformer fault severity", IEEE Trans. on Power Delivery, vol. 30, no. 4, pp. 1941–1948, 2015. DOI: 10.1109/TPWRD.2015.2415767

[4] I. B. M. Taha, S. S. Dessouky and S. S. M. Ghoneim "Transformer fault types and severity class prediction based on neural pattern-recognition techniques", Electric Power Systems Research, vol. 191, no. 7, 9, pp. 106899, 2021.

[5] A. Hoballah, D. A. Mansour and I. B. M. Taha "Hybrid grey wolf optimizer for transformer fault diagnosis using dissolved gases considering uncertainty in measurements", IEEE Access, vol. 8, pp. 139176–139187, 2020.

[6] M. A. Izzularab, G. E. M. Aly and D. A. Mansour "On-line diagnosis of incipient faults and cellulose degradation based on artificial intelligence methods", IEEE Int. Conf. on Solid Dielectrics, Toulouse, France, 2004.

[7] M. Duval and A. dePabla "Interpretation of gas-in-oil analysis using new IEC publication 60599 and IEC TC 10 databases", IEEE Electrical Insulation Magazine, vol. 17, no. 2, pp. 31–41, Mar. 2001.

[8] "Ieee guide for the interpretation of gases generated in oil-immersed transformers", IEEE Std C57.104-2008 (Revision of IEEE Std C57.104-1991), pp. 1–36, 2009.

[9] M. Duval "A review of faults detectable by gas-in-oil analysis in transformers", IEEE Electrical Insulation Magazine, vol. 18, no. 3, pp. 8–17, May 2002. DOI: 10.1109/MEI.2002.1014963

[10] N. A. Bakar and A. Abu-Siada "Fuzzy logic approach for transformer remnant life prediction and asset management decision", IEEE Transactions on Dielectrics and Electrical Insulation, vol. 23, no. 5, pp. 3199–3208, Oct. 2016.

[11] S. S. M. Ghoneim and I. B. M. Taha ''A new approach of DGA interpretation technique for transformer fault diagnosis'', Int. J. Electr. Power Energy Syst., vol. 81, pp. 265–274, Oct. 2016.

[12] I. B. M. Taha, S. S. M. Ghoneim, and A. S. A. Duaywah ''Refining DGA methods of IEC code and Rogers four ratios for transformer fault diagnosis'', IEEE Power Energy Soc. Gen. Meeting (PESGM), pp. 1–5, Jul. 2016

[13] S.M. Islam, T. Wu, G. Ledwich "A novel fuzzy logic approach to transformer fault diagnosis''. IEEE Trans. Dielectr. Electr. Insul, 7, 177–186, 2000

[14] S. Souahlia, K. Bacha and A. Chaari "MLP neural network-based decision for power transformers fault diagnosis using an improved combination of Rogers and Doernenburg ratios DGA", Int. Journal of Electrical Power & Energy Systems, vol. 43, no. 1, pp. 1346–1353, 2012

[15] V. Miranda, A.R.G. Castro ''Improving the IEC table for transformer failure diagnosis with knowledge extraction from neural networks''. IEEE Trans. Power Deliv., 20, 2509–2516, 2005

[16] Y. Benmahamed, M. Teguar, A. Boubakeur ''Application of SVM and KNN to Duval Pentagon 1 Transformer Oil Diagnosis''. IEEE Trans. Dielect. Electr. Inst., 24, 3443–3451, 2017

[17] K. Bacha, S. Souahlia and M. Gossa "Power transformer fault diagnosis based on dissolved gas analysis by support vector machine", Electrical Power Systems Research, vol. 83, no. 1, pp. 73–79, 2012.

[18] H. Zheng, Y. Zhang, J. Liu, H. Wei, J. Zhao, R. Liao ''A novel model based on wavelet LS-SVM integrated improved PSO algorithm for forecasting of dissolved gas contents in power transformers''. Electr. Power Syst. Res., 155, 196–205, 2018

[19] Y. Zhang, H. Wei, R. Liao, Y. Wang, L. Yang, C. Yan ''A New Support Vector Machine Model Based on Improved Imperialist Competitive Algorithm for Fault Diagnosis of Oil-immersed Transformers''. J. Electr. Eng. Technol. 2017, 12, 830–839.

[20] O. Kherif, Y. Benmahamed, M. Teguar, A. Boubakeur and S. S. M. Ghoneim "Accuracy Improvement of Power Transformer Faults Diagnostic Using KNN Classifier With Decision Tree Principle" in IEEE Access, vol. 9, pp. 81693-81701, 2021.

[21] J. I. Aizpurua, V. M. Catterson, B. G. Stewart, S. D. J. McArthur, B. Lambert, B. Ampofo, G. Pereira, and J. G. Cross ''Power transformer dissolved gas analysis through Bayesian networks and hypothesis testing'', IEEE Trans. Dielectrics Electr. Insul., vol. 25, no. 2, pp. 494–506, Apr. 2018. DOI: 10.1109/TDEI.2018.006766

[22] M. T. Yang, L. S. Hu ''Intelligent fault types diagnostic system for dissolved gas analysis of oil-immersed power transformer". IEEE Trans. Dielectr. Electr. Insul., 20, 2317–2324, 2013

[23] J. Dai, H. Song, G. Sheng, X. Jiang ''Dissolved gas analysis of insulating oil for power transformer fault diagnosis with deep belief network". IEEE Trans. Dielectr. Electr. Insul., 24, 2828–2835, 2017

[24] P. Mirowski, Y. LeCun ''Statistical Machine Learning and Dissolved Gas Analysis: A Review''. IEEE Trans. Power Deliv., 27, 1791–1799, 2012. DOI: 10.1109/TPWRD.2012.2197868

[25] P. Mirowski and Y. LeCun "Statistical Machine Learning and Dissolved Gas Analysis: A Review", IEEE Trans. Power Del., vol. 27, no. 4, pp.1791–1799, Oct. 2012.

[26] N. Abu Bakar, A. Abu-Siada, and S. Islam "A Review of Dissolved Gas Analysis Measurement and Interpretation Techniques", IEEE Electr. Insul. Mag., vol. 30, no. 3, pp. 39–49, May-June 2014.

[27] I.B.M. Taha, A. Hoballah, S.S.M. Ghoneim ''Optimal ratio limits of Roger's four-ratios and IEC 60599 code methods using particle swarm optimization fuzzy-logic approach''. IEEE Trans. Dielect. Electr. Inst., 27, 222–230, 2020. DOI: 10.1109/TDEI.2019.008395

[28] M. S. Mücahid, Y. Ali ''Performance Analysis of ANN and Naive Bayes Classification Algorithm for Data Classification''. Intern. J. of Intelligent Systems and Applications in Engineering, IJISAE, 7(2), 88–91, 2019

[29] G. Dimitoglou, J. A. Adams and C. M. Jim ''Comparison of the C4. 5 and a Naïve Bayes classifier for the prediction of lung cancer survivability''. arXiv preprint arXiv:1206.1121, 2012

[30] J. R. Quinlan ''Induction of decision trees''. Mach Learn 1(1):119–127, 1986.

[31] A. Alqudsi and A. El-Hag "Application of machine learning in transformer health index prediction", Energies, vol. 12, no. 14, pp. 2694, 2019. DOI: 10.3390/en12142694

[32] J. R. Quinlan "C4.5: Programs for Machine Learning", Morgan Kaufmann Publishers, 1993

[33] J. Soni and D. Suthar "An Experimental Analysis to Check Accuracy of DGA Using Duval Pentagonal Method in Power Transformer", ICRISET2017 the Int. Conf. on Research and Innovations in Science, Engineering and Technology, vol 1, pp. 394--401, Aug. 2017.

[34] J. Dukarm and F. Jakob "Thermodynamic estimation of transformer fault severity" IEEE/PES Transmission and Distribution Conference and Exposition (T&D), Dallas, TX, USA, pp. 1-1, 2016

Yassine Mahamdi received the Master's and Engineer's degrees in Electrical Engineering from Ecole Nationale Polytechnique (ENP) of Algiers in 2018. He is currently a Ph.D. student at the Electrical Engineering Department in the same School. His field of research is based on transformer diagnostics and artificial intelligence.

Ahmed Boubakeur received in 1975 the degree of Engineer in electrical engineering from Ecole Nationale Polytechnique (ENP) of Algiers, and in 1979 he obtained the Doctorate in Technical Sciences from the Institute of High Voltage Engineering of the Technical University of Warsaw of in Poland. He is currently a professor at ENP of Algiers where he has been giving lectures and supervising research in the field of High Voltage Engineering since 1982. His principal research areas are discharge phenomena, insulators pollution, lightning, polymeric cables insulation, transformer oil ageing, neural network and fuzzy logic application in HV insulation diagnosis, and electric field calculation and measurement. He is an IEEE senior member, member of IEEE/DEIS and a member of the Algerian HV Power Systems Association ARELEC (National Algerian Comity of CIGRE and ENP Elders Association ADEP). He has been member of the Editorial Board and Associate Editor of IET/SMT.

Abdelouahab Mekhaldi received the degree of Engineer in 1984 in electrical engineering, the MSc degree in 1990 and a Ph.D. in high voltage engineering in 1999 from Ecole Nationale Polytechnique (ENP) of Algiers. He is currently a Professor at ENP. His main research areas are in discharge phenomena, outdoor insulators pollution, polymeric cables insulation, lightning, artificial intelligence application in high voltage insulation diagnosis and electric field calculation.

Youcef Benmahamed received the degree of Engineer and Master's degree in power electronics engineering in 2014 and Ph.D in High Voltage techniques in 2019 from Ecole Nationale Polytechnique (ENP) of Algiers. His research interests are in diagnosis, artificial intelligence and optimization techniques.

Comparison of two purification methods of Algerian bentonite: chemical, mineralogical and physicochemical properties

Nabil Babahoum, Malek Ould Hamou, Amira Merchichi, and Farid Aghilas Mansour

Abstract− The aim of this work is to evaluate the efficiency of two methods of purification on Algerian bentonite clay. The first method was performed by centrifugation treatment, using sodium hexametaphosphate $(NaPO_3)_6$ as a dispersing agent. The second method involves a chemical purification with NaCl, followed by sedimentation technique. The study concerns mineralogical, chemical, structural aspects and a series of physical testing. The results have shown that the raw bentonite (RBN) contain (~ 59%) of montmorillonite, illite (~ 5) and (~26%) of quartz, and feldspar (orthoclase + albite), with 5% of calcite. In the purified state by NaCl (RBN-2), the mineralogical and physicochemical properties including cation exchange capacity and specific surface area are higher than the purified samples by physical beneficiation (by centrifugation - RBN-1). Moreover, the treatment with NaCl increased the montmorillonite content of the bentonite from 56 % to 100%. The quartz impurities were totally removed in RBN-2, whereas impurities (quartz + feldspar) were still observed by the X-ray diffraction (XRD). Finally, the results obtained from the morphological, mineralogical and chemical characterization confirm that the bentonite RBN -2 was more effective , and it has promise as an engineering material compared to the RBN and RBN-1, indicating its possible application in various industrial applications.

***Keywords*− Bentonite, Centrifugation, Mineralogical, Beneficiation, Material.**

NOMENCLATURE

RBN	Raw Bentonite Clay.
RBN-1	Purified Bentonite By Centrifugation.
RBN-2	Purified Bentonite By NaCl.

I. INTRODUCTION

As a geological term, bentonite is a rock formed from altered volcanic ashes and largely composed of montmorillonite type smectites [1]. Depending on their genesis, bentonite clay, in addition to smectite, contain a variety of accessory minerals. These minerals may include mainly quartz, feldspar, calcite, illite and mica [2]. Due to their unique physical and chemical properties, bentonites are used in great varieties of industries. The major uses of bentonites in industry are as foundry , sand bonds, drilling mud, pet litter and iron ore pelletizing , cosmetics, foods, pharmaceuticals, thickeners and extenders for paints, additives in ceramics, coating and filling of paper, organ clays and acid activated bleaching earths [3,4] . The commercial importance of bentonites depends on the quality and quantity of smectites and other minerals [5] as well as other technological proprieties like ; the cation exchange capacity and specific surface area . Enrichment of bentonite clays is very important step in the production of bentonite – based products for any industry [5] . Many different methods of enrichment are proposed in the literature to purify bentonite materials . The magnetic separation , centrifugation and sizing methods can be applied to extract the montmorillonite (fraction < 2 µm) and remove quartz and kaolinite impurities . On the other hand, the chemical purification was proposed in order to eliminate the iron oxides and the carbonates onto the clays [6,7-8].

In this study, a bentonite clay, taken from the Hammam Boughrara one of the largest bentonite deposits in Algeria and Africa , was subjected in order to describe and compare the properties of the bentonitic clay after purification with tow deferent process : (1) by centrifugation technic and (2) by NaCl treatment . The purification process are carried out at the research laboratory of mining engineering department (National Polytechnic School , Algiers) .

II. MATERIALS AND METHODS

The raw bentonite was collected from a mine located in Hammam Boughrara, Maghnia district in Tlemcen province (Algeria). The samples were mixed and quartered to obtain a representative sample of the completely bentonitic deposit. Then the samples were sieved, dried at 60 °C in a laboratory for a period of 24 h

A. Method -1: Physical purification by centrifugation

This processing was described by Thuc et.al [8] , Five grams of natural bentonite sample were agitated for 60 min in 1 L of deionized water with about 0.25 g of sodium hexametaphosphate $(NaPO_3)_6$ as a dispersing agent. After centrifugation for 5 min at 2500 r/min, the fine fraction in

Manuscript received October 29, 2021; revised April 25, 2022.

N. Babahoum is with SONATRACH, Algeria (e-mail: nabil.babahoum@g.enp.edu.dz)
M. Ould Hamou, A. Merchichi and F. A. Mansour are with the Mining Department, Ecole Nationale Polytechnique, Algiers, ALGERIA. (e-mail: malek.ould_hamou@g.enp.edu.dz, amira.merchichi@g.enp.edu.dz,farid_aghilasse.mansour@g.enp.edu.dz)

Digital Object Identifier (DOI): 10.53907/enpesj.v2i1.64

dispersion was collected and dried at 70ºC. Then, the dried bentonite was re-ground to obtain fine powder for experimental purpose. Fig.1 shows a simplified flow sheet for the beneficiation by centrifugation. The centrifugation time was estimated from the following relation based on Stokes' law:

$$t = [\eta \log10 (R/ S)] / [3.81 N2 r2 \Delta S]$$

with:

t centrifugation time (second)
R distance from the deposit surface to the axe of rotor (12 cm)
S distance from the suspension surface to the axe of rotor (4 cm)
N rotation speed = (2500 r/min)
r maximum radius in cm of the desired particles (cm) = ($2 \cdot 10^{-5}$ cm)
ΔS specific gravity difference between the particles and the liquid suspension (0.00528 g cm^{-3})
η viscosity of the fluid (0.00748 poise at 25 °C)

B. Method -2: Chemical purification of bentonite by Na$^+$ ion exchange

The raw bentonite was chemically purified according to classical purification method of Bergaya et al. 2013 [9,10] . About 25 g of raw bentonite was first dispersed in 400 mL of 1 M NaCl solution, stirred magnetically overnight and centrifuged at 3000 r/min for 2 h . Then , the supernatant liquid was added to the same volume of 1 M NaCl. This same process (agitation + centrifugation) was repeated several times to give sodium saturated bentonite (Na^+ bentonite). Finally chloride free slurry was obtained by washing with deionized water (as confirmed with the silver nitrate test). The particles smaller than 2 µm (montmorillonite particles) were collected by sedimentation [11] (Fig.2)

C. Mineralogical analysis

Bentonite samples (natural and after treatment; RBN and RBN-1. RBN-2) were mineralogicaly characterized at the research center CRPEC (Centre de Recherche Scientifique et Technique en Analyses Physico – Chimiques - Bou Ismaïl) , with an X'Pert Pro PANalytical diffractometer (CuKα radiation), 40 kV accelerating voltage, and 20 mA intensity. The scan was recorded in the angular range of 2°–30° (2θ) with a step size 0.017° (2θ) and a scanning speed of 2° per minute [10].

D. Chemical analysis

Chemical compositions (major element contents) of all samples were obtained with a Philips X-ray fluorescence spectrometer, model PW2400 [10].

E. SEM observations

Morphological characteristics of bentonite samples were checked with scanning electron microscopy (SEM), using QUANTA 250 SEM equipment. The SEM images were acquired with an applied acceleration voltage of 300 kV [10]. The scanning electron microscopy (SEM) and chemical analysis are carried out at the research center CRPEC (Centre de Recherche Scientifique et Technique en Analyses Physico – Chimiques - Bou Ismaïl) .

D. Cation exchange capacity (CEC) and specific surface area (SSA)

SSA and CEC measurements were determined using the methylene blue method (spot test) [10, 12-13].

The CEC was computed by Eq. (1) [14]:

$$CEC = (100 \cdot Vcc \cdot Nmb) / ms \qquad (1)$$

Where, ms is the mass of the specimen (g), Vcc is the volume of the methylene blue titrant (mL) and Nmb is the normality of the methylene blue substance (meq / mL).

Specific surface area (SSA) values were calculated from the following Eq. (2) [13]:

$$SSA = \frac{1}{319.8} \frac{1}{200} (0.5N) A_V A_{MB} \frac{1}{10} \qquad (2)$$

where N is the number of MB increments added to the soil suspension solution, Av is Avogadro's number, and A_{MB} is the area covered by one MB molecule.

E. Particle size analysis

In this part, The raw and purified samples were studied by means of a laser granulometer Mastersizer (2000 Ver 4.00) to determine the range of particle sizes in our bentonite samples and to identify the efficiency of tow purification methods in separating the small particles from all materials.

III. RESULTS AND DISCUSSIONS

A. Mineralogical analysis of natural and purified bentonites (RBN, RBN-1 and RBN-2)

The mineralogical study aimed to determine the mineralogical composition of the clays studied before and after purification, and also to follow the influence of each purification method on the quality of bentonite clays . Comparative X-ray diffraction (XRD) diagrams for the RBN, RBN-1 and RBN-2 samples are presented in Figs. 3, 4 and 5 respectively.

The mineralogical analysis clearly reveal important significant differences. XRD results shown in Table1 indicate that the raw bentonite (RBN) within the Hammam Boughrara area is mainly composed of montmorillonite (~ 59%) and illite (~ 5%). The major non clay minerals are quartz (11%), feldspar (15%), calcite (5%) and (orthoclase + albite) (Fig. 3).

Compared with the raw material, the examination of the diffractograms recorded on the clay sample after the treatment by method 0-1(RBN-1) , the results demonstrated that an decrease in certain characteristic lines of the crystalline phases in the form of impurities, particularly those of quartz with a total disappearance of the intensity corresponding of feldspar (orthoclase + albite) and illite (Fig. 4).

On the other hand, XRD analysis of the purified sample RBN-2 showed that it was composed mostly of montmorillonite (≥ 99%). Quartz, feldspar and other impurities were totally absent (Fig. 5). The obtained mineralogical results confirms that the purification procedure as carried out, by method -2 is more efficient.

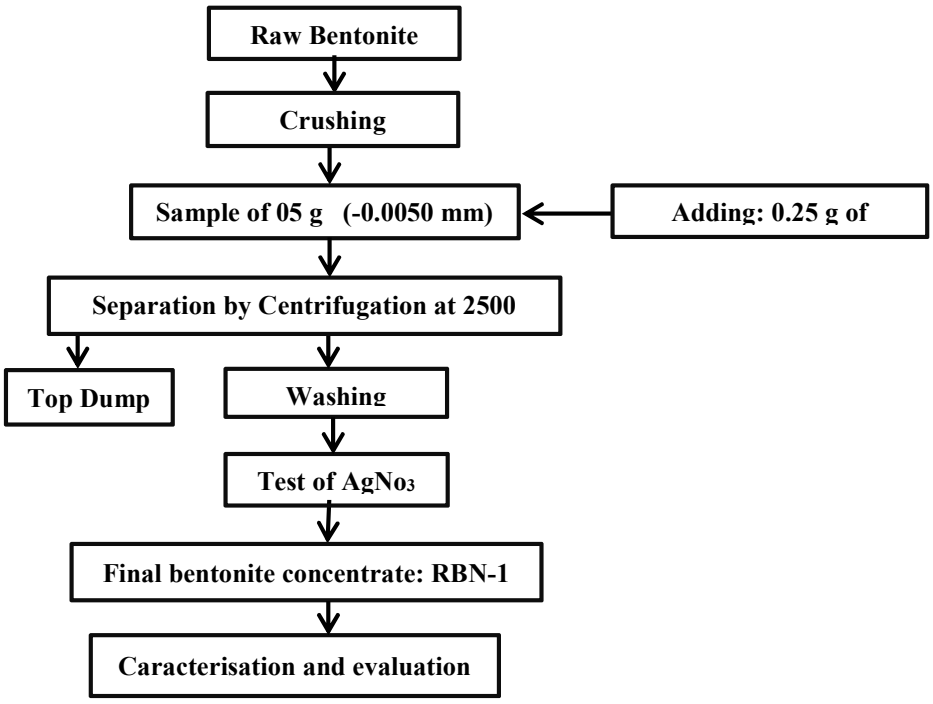

Fig. 1: Flow sheet of beneficiation by centrifugal scheme (method 1)

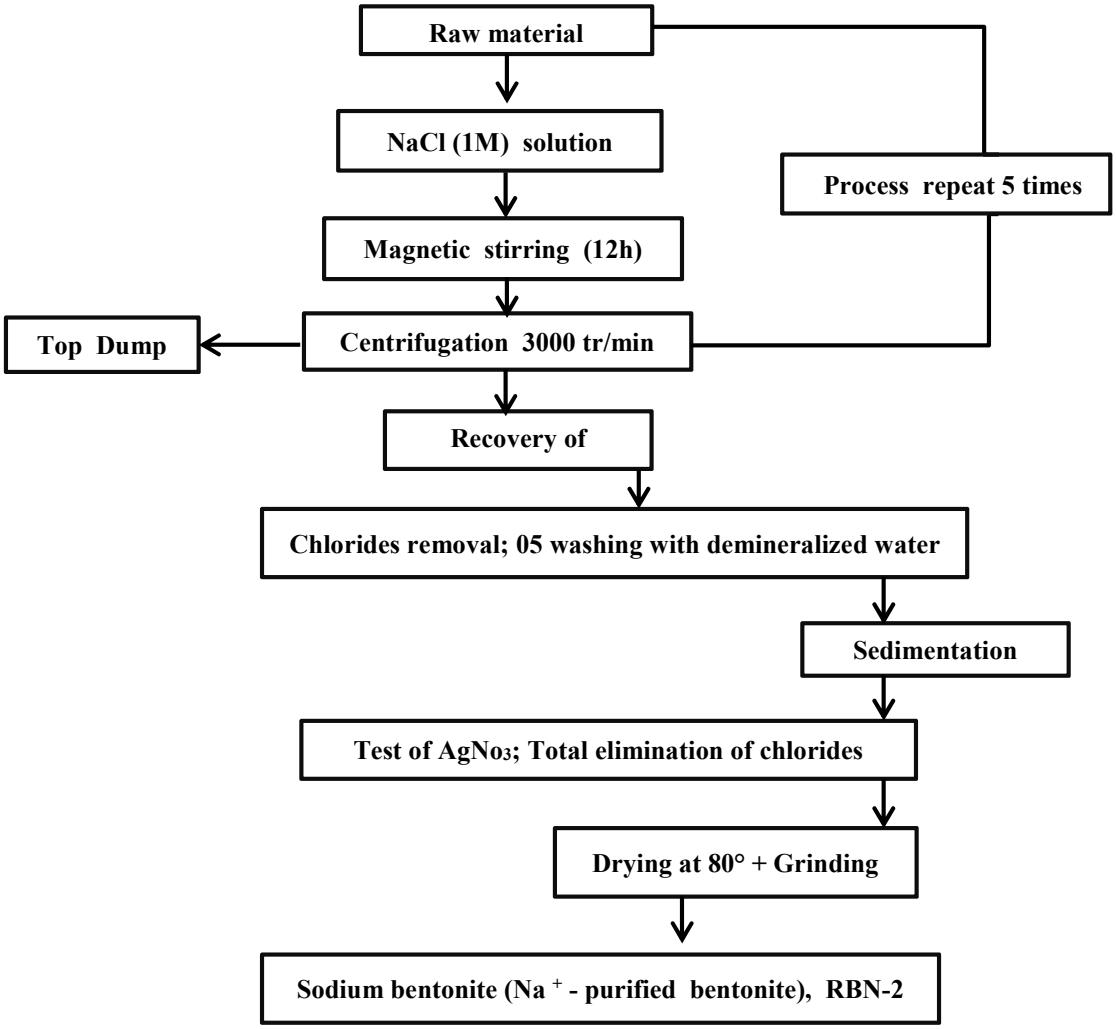

Fig. 2: Flowsheet of chemical purification by Nacl (method -2)

Table 1
MINERAL CONTENT OF RAW AND PURIfiED SAMPLES (RBN , RBN-1 AND RBN-2) DETERMINED BY XRD

Sample	Montmorillonite (%)	Illite (%)	Feldpar (%)	Calcite (%)	Quartz (%)
RBN	59	5	20	5	11
RBN-1	85	0	0	5	10
RBN-2	100	0	0	0	0

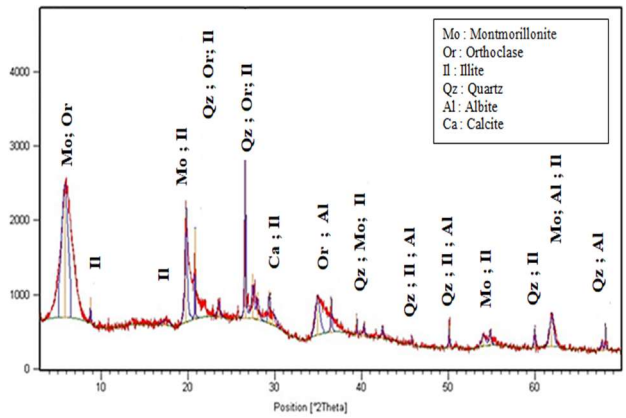

Fig. 3: X-ray diffraction patterns of RBN

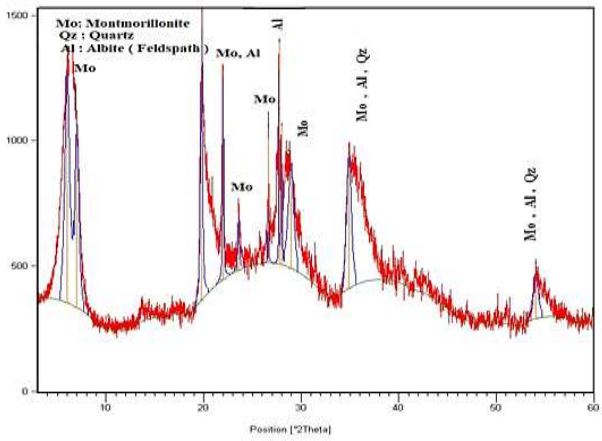

Fig. 4: X-ray diffraction patterns of RBN -1

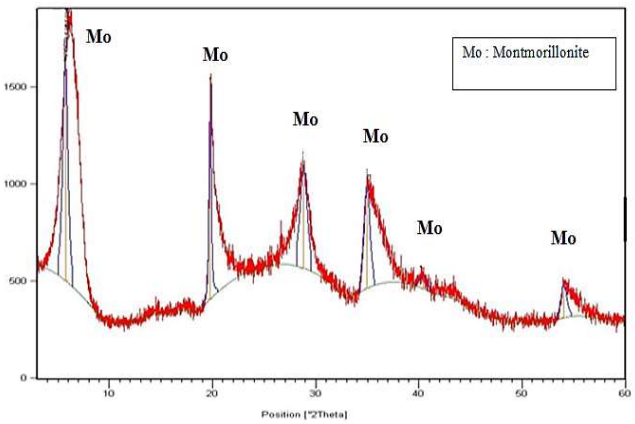

Fig. 5: X-ray diffraction patterns of RBN -2

B. Chemical analysis

The results of chemical compositions of bentonite samples (RBN, RBN-1 and RBN-2) are reported in Table 2. The major element oxides found in all samples were SiO_2, Al_2O_3 and Fe_2O_3, and small quantities of other compounds such as CaO, MgO, Na_2O, TiO_2 and SO_3. Increased silica (SiO_2 %) and alumina (Al_2O_3 %) contents in RBN-1 and RBN-2 were probably associated with the low percentages of quartz and feldspar minerals which is in agreement with the XRD data [15].

The contents of CaO and MgO were low for RBN-1 and RBN-2, which is related to the absence of carbonates. The purification process by two methods increased the content of TiO_2 and SO_3.

High amounts of Na_2O were observed in the RBN-2 sample, and this difference was due to the transformation of Ca^{2+} bentonite into Na^+ bentonite [16].

C. SEM observations

The studies by SEM were conducted to study the change in morphological characteristics of natural and purified samples. The images obtained by scanning electron microscopy of all samples bentonite, with different magnifications, are shown in the figures 6 A, B, D, E, F . The original bentonite (RBN) was composed of large pseudo spherical aggregates of smectite, generally sized from 5 to 100 µm (Fig. 6A, B) and Most of the particles were unconnected from each other.

In the case of purified bentonite method 1(RBN-1) , an excess of bentonite clay is observed in irregular angular shape and the presence of a greater proportion of spherical particles, and association of small circular particles generally sized from 10 m to 100 m (Fig. 6C,D). It also reveals that the surface morphology was almost compact as the same of natural sample.

After purification with NaCl (RBN-2), the surface morphology was changed significantly. When looking at higher magnification, we can observe a significant presence of macros pores arranged in the form of sheets for the sodium bentonite (Fig. 6E, F) and which we did not observe on the raw material. This is probably due to the various processing steps that the clay raw material has undergone (sodification by NaCl + sedimentation and total elimination of impurities) at the side surfaces of the particles.

Table 2

CHEMICAL COMPOSITIONS OF THE RAW AND PURIFIED BENTONITE EXPRESSED AS WEIGHT PERCENT OF MAJOR ELEMENT OXIDES BASED ON X-RAY fIUORESCENCE ANALYSES

Sample	SiO_2 (٪)	Al_2O_3 (٪)	Fe_2O_3 (٪)	MgO (٪)	CaO (٪)	Na_2O(٪)	K_2O(٪)	TiO_2(٪)	SO_3(٪)	LOI(٪)
RBN	51.47	18.50	2.66	6.16	2.86	1.72	1.14	0.25	0.34	17.19
RBN-1	53.80	19.10	1.8	5	1.5	1.65	1	0.35	0.2	15.60
RBN-2	56.40	19 .22	2	3.11	1.56	3.12	1	0.45	0.56	12 ,58

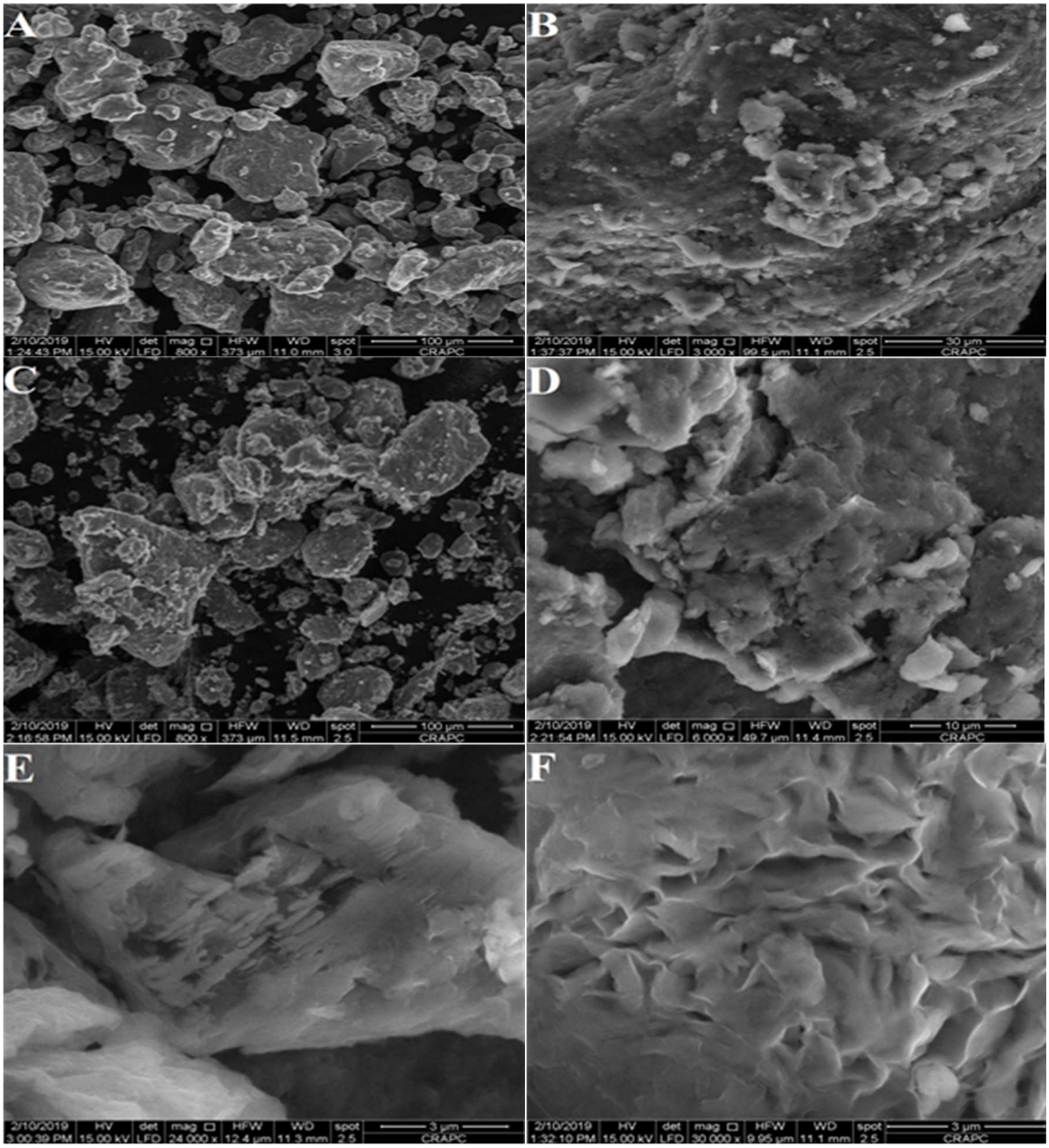

Fig. 6: SEM images of RBN (A, B), RBN-1(C, D) and RBN-2 (E, F)

D. Cation exchange capacity (CEC) and specific surface area (SSA)

CEC and SSA values of natural and purified bentonite samples (RBN , RBN-1. RBN-2) are illustrated in Table 3. Significant increases in CEC and SSA were observed (Fig.7 A and B, respectively). The cation exchange capacity CEC ranged from 61.76 to 70.36 and to 88.20 meq/100 g for RBN-1 and RBN-2 , respectively . These results could be related to the mineralogical changes that occurred in the clay minerals. Also, this increase in CEC is caused by the complete conversion of natural bentonite to Na + bentonite and therefore replacement of the pre-existing interlayer cations with sodium cations occurs and gives the maximum CEC value of 88,20 meq. / 100g.

Purified bentonite RBN-2 has a specific surface area of 677.7 m2/g), greater than the raw bentonite RBN (474.64 m2 / g) and RBN-1 (540.70 m2 / g).

This significant increase in SES is due to the total removal of impurities and the high purity and high montmorillonite content obtained by purification (method -2).

Table 3

CATION EXCHANGE CAPACITY (CEC) AND SPECIFIC SURFACE AREA (SSA) VALUES OF RAW AND PURIFIED SAMPLES

Sample	RBN	RBN-1	RBN-2
CEC (meq/100g)	61.76	70.36	88.20
SSA (m^2/g)	474.64	540.70	677.71

E. Particle size analysis

RBN-1 sample showed a broad particle size distribution with high volume percentages centered at 5 µm and 11 µm, which were attributed to quartz, feldspar and other impurities [10]. (Fig. 8).

In the case of RBN-1, we did not see a big change in the particle size distribution compared to RBN; this may be explained by the mineralogical composition of RBN-1, which may be the same with the RBN.

After beneficiation by NaCl, the volume percentage of the fine particle size increased dramatically compared to RBN and RBN-1 samples, and two maxima (one centered at 0.3 µm and the other centered at 1.5 µm) were attributed to the purity of RBN-2 clay (100% of montmorillonite) [10].

IV. CONCLUSION

In this study, Algerian bentonite samples underwent physical and chemical purifications in order to evaluate the efficiency of tow methods and their characteristics were analyzed using different methods. Raw bentonite clay is composed of montmorillonite (59%) associated with variable proportions of quartz, feldspar and calcite. The chemical compositions indicated that SiO_2 (51.47%), Al_2O_3 (18.50%) and MgO (6.16%) are major elements while Ti_2O_3 is less abundant (0.25%).The efficiency of chemical treatment (by NaCl) is clearly approved, because it allows a better increase in the content of montmorillonite. Moreover, this method leads to a total disappearance of impurities and especially of quartz and feldspar. Physicochemical characterizations showed that purified bentonite by method-2 (chemical purification by NaCl) has a higher values of cation exchange capacity (CEC) and specific surface area (SES).

On the basis of bulk mineralogical composition, chemical and physical properties of Algerian bentonite indicate that the purification by chemical procedure is more efficient and the treated bentonite (by NaCl) could be potential materials for industrial applications.

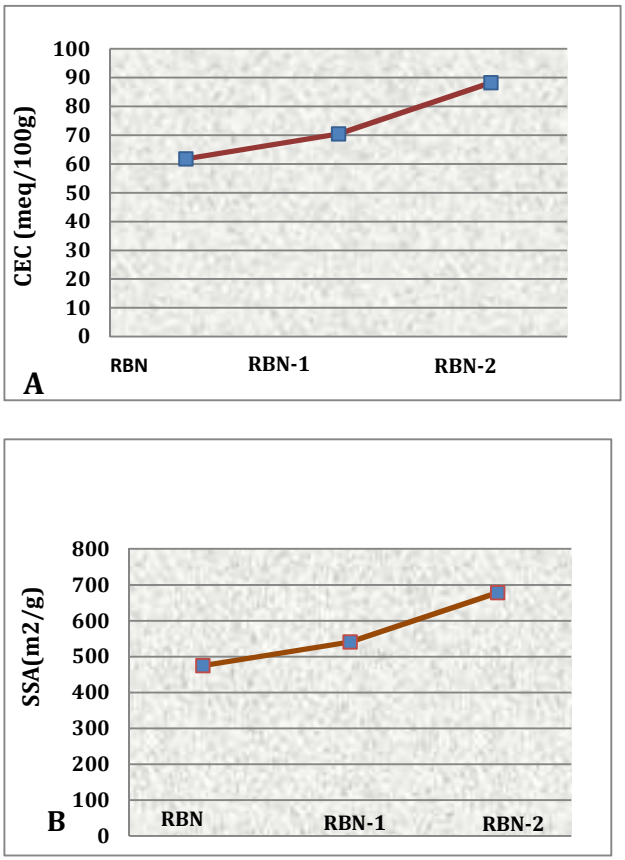

Fig. 7: A, variation of CEC values in RBN, RBN-1 and RBN-2; **B**, variation of SES values in RBN, RBN-1 and RBN-2

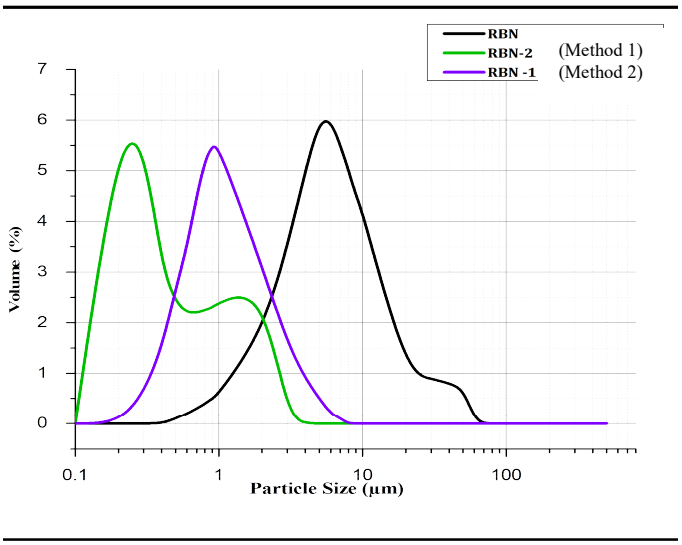

Fig. 8: Distributions of particle sizes for RBN, RBN-1 and RBN-2 bentonite clay

REFERENCES

[1] MBulut.G, Chimeddorj.M, Esenli F, Çelik.MS,“ Production of desiccants from Turkish bentonite. Appl” 2009 , Clay Sci 40:141–147.

[2] F. Boylu, K. Çinku, F. Esenli, and M. S. Çelik, “The separation efficiency of Na-bentonite by hydrocyclone and characterization of hydrocyclone products,” 2010 , Int. J. Miner. Process, 94, 196-202.

[3] Allo, W.A, Murray, H.H., “Mineralogy, chemistry and potential applications of a white bentonite in San Juan province, Argentina”. 2004. Appl. Clay Sci. 25, 237–243.

[4] Christidis.G and Scott, P.W. “Origin and colour properties of the white bentonites. A case study from the Aegean Islands of Milos and Kimolos, Greece. Mineralium Deposita,” 1997, 32, 271–279.

[5] S, Yildiz A “Application of box— behnken design to modeling the effect of smectite content on swelling to hydrocyclone processing of bentonites with various geologic properties”. (2010), Clays Clay Miner 58:431–448. DOI: 10.1346/CCMN.2010.0580312

[6] Chipera, S.J, Guthrie Jr, G.D, Bish, D.L, In: Guthrie Jr., G.D., Mossman, B.T. (Eds.), 1993 “Health Effects of Mineral Dusts”, Chapter 6, 28, pp. 235–249.

[7] Ottner, F, Gier, S, Kuderna, M, Schwaighofer, B. “Results of an inter-laboratory comparison of methods for quantitative clay analysis”. Appl. Clay Sci. 17, 223–243.

[8] Thuc C.-N. H, Grillet A.-C. ,Reinert L., Ohashi F., Thuc H. , Duclaux L., “Separation and purification of montmorillonite and polyethylene oxide modified montmorillonite from Vietnamese bentonites”, 2010, Applied Clay Science 49 (2010) 294–300.

[9] Bergaya F, Lagaly G. “Purification of natural clays. In: Bergaya, F., Lagaly, G. (eds.) ‘’Handbook of Clay Science”, 2nd edn. Elsevier, Amsterdam; 2013.

[10] Babahoum, N., Ould Hamou, M. “ Characterization and purification of Algerian natural bentonite for pharmaceutical and cosmetic applications”.BMC Chemistry 15, 50 (2021).

[11] Van Olphen H. “Clay colloid chemistry. New York: Interscience Publishing”; 1963. p. 16–29.

[12] Yukselen Y, Kaya A. “Suitability of the methylene blue test for surface area, cation exchange capacity and swell potential determination of clayey soils”. Eng Geol. 2008;102:38–45.

[13] Santamarina JC, Klein KA, Wang YH, Prencke E. “Specific surface: determination and relevance”. Can Geotech J. 2002;39:233–41.

[14] Cokca E, Birand A. “Determination of cation exchange capacity of clayey soils by the methylene blue test”. Geotech Test J. 1993;16 (4):518–24. DOI:10.1520/GTJ10291J

[15] Gamoudi S, Srasra E. “Characterization of Tunisian clay suitable for pharmaceutical and cosmetic applications”. Appl Clay Sci. 2017;146:162–6. DOI: 10.1016/j.clay.2017.05.036

[16] El shater A, El-haddad A, El-attaar A, Abugharbi M, Soliman W. “Characterisation of the Egyptian Pliocene bentonite from the Sohag region for pharmaceutical use”. Arab J Geosci. 2018;11:385–97.

Nabil Babahoum received the degree of Engineer and Master’s degree in 2014 and Ph.D in 2022 in mining engineering from Ecole Nationale Polytechnique (ENP) of Algiers. He is a WellSite Geologist at SONATRACH since 2015.

Malek Ould Hamou is a professor at Ecole Nationale Polytechnique, Algiers, Algeria. He was the head of mining engineering department and the director of the mining engineering laboratory of the same establishment. His research interests are mineralurgy, bio-processing and mining environment.

Amira Merchichi is an assistant professor at Ecole Nationale Polytechnique, Algiers, Algeria, since 2014. Her research interests are mining environment, mineral processing, biomining.

Farid Aghilas Mansour is a PhD student at the Department of Mining Engineering, Ecole Nationale Polytechnique, Algiers, Algeria. His research interests are in Geochemistry, Geostatistics and Mineralogy.

Task management in IoT-Fog-Cloud environment employing static scheduling Techniques

Gaurav Goel and Rajeev Tiwari

Abstract— In a distributed computing system, there are limited resources, which needs to be utilized effectively. Then for improving QoS Fog computing paradigm is an effective way, with suitable allocations. Thus, different resource scheduling and optimization algorithms exist. However, still, there is a scope to improve bandwidth, latency, energy consumption, and total communication cost in the Fog environment. In this work investigation is done to show significance of task management in such resource constrained environment. Various heuristics and meta-heuristic algorithms are evaluated using simulations, to show the task placement and their impacts by using 5 different Montage datasets from work flow sim tool kit for Fog-Computing environment. Then QoS parameters like cost, makespan, and energy consumptions are computed for various state-of-the-art techniques like Min-max, PSO, GA, ACO, and BLA. This shows the behaviour of these techniques with such different tasks and allocation environment configurations. Evaluated result parameters are collected and presented in the result section. This work shows the effectiveness of heuristics and meta-heuristics techniques to manage the tasks and their allocations in the Fog environment.

***Keywords*— Task management, IoT, Fog, Cloud, Resource Scheduling.**

I. INTRODUCTION

IoT devices are expanding rapidly with an increase in networking technologies. Large applications are being developed by a group of users. These applications require more computation, large resources, and an intelligence system. Resources available to execute this application are insufficient with cloud devices. The problem of latency, high cost, and high makespan is faced by users while transferring their application data to the cloud for computation [1].

To overcome these problems a Fog environment is introduced by CISCO. The Fog paradigm is providing the same environment as a cloud in contrast to computation by using Fog nodes. Fog nodes can be a router, switches, gateway, modems, etc. Fog nodes are heterogeneous and distributed with limited storage and computation capacity. However, some applications require high storage and computation capacities, for this cloud can be used at the backend. Today's Fog paradigm is used in many applications like health monitoring, traffic management, industries, and farming. The benefit of using a Fog environment in this application is that Fog nodes are established in proximity to the end devices. Because of this benefit problems of latency, and bandwidth can be reduced [2,3]. Many researchers have discussed the problem of optimization in this scenario. Many optimization algorithms have been designed to achieve Quality of Service (QoS) in the IoT-Fog-Cloud environment. Many researchers have focussed on the technique of task management but still, there is a problem with latency, bandwidth, and the cost is raised.

Manuscript received November 20, 2021; revised June 9, 2022.

Gaurav Goel , Department of Computer Science and Engineering, Chandigarh Group of Colleges, Landran (Mohali), India, and Research Scholar, University of Petroleum and Energy studies, Dehradun, India, (email: gaurav.coecse@cgc.edu.in)
Rajeev Tiwari, School of Computer Science, University of Petroleum and Energy studies, Dehradun, India, (email: errajeev.tiwari@gmail.com)

Digital Object Identifier (DOI): 10.53907/enpesj.v2i1.76

A. RESOURCE MANAGEMENT IN FOG COMPUTING

Resource distribution and planning is an important technology for managing resource utilization, and obtaining load balancing for the data centers. In the cloud paradigm, the resource allocation is done in a centralized manner, to balance the workload of running physical machines and to avoid congestion. But the cloud is placed away from the IoT devices, so the problem of Latency and Bandwidth arises [4] . In the fog computing environment, resource allocation is now days a bottleneck task. The Fog nodes are distributed desperately in the Fog environment, while in the cloud the computing nodes are distributed in a centralized data center. The resource requirements for the IoT applications are distinguished because the applications have different requirements of bandwidth, computing power, and storage capacity. Therefore, it is requisite to achieve resource allocation for the static resource requirements to attain the target of QoS. The purpose of resource planning is to find better resources as per the demand of applications for achieving lower processing delay [5].

B. HOW DO OPTIMIZATION ALGORITHMS IMPACT TASK MANAGEMENT?

Task management [6] is a strategy for allocating tasks to fog nodes/cloud servers efficiently. In the IoT-Fog Cloud environment number of tasks may be raised by devices, which further undergo computation. By efficient task management techniques, one can schedule the Fog/cloud resources successfully. Suppose "n=5 "is representing the number of tasks, which is generated by the IoT devices [7]. These five tasks need to allocate to fog devices or maybe to the cloud server for computation. Devices in the fog environment are highly heterogeneous. so, there is a requirement for a useful strategy that helps task management in the Fog environment. Following any designed task scheduling technique helps the efficient tasks management in Fog environment. If task management strategy is chosen wisely then QoS parameters like cost, makespan, energy consumption, latency [8], and security can be achieved.

Optimization algorithms iteratively search for optimal solutions from a set of solutions. By comparing a new solution with the previous one optimal solution can be achieved. Similarly, in a Fog environment, searching for the best machines for the allocation of tasks may occur. So that problem of task management can be overcome [9].

Many traditional optimization algorithms like Min-Min, Max-Min, PSO, GA, RoundRobin, and FCFS are the basis of later/upcoming optimization algorithms. Most of the researchers have provided Bio-inspired optimization algorithms like PSO, GA, Cat-Swarm, Moth-flame optimization algorithm, Dolphin Partner Optimization algorithm, Grey-wolf, firefly, Bees-swarm, Cuckoo, lion optimization algorithms, etc.

C. FOG COMPUTING ARCHITECTURE

Fig. 1 is showing the architecture of the IoT-Fog-Cloud environment. It consists of a three-tier structure which includes: the IoT device layer, Fog computing layer, and Cloud layer. The fog layer is in between the cloud layer and the IoT layer.

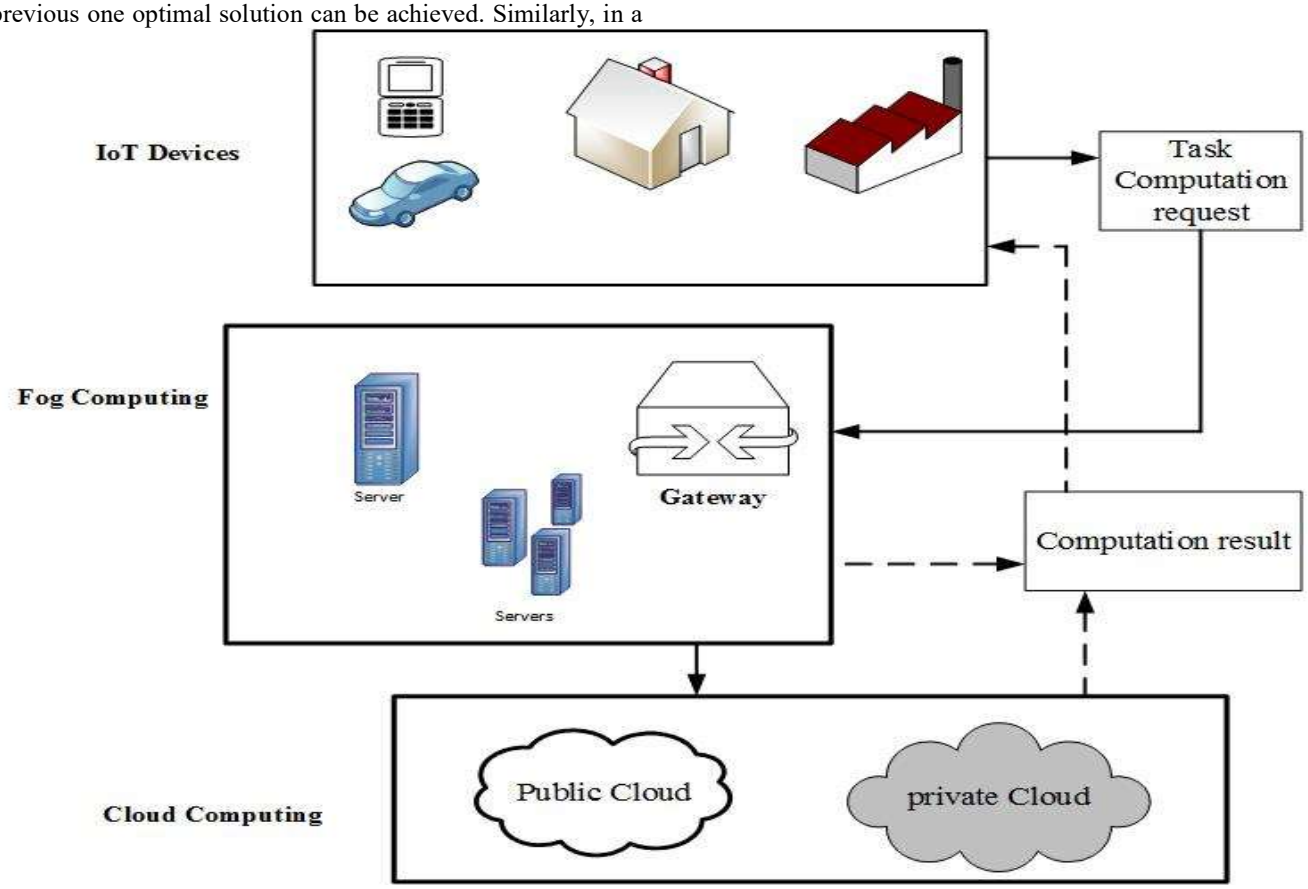

Fig. 1: Fog Computing Architecture

Cloud layer: Cloud layer consists of large computing servers and storage computation devices. Cloud can be any form like a public cloud for anybody access, it can be a private cloud for limited user access or it can be a hybrid cloud combination of both.

Fog layer: The fog layer consists of heterogeneous Fog nodes, having limited computation and storage capacity. It exists at the edge of the network, which helps it for improving bandwidth, computation cost, etc.

IoT device layer: This layer occupies the end-user interface, and includes devices and sensors. Sensors device collect user information. This information sends to the upper layer for processing.

D. THE MAJOR CONTRIBUTION OF THE WORK

1. Heuristic and meta-heuristic algorithms are investigated,

simulated and evaluated for QoS parameters using work Flow Simulator.

1. Investigation of 5 types of montage data set is done with all techniques, which depicts the performance execution with smaller to larger tasks in the system.
2. Comparative performance evaluation of state-of-the-art techniques is presented on cost, makespan, and energy consumption QoS parameters.

E. ORGANIZATION OF THE WORK

In this work, section II describes the related work of task management in the IoT-Fog-Cloud environment is done. Section III provides a taxonomy for Task Management optimization techniques to attain QoS parameters. In section IV description of simulation and parameter setting is provided. The result and discussion part are discussed in section V. A conclusion of this work is provided in section VI.

II. RELATED WORK

Salim Bitam et al. [10] described an algorithm based on Bees life named BLA. Researchers addressed the problem of Job scheduling in the Fog environment in their work. The authors discussed the trade-off between memory utilization and execution time of the CPU. The authors made a comparison of the proposed technique with PSO and GA and successfully outperforms both techniques in terms of memory and CPU execution time. Saniah Rehman et al. [11] proposed a technique of load balancing for efficient utilization of resources. Researchers used the technique of the Min-Min algorithm for efficient management. Resources are allocated first to those tasks which have minimum execution time as per the protocol of the Min-Min algorithm. The proposed approach is compared with the Round-Robin algorithm. The proposed technique outperforms the Round-Robin algorithm on parameter cost. Bushra jamil et al. [12] provided a technique of job scheduling for achieving optimal QoS parameters delay, energy consumption, and network usage. Researches provide a case study on health management to show the efficiency of the proposed algorithm. The authors achieved optimal results in comparison with the FCFS approach by 32% of delay and 16% of network usage. Mostafa Ghobaei-Arani et al. [13] described a technique of moth-flame for task scheduling in a Fog environment. By using this technique authors focussed on efficient task allocation to achieve optimal QoS requirements in the Fog environment. The objective function of work is to minimize the transfer time and task execution time. For showing the efficiency of work, the comparison is in contrast with PSO, BLA, and NSGA-2 techniques and validated the results of the proposed technique. Claudia Canali et al. [14] addressed the problem of distribution of data stream to fog nodes received from sensors. For the solution to this problem, the authors worked in two folds. The first optimization model considers not only the load on the fog nodes but also considers communication latency between fog nodes and sensors. second, a scalable genetic algorithm is proposed to address the problem. for the validation of the results, experiments were conducted on the smart cities problem. Narayana Potu et al. [15] proposed an extended PSO technique for optimizing resource scheduling in the Fog computing environment. Researchers used the extra gradient method in this technique to optimize the problem of task scheduling. the proposed technique is compared with TCaS, BLA, ideal PSO, and MPSO on parameter cost and makespan. Researchers have noticed the improvement in doing a comparison with existing techniques. Amit Kishor et al. [16] discussed the technique of task offloading by proposing a smart ant colony optimization algorithm. In this work, Researchers addressed the problem of latency when the task is going to offload from IoT devices to Fog nodes. The proposed technique is compared with modified PSO, BLA, RoundRobin, and throttled algorithm. The smart ant colony technique conquers all the existing techniques on parameter task offloading time. Fatma M. Talaat et al. [17] proposed a method of EPRAM (Effective prediction and resource allocation method) in the healthcare system. To control EPRAM, the authors concentrated on the method of Resource allocation method, Data processing method, and effective prediction method. These all techniques assist to preserve persons from high-threat diseases by the method of deep reinforcement learning and PNN. This designed method helps to reduce the makespan, and enhance load balancing and resource allocation. Noé Godinho et al. [18] describe the idea of services offloading and communication to the Fog environment for efficient QoS. In the proposed method researchers described the idea of MILP (Mixed integer linear programming) and mapping of VN to the network for leading energy and bandwidth in the Fog environment. The designed method successfully gets the optimal results. Jyoti Bisht et al. [19] proposed the method of extended min-min scheduling algorithm which assist the researcher to enhance makespan, cost, load balancing, and energy utilization in a Fog-edge environment. For the validation of the result, the designed method in contrast with the ELBMM & min-min algorithm, and the proposed method conquer both the techniques on the mentioned parameters.

III. TASK MANAGEMENT OPTIMIZATION TECHNIQUES TO ATTAIN QOS PARAMETERS

QoS in a system may be achieved through techniques of heuristic and meta-heuristic as shown in Fig. 2. Many researchers have provided various methods [20] under these categorized techniques. Min-Min, Max-Min, FCFS, Round-Robin, etc. fall under heuristic categories. Similarly, PSO, GA, BLA, ACO, etc. fall under Metaheuristic categories. Following heuristic and metaheuristic techniques, many researchers have done task management to attain QoS parameters like cost, makespan, time, response time, throughput, etc. in the Fog environment [21-23].

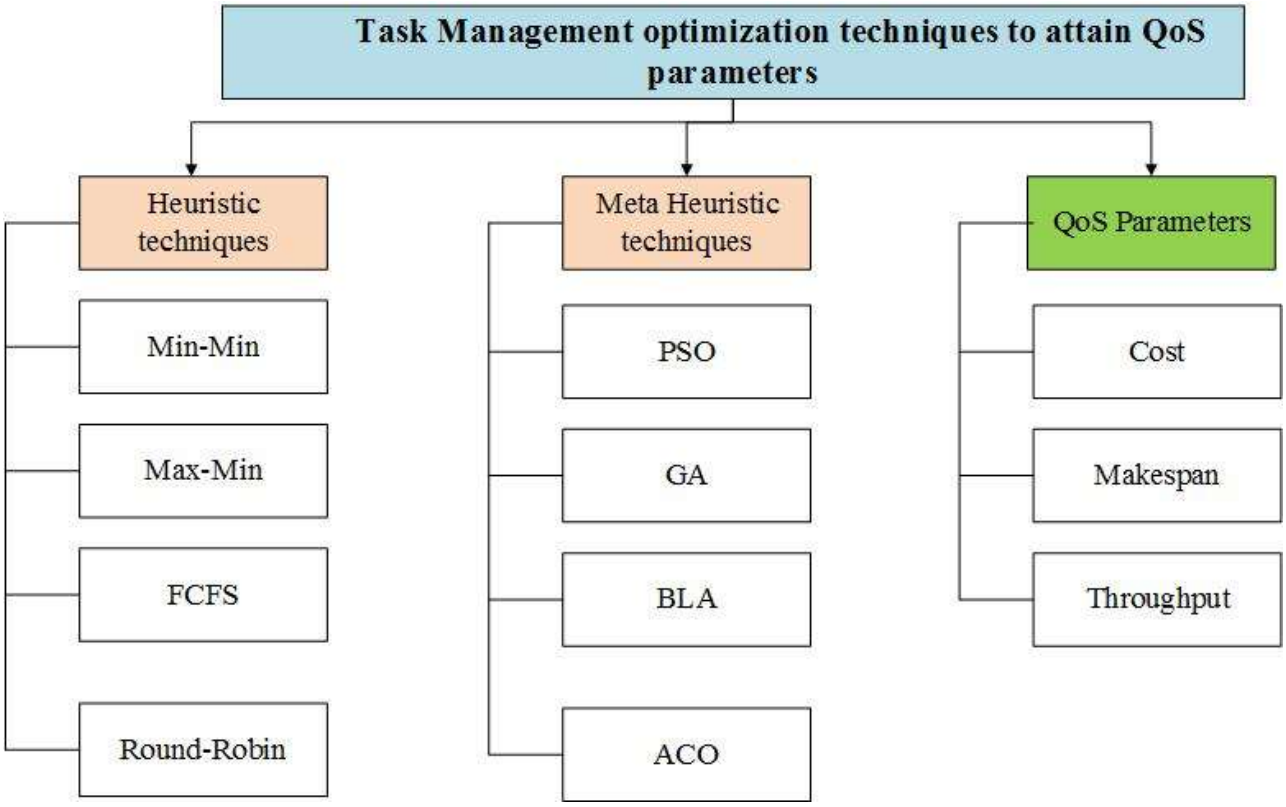

Fig. 2: Taxonomy of Task management

a) Heuristic technique: This technique is meant to be problem dependent. Heuristic algorithms may be used only for specified problems. Heuristic algorithms are more focused on speed rather than accuracy in the system. In the heuristic technique, one can guess a solution to a problem but he does not know how close this is to a solution to any problem [24]. Traditionally heuristic algorithms are used in many applications. Selecting the random number to pivot in quicksort is one example of the application of the heuristic algorithm. In Figure, 2 authors have mentioned some of the traditional heuristic algorithms.

   i. Min-Min Technique**:** Min-Min is a type of heuristic technique; in a Fog environment this technique is used by many researchers for task management. The problem of resource management is still an issue in the Fog system. Many authors allocated VM to task as per policies of the Min-Min algorithm those tasks have minimum execution time, the machine will be allocated to that task first. The execution time of a task is computed based on the number of instructions in a task. As an application Min-Min algorithm is used in Smart-cities during power consumption in cities.

   ii. Max-Min Technique**:** This technique is providing priority to larger tasks over smaller tasks. In the Fog system, those tasks that have a large number of instructions will get the priority first and those tasks that have a smaller number of instructions will get the lowest priority. The computation of Makespan in a system is examined by the implementation of the longest tasks.

   iii. FCFS Approach**:** FCFS works on the process of FIFO queue. Jobs that get the resources request first will get the allocation of resources first. In the Fog environment, optimal QoS can be achieved through the FCFS heuristic technique by managing the request queue of tasks. A drawback of the technique is if some longest tasks get in the request queue first then some small tasks have to wait for a long time until the longest tasks get finished.

   iv. Round-Robin technique: Round-Robin technique is a pre-emptive type FCFS approach.in Round-Robin technique CPU is allocated for quantum or for a particular time to tasks. If tasks fail to be completed in a given time then tasks need to wait in queue for the next turn. in the IoT-Fog-Cloud system, many researchers successfully get optimal cost and makespan by computing the expected completion time of the tasks.

b) Metaheuristic Techniques: This technique is meant to be problem independent. Metaheuristic techniques are not for specified problems. Using Meta-heuristic techniques researchers are solving many NP-hard problems. Unlike the heuristic technique, the meta-heuristic technique provides

some optimal solutions to the problem in the next steps. An example of Hill-Climb is one of the finest applications of metaheuristic technique, where during a hill climb as moves to the next steps, there is the assurance of reaching the target. Authors have provided various algorithms for these techniques like PSO, ACO, GA, BLA, etc.

i. PSO optimization algorithm: The particle swarm optimization technique is a type of meta-heuristic technique. It's based on the nature of swarm or particle agents that moves around in search space for solving the problems to obtain an optimal solution. The motion of a particle is advised through the particle's own best position and other's global best solution. Many applications like healthcare, agriculture, smart industries, etc. use the PSO technique for solutions in their field.

ii. GA optimization algorithm: The technique is based on the process of natural election. In this technique, there is a selection of individuals for reproduction to generate offspring for an upcoming generation. Genetic algorithm is working on techniques of crossover and mutation. Application of GA algorithms like DNA analysis, economics, aircraft design, etc.

iii. Bees life optimization algorithm: Bees life algorithm is inspired by bees life when they are searching for their food and find the best food out of search space. Multiple bees looking at multiple places for their daily food. Out of multiple choices best, one is selected an optimal solution from the search space. Similarly, the concept is used in a fog environment, out of given resources which best available resource is allocated to the task for execution.

iv. Ant Colony optimization algorithm: it's a part of the optimization algorithm that depends upon the behavior of the ant colony. This optimization technique is used in finding an optimal path in a given solution search space. Ants pull out a pheromone to find a path for food. Ants roam randomly in search space, and when they find food on the path. Ants use that path as a source path for food with the help of pheromone. The same technique is used in the fog environment on smart city applications where the task is allocated to the Fog nodes in a distributed manner.

C. QoS parameters**:** In a Fog environment, Fog devices are heterogeneous in terms of memory, CPU, and other resources. Fog nodes in the Fog environment can be considered also mobile nodes. Nodes are distributed in an environment for efficient computation. But heterogeneity, mobility, and distributed structure make it difficult to achieve QoS parameters in the Fog environment [25,26]. Some of the QoS parameters are mentioned in **Figure 2** like cost, makespan, time, response time, etc. Efficient calculation of these parameters eventually depends on how resources are distributed to tasks [27,28]. Discussion on QoS parameters cost, makespan, time, and response time are done below:

I. Cost**:** The cost parameter is computed based on the computation done in the Fog system by machines. Cost is included based on memory cost, bandwidth cost, and processing cost or CPU utilization cost. Cost of computation of Task (τ_k^i) may be considered using equation 1:

$$cost\,(\tau_k^i) = cp(\tau_k^i) + cm(\tau_k^i) + cb(\tau_k^i) \quad (1)$$

computation cost is computed by the sum of processing cost, memory cost, and bandwidth cost. processing cost using equation 3, is a cost of CPU usage cost ($\boldsymbol{\zeta 1}$) of each node n_i, and execution time is defined using equation 2:

$$Execution\text{-}time = \frac{Length-of-task}{cpu-rate} \quad (2)$$

Execution time in a system is computed by the number of instructions computed by the CPU based on fixed CPU frequency.

$$cp(\tau_k^i) = \zeta 1 * Execution\text{-}time \quad (3)$$

Cost of memory usage may be computed by the amount of memory required by tasks ($Mem\tau_k^i$) for computation with memory usage cost ($\boldsymbol{\zeta 2}$). Memory usage cost may be computed as using equation 4 below:

$$cm(\tau_k^i) = \zeta 2 * Mem(\tau_k^i) \quad (4)$$

Task requires bandwidth for computation in a Fog environment. The amount of bandwidth requires depends upon the size of input and output files. The cost of bandwidth usage may be computed as the bandwidth required by the tasks $band(\tau_k^i)$ at each node n_i with bandwidth usage cost parameter ($\boldsymbol{\zeta 3}$). Bandwidth usage cost may be computed as using equation 5 below:

$$cb(\tau_k^i) = \zeta 3 * band(\tau_k^i) \quad (5)$$

II. Makespan: Makespan is a time between when tasks arrive for computation to all tasks completed. By improving the execution time of tasks, authors can improve the makespan of the system. Makespan may be calculated using equation 6:

$$\text{Makespan} = \min\{\text{Execution-time}\} \quad (6)$$

Execution time in a system may be calculated as mentioned in equation 2. Minimum makespan may also be considered as each task execute at the same time using equation 7.

$$\text{Makespan}_{Min} = \text{Execution-time}(N_1) = \text{------} = \text{Execution-time}\,(N_m) \quad (7)$$

III. Throughput (ϒ): Throughput is meant to be how the system is efficiently performing for a given bandwidth. Efficiency will be calculated by useful time (U_{time}) over the Total time (T_{time}) of the system. Useful time (U_{time})will be the time the system performs without any delay. Efficiency of system may be computed using equation 8.

$$\varepsilon = \frac{Utime}{Ttime} \qquad (8)$$

Then throughput is defined as system efficiency **ε** over a provided bandwidth **β** using equation 9.

$$\text{Throughput } (\Upsilon) = \varepsilon * \beta \qquad (9)$$

IV. SIMULATION PARAMETER AND SETTING

This section elaborates on the simulation strategies and parameter settings used in this work. Simulation has been performed on the Fog-workflow sim toolkit [29] with a CPU Core i3-2370M @ 2.40GHz, 8GB RAM, and operating system windows 7. For the whole scenario to work, each server and node has its own set of memory and processing capacity in MIPS. For simulation, researchers set the parameters, Number of Fog nodes=10 nodes, Number of cloud servers= 3, processing capacity of Fog nodes= 1300 MIPS, and processing capacity of Cloud Nodes = 1600 MIPS.
in this work, Parameter setting for PSO technique are Number of particles=20, iteration=100, c1=2.05, c2=20.3, and inertia weight=0.5. For GA technique population size=50, No. of iterations=100, cross rate=0.8, and mutation=0.1.

V. RESULT AND DISCUSSION

This section describes the comparison of parameter makespan, cost, and energy consumption between Min-Min, Max-Min, FCFS, RoundRobin, PSO, and GA.

As shown in Fig. 3, a comparison of parameter makespan is done between all heuristic and meta-heuristic techniques for 60-300 tasks. All comparison is done on 5 types of montage data sets. Heuristic technique FCSF outperforms all other Min-Min, Max-Min, and Round-Robin techniques. Improvement of 3-6% is shown with the FCFS technique in comparison to all heuristic techniques. For a higher number of tasks 200 tasks and 300 tasks, the FCFS technique performs much better in comparison to a lower number of tasks. Besides, for meta-heuristic techniques PSO and GA. PSO technique is performing better concerning GA. An improvement of 1.5%-2.5% is noticed with PSO in comparison to GA. The Metaheuristic technique is performing better for the lower number of tasks. For a higher number of tasks, less improvement is seen with PSO on GA.

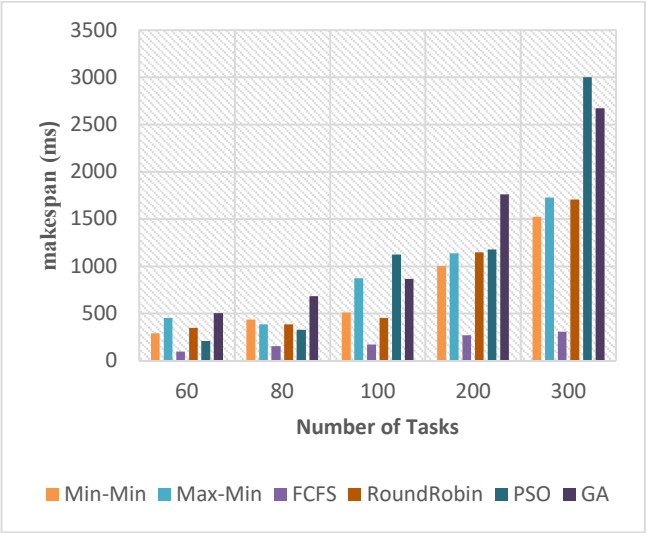

Fig. 3: Makespan Comparison between techniques

A comparison of cost parameters is done for all techniques as shown in Fig. 4. Total cost is depending on processing cost, bandwidth cost, and memory cost as shown in equation 1. Total cost in heuristic technique is less for FCFS technique w.r.t other techniques. Cost is computed in Grid $ in exchange for currency unit. Cost is less up to 1.5%-2% for FCFS technique in comparison with Min-Min, Max-Min, and Round-Robin. Whereas in the Meta-heuristic technique, GA outperforms PSO by about 1.5%-2%. For a high number of tasks such as 200 and 300, less cost is seen for GA on PSO. A comparison of energy consumed by heuristic and meta-heuristic techniques is shown in Fig. 5. The Min-Min technique consumes much less energy in contrast to Max-Min, FCFS, and Round-Robin techniques. Min-Min consumes approx. 20-22% less energy in comparison to all techniques for heuristic strategy. Besides for metaheuristic technique, the GA technique is consuming less energy in a Fog environment in contrast to the PSO technique. In the IoT-Fog-Cloud environment, GA consumes approx. 6-7% less energy in contrast to the PSO technique

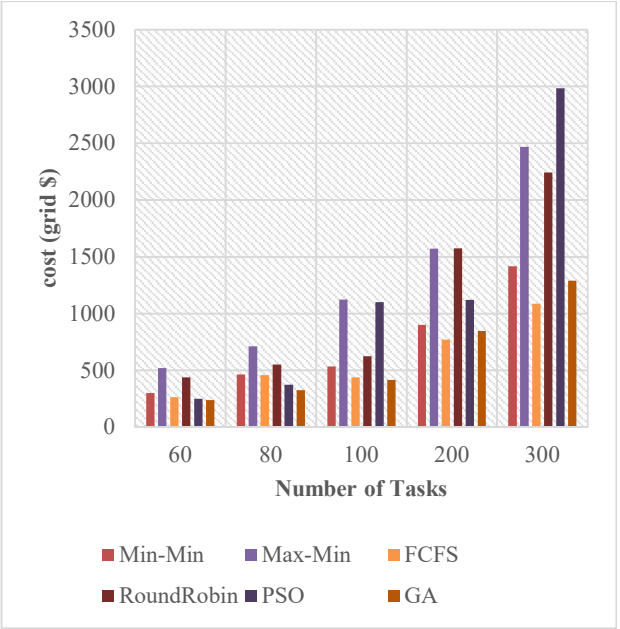

Fig. 4: Cost Comparison between techniques

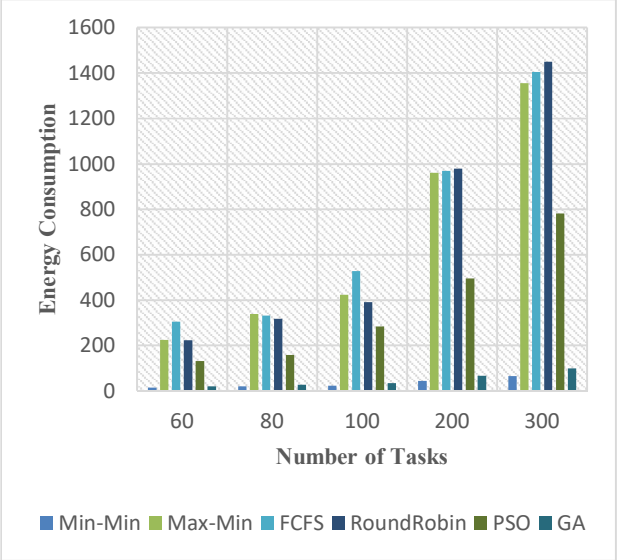

Fig. 5: Energy consumed Comparison between techniques

VI. CONCLUSION

This work focuses on, the discussion on some of task management and resource scheduling techniques. Their various QoS parameters and their impact is also discussed in Fog environment. Montage workload for tasks is considered to simulate the Fog environment. Various heuristics and meta-heuristic techniques are implemented on workflow sim to show the effectiveness of state-of-the-art techniques. These techniques are evaluated on makespan, cost and energy consumed. The experimental setup shows that the techniques, like PSO and GA, has shown less significant improvements with larger number of tasks for makespan. For cost computation of all execution of tasks on Fog nodes is optimal in case of GA based heuristics techniques *w.r.t* Min-Max, Max-Min, FCFS, Round robin and PSO. Then for energy consumption, PSO and GA techniques has out-performed the other techniques with lesser to larger number of tasks. Thus, heuristics and meta heuristics are significant in task management in Fog environment to utilize the limited resources. Thus, in future more task management techniques are required for optimizing the utilization of limited resources so that computing environment can support the real-life network traffic requests.

DECLARATION OF INTERESTS

The authors declare that they have no known competing financial interests or personal relationships that could have appeared to influence the work reported in this paper.

REFERENCES

[1] Elgendy, I. A., Zhang, W. Z., He, H., Gupta, B. B., El-Latif, A., & Ahmed, A. (2021). Joint computation offloading and task caching for multi-user and multi-task MEC systems: reinforcement learning-based algorithms. Wireless Networks, 27(3), 2023-2038.

[2] Kumar, Sumit, and Rajeev Tiwari. "An efficient content placement scheme based on normalized node degree in content centric networking." Cluster Computing 24.2 (2021): 1277-1291.

[3] Tiwari, Rajeev, and Neeraj Kumar. "A novel hybrid approach for web caching." 2012 Sixth International Conference on Innovative Mobile and Internet Services in Ubiquitous Computing. IEEE, 2012.

[4] Tiwari, Rajeev, et al. "Automated parking system-cloud and IoT based technique." International Journal of Engineering and Advanced Technology (IJEAT) 8.4C (2019): 116-123.

[5] Wang, S., Zhao, T., & Pang, S. (2020). Task scheduling algorithm based on improved firework algorithm in fog computing. IEEE Access, 8, 32385-32394. DOI: 10.1109/ACCESS.2020.2973758

[6] Naha, R. K., Garg, S., Chan, A., & Battula, S. K. (2020). Deadline-based dynamic resource allocation and provisioning algorithms in fog-cloud environment.,Future Generation Computer Systems, 104 , 131-141.

[7] Khan, E., Garg, D., Tiwari, R., & Upadhyay, S. (2018, February). Automated toll tax collection system using cloud database. In 2018 3rd International Conference On Internet of Things: Smart Innovation and Usages (IoT-SIU) (pp. 1-5). IEEE.

[8] Tiwari, R., & Kumar, N. (2012, December). Dynamic Web caching: For robustness, low latency & disconnection handling. In 2012 2nd IEEE International Conference on Parallel, Distributed and Grid Computing (pp. 909-914). IEEE.

[9] Tiwari, R., Kumar, K., & Khan, G. (2010, November). Load balancing in distributed web caching: a novel clustering approach. In AIP Conference Proceedings (Vol. 1324, No. 1, pp. 341-345). American Institute of Physics.

[10] Salim Bitam, Sherali Zeadally & Abdelhamid Mellouk (2018) Fog computing, job scheduling optimization based on bees swarm, Enterprise Information Systems, 12:4, 373-397, DOI: 10.1080/17517575.2017.1304579.

[11] Rehman, S., Javaid, N., Rasheed, S., Hassan, K., Zafar, F., & Naeem, M. (2018, October). Min-min scheduling algorithm for efficient resource distribution using cloud and fog in smart buildings. In International Conference on Broadband and Wireless Computing, Communication and Applications (pp. 15-27). Springer, Cham.

[12] Jamil B, ShojafarM, Ahmed I, Ullah A, Munir K, Ijaz H. A job scheduling algorithm for delay and performance optimization in fog computing. Concurrency Computat Pract Exper. 2019;e5581. https://doi.org/10.1002/cpe.5581.

[13] Ghobaei-Arani M, Souri A, Safara F, Norouzi M. An efficient task scheduling approach using moth-flame optimization algorithm for cyber-physical system applications in fog computing. Trans Emerging Tel Tech. 2019;e3770. DOI: 10.1002/ett.3770.

[14] Canali, C., & Lancellotti, R. (2019). GASP: genetic algorithms for service placement in fog computing systems. Algorithms, 12(10), 201.

[15] Potu N, Jatoth C, Parvataneni P. Optimizing resource scheduling based on extended particle swarm optimization in fog computing environments. Concurrency Computat Pract Exper. 2021;e6163. DOI: 10.1002/cpe.6163.

[16] Kishor, A., & Chakarbarty, C. (2021). Task offloading in fog computing for using smart ant colony optimization. Wireless Personal Communications, 1-22.

[17] Talaat, F. M. (2022). Effective prediction and resource allocation method (EPRAM) in fog computing environment for smart healthcare system. Multimedia Tools and Applications, 81(6), 8235-8258.

[18] Godinho, N., Silva, H., Curado, M., & Paquete, L. (2022). A reconfigurable resource management framework for fog environments. Future Generation Computer Systems.

[19] Bisht, J., & Vampugani, V. S. (2022). Load and Cost-Aware Min-Min Workflow Scheduling Algorithm for Heterogeneous Resources in Fog, Cloud, and Edge Scenarios. International Journal of Cloud Applications and Computing (IJCAC), 12(1), 1-20.

[20] Singh, S. P. (2022). Effective Load Balancing Strategy Using Fuzzy Golden Eagle Optimization in Fog Computing Environment. Sustainable Computing: Informatics and Systems, 100766.

[21] Tiwari, R. (2010). Gulista khan,"Load Balancing through distributed Web Caching with clusters". Proceeding of the CSNA, 46-54.

[22] Kumar, S., & Tiwari, R. (2021). Dynamic popularity window and distance-based efficient caching for fast content delivery applications in CCN. Engineering Science and Technology, an International Journal, 24(3), 829-837.

[23] Chithaluru, P., Tiwari, R., & Kumar, K. (2021). Performance analysis of energy efficient opportunistic routing protocols in wireless sensor network. International Journal of Sensors Wireless Communications and Control, 11(1), 24-41.
[24] Sangeetha, A., & Rajendran, T. (2022). Supervised Vector Machine Learning with Brown Boost Energy Efficient Data Delivery In MANET. Sustainable Computing: Informatics and Systems, 100761.
[25] Chithaluru, P., Tiwari, R., & Kumar, K. (2021). Arior: Adaptive ranking based improved opportunistic routing in wireless sensor networks. Wireless Personal Communications, 116(1), 153-176.
[26] Tiwari, R., Sille, R., Salankar, N., & Singh, P. (2022). Utilization and Energy Consumption Optimization for Cloud Computing Environment. In Cyber Security and Digital Forensics (pp. 609-619). Springer, Singapore.
[27] Tiwari, R., Mittal, M., Garg, S., & Kumar, S. (2022). Energy-Aware Resource Scheduling in FoG Environment for IoT-Based Applications. In Energy Conservation Solutions for Fog-Edge Computing Paradigms (pp. 1-19). Springer, Singapore.
[28] Varshney, S., & Singh, S. (2018). A survey on resource scheduling algorithms in cloud computing.,International Journal of Applied Engineering Research, 13(9), 6839-6845.
[29] Liu, Xiao, et al. "FogWorkflowSim: an automated simulation toolkit for workflow performance evaluation in fog computing." 2019 34th IEEE/ACM International Conference on Automated Software Engineering (ASE). IEEE, 2019.

Gaurav Goel was born on January 09, 1987, in India. He has done his B.Tech from Haryana Engineering College Jagadhri, India in the stream Computer Science and Engineering from 2004-to 2008. Further has completed his MTech in Computer Science and Engineering in 2014. Currently, the Author pursuing his Ph.D. in Computer Science and Engineering from UPES Dehradun, India in the area of Fog Computing. He has held the position of Assistant professor in Chandigarh Group of Colleges, Landran, India. He has a total Experience of 14 years.

Rajeev Tiwari is working as a Professor in SCS in UPES, Dehradun (India). He is a senior IEEE Member. He has done Ph.D. in CSE from Thapar Univeristy, Patiala (Punjab). He has more than 16 years of research and teaching experience. His broad area of research is Cloud Computing, MANET, VANET, QoS in wireless networks, Cache Invalidation Techniques, Internet of Things (IoT), Big Data Analytics and Machine Learning. He is also an expert in simulation and design of scenarios on NS2, SUMO and MOVE. He is an active member of ACM, IEI, IACSIT and IAENG. He has 40 + international publications in SCI, and Scopus indexed journals and conferences. His publications are majorly indexed in SCI, Scopus and DBLP. He has published two Patents also. He has enriched experience of organizing international conferences successfully. He has major roles as Organizing Chair, TPC chair, Co-Chair Secretory etc in NGCT 2016, NGCT 2017, NGCT 2018, NGCT 2019, ICACCA 2019, IC4S 2019 etc with Springer and IEEE. He has chaired many sessions in international conferences. He is a lead reviewer in SCI indexed journal of Springer, IEEE and ScienceDirect and international conferences. He has edited books and published book chapters also with international publishers. He has contributions in funded projects in field of IoT, Cloud and wireless network QoS.

A New Robust Adaptive Algorithm for Second Order Blind Source Separation

Zineb Bekhtaoui, Karim Abed-Meraim, Abdelkrim Meche, and Messaoud Thameri

Abstract—This paper deals with the adaptive blind source separation problem in presence of impulsive noise. New algorithms extending the well known SOBI method from batch to adaptive scheme are introduced. At first, the standard Gaussian noise case is considered, leading to our first algorithm referred to as Adaptive SOBI (A-SOBI). Later on, a robust version of A-SOBI, referred to as RA-SOBI is derived to handle the impulsive noise case. RA-SOBI relies on robust subspace tracking for the whitening stage together with robust correlation estimation for the separation stage. All proposed algorithms are of relatively low complexity and allow to achieve good separation quality as illustrated by our simulation results.

***Keywords*—Blind source separation, Adaptive algorithm, Impulsive noise, Robustness, Subspace tracking**

I. Introduction

Blind source separation (BSS) consists of the extraction of source signals from their observed mixtures without prior knowledge of the mixing matrix or its inputs. BSS is widely used in many signal processing applications, and a plethora of works have been devoted to develop solutions in different contexts and under different mixing models, e.g., [1–7]. In particular, second order statistics based methods are highly regarded due to their low computation load and efficiency to separate temporally coherent (colored) sources. These features make them suitable for adaptive scheme when dealing with streaming data. Several algorithms have been already dedicated to such an adaptive scheme including [4, 5, 8–13]. Most of existing algorithms consider noise as being Gaussian or negligible. However, in many applications the measurements are affected by impulsive noise or outliers, e.g., [21–23], in which context standard methods fail to achieve the BSS. To deal with impulsive noise, some authors have proposed robust batch BSS algorithms, e.g., [7, 14–18].

In this work, we propose to deal with both streaming data (i.e. adaptive scheme) and impulsive noise. Hence, a new approach that ensures both robustness and adaptivity is introduced based on second order decorrelation approach. At first, we consider only the streaming data case and introduce the adaptive Second Order Blind Identification (SOBI) algorithm [12] for the Gaussian noise case. In this algorithm, referred to as Adaptive SOBI (A-SOBI), the source separation is performed in two steps: whitening and joint diagonalization. The whitening is achieved using an adaptive Principal Components Analysis (PCA) algorithm followed by the joint diagonalization conducted on several non zero lag correlation matrices. Then, our Robust Adaptive SOBI (RA-SOBI) algorithm is derived via the use of robust PCA tracking algorithm [19] for the whitening step by minimizing a weighted least criterion. Moreover, to improve furthermore the robustness of the algorithm, we propose here to estimate the non zero lag correlation matrices, considered in the joint diagonalization step, via robust estimation techniques [24].

This paper is organized as follows: Objectives and problem formulation are stated in section II.. The A-SOBI algorithm is given in section III.. Section IV. introduces RA-SOBI algorithm, while section V. is dedicated to simulation results providing the evaluation of our algorithms effectiveness. Finally, our concluding remarks are given in section VI..

Notations: The conjugate transpose, the transpose, the conjugate, the inverse, and the trace operations are represented by $()^H$, $()^T$, $()^*$, $()^{-1}$, and $tr()$ respectively. a denotes a scalar, $\mathbf{a}$ denotes a vector, $\mathbf{A}$ denotes a matrix, $\|\cdot\|^2$ denotes the Euclidean norm, $\mathbf{I}$ represents the identity matrix, and $\mathbf{A}_{ij}$ represents the (i,j)-th element of $\mathbf{A}$.

II. Problem statement

Consider a streaming data of multivariate $n \times 1$ dimensional vectors $\mathbf{x}(t)$ corresponding to the noisy mixtures of $p < n$ sources, i.e. $\mathbf{s}(t) = [s_1(t), \cdots, s_p(t)]^T$, according to

$$\mathbf{x}(t) = \mathbf{A}\mathbf{s}(t) + \mathbf{n}(t) \tag{1}$$

where $\mathbf{A}$ is the unknown $n \times p$ mixing matrix assumed to be of full column rank and $\mathbf{n}(t)$ is the additive noise vector assumed to be of zero mean and spatially white with covariance $E(\mathbf{n}(t)\mathbf{n}^H(t)) = \sigma^2\mathbf{I}$. The zero mean source signals are assumed to be temporally coherent but mutually decorrelated, i.e. $E(s_i(t+\tau)s_j^*(t)) = \delta_{ij}\rho_i(\tau)$ where $\rho_i(\tau)$ represents the correlation function of the i-th source signal and δ_{ij} is the Kronecker index.

Our objective in this work is to exploit the statistical (mutual) decorrelation information of the sources to retrieve the latter

Manuscript received April 22, 2022; revised June 13, 2022.

Z. Bekhtaou and A. Meche are with Laboratoire Signaux et Images, University of Sciences and Technology of Oran Mohamed Boudiaf (USTOMB), B.P 1505, El M'Naouar - Bir el Djir- Oran, Algeria. (e-mails: zineb.bekhtaoui@univ-usto.dz, abdelkrim.meche@univ-usto.dz)

K. Abed-Meraim, IUF Member, is affiliated to PRISME Lab., University of Orleans, France. (e-mail: karim.abed-meraim@univ-orleans.fr)

M. Thameri is with Ecole Supérieure Ali Chabati, Réghaia, Alger, Algérie. (e-mail: m_thameri@hotmail.com)

Digital Object Identifier (DOI): 10.53907/enpesj.v2i1.86

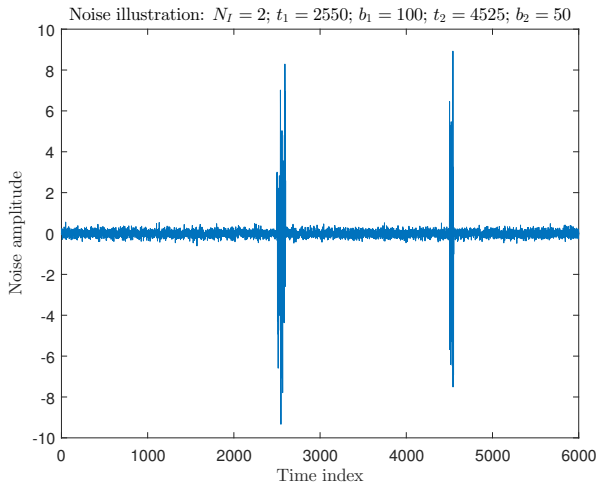

Fig. 1: Illustration of the noise $\mathbf{n}(t)$. The burst noise here appears in two occasions: at time 2500 and 4500 with duration 100 and 50, respectively.

from the observed data $\mathbf{x}(t)$ using only its second order statistics. Hence, this blind source separation problem consists of finding a separation matrix $\mathbf{B}$ so that (2) represents an estimation of the source vectors $\hat{\mathbf{s}}(t)$ up to permutation and scaling factors[2].

$$\hat{\mathbf{s}}(t) = \mathbf{B}\mathbf{x}(t) \tag{2}$$

As mentioned earlier, we consider here an adaptive scheme, where the model in (1) can be non-stationary but 'slowly' varying, and address the case where observed data is corrupted by impulsive noise. After considering first the adaptive scheme in a Gaussian noise case, we extend our algorithm to the burst noise[3] context modeled by additional centered Gaussian white noise with larger amplitudes occurring in short periods of time. The burst noise $\mathbf{n}(t)$ can therefore be written as

$$\mathbf{n}(t) = \mathbf{n}_G(t) + \sum_{i=1}^{N_I} u\Big(\frac{t-t_i}{b_i}\Big)\mathbf{n}_I^i(t) \tag{3}$$

where $\mathbf{n}_G(t)$ and $\mathbf{n}_I^i(t)$ are white centered Gaussian noises of variances $\sigma_G^2 << \sigma_I^2$. $\mathbf{n}_I^i(t)$ is weighted by $u(\cdot)$ a rectangular function which is used to describe the short duration appearance of the burst noise as illustrated by Fig. 1. N_I refers to the number of impulsive events, t_i is the center of the i-th impulsive event, and b_i is its duration.

III. A-SOBI ALGORITHM: GAUSSIAN NOISE CASE

A-SOBI algorithm consists of a separation approach by second order decorrelation, which proceeds in two steps: Whitening and diagonalization which are detailed next.

A. Whitening step

This step consists of projecting the observed vector $\mathbf{x}(t)$ onto the principal subspace spanned by the column vectors of the mixing matrix $\mathbf{A}$, with the purpose of transforming it into a unitary matrix. The used matrix in this transformation is called the whitening matrix $\mathbf{W}$.

[2] The latter are inherent indeterminacies of the BSS problem [3].

[3] This is the noise model used in our simulations, but other impulsive noise models can be considered as well [27].

In [3], it has been shown that the whitening matrix $\mathbf{W}$ can be computed from the eigen-decomposition of the covariance matrix of $\mathbf{x}(t)$, denoted $\mathbf{C}_x$, as follows:

$$\mathbf{C}_x = \mathbf{U}_s\mathbf{\Lambda}\mathbf{U}_s^H + \sigma^2\mathbf{I} \tag{4}$$
$$\mathbf{W} = \mathbf{\Lambda}^{-1/2}\mathbf{U}_s^H \tag{5}$$

where $\mathbf{U}_s$ and $\mathbf{\Lambda}$ are the matrices of the p principal eigenvectors and eigenvalues of the noise free covariance matrix. In an streaming data scheme, the exact eigenvectors and eigenvalues are replaced by their adaptive estimates using Givens-Orthogonal Projection Approximation Subspace Tracking (GOPAST) algorithm (see details in [12, 20]) according to:

$$\mathbf{W}(t) = \mathbf{\Lambda}(t)^{-1/2}\mathbf{U}_s^H(t) \tag{6}$$

The estimates of the principal components were obtained by using the linear cost GOPAST algorithm [20], i.e. its cost is $O(np)$ flops per iteration. This latter consists of estimating adaptively a basis $\mathbf{D}(t)$ of the principal subspace of the covariance matrix $\mathbf{C}_x$ with the GOPAST algorithm, starting with minimizing ($0 < \beta \leq 1$ being a chosen forgetting factor):

$$J\left(\mathbf{U}_s(t)\right) = \sum_{j=1}^{t} \beta^{t-j} \left\|\mathbf{x}(j) - \mathbf{D}(t)\mathbf{D}^H(t)\mathbf{x}(j)\right\|^2 \tag{7}$$

followed by an appropriate diagonalization using Givens rotations to get $\mathbf{U}_s(t)$ and $\mathbf{\Lambda}(t)$.

Note that since we are dealing with a slowly time varying system, β can be chosen to have a high value to insure faster convergence rate.

Remark: In GOPAST algorithm, $\mathbf{\Lambda}$ corresponds to the diagonal matrix of the principal eigenvalues of the covariance matrix $\mathbf{C}_x$. Implicitly, this means that the noise term (i.e. noise power σ^2) has been neglected in (4). In case, the latter cannot be considered as negligeable, one can estimate it as shown in [19] and replace in (6) $\mathbf{\Lambda}(t)$ by $\mathbf{\Lambda}(t) - \sigma^2(t)\mathbf{I}$.

B. Diagonalization step

After whitening, the mixing matrix is approximately reduced to a $p \times p$ unitary matrix denoted $\mathbf{U}^H(t)$ and hence the noiseless whitened signal can be written as $\tilde{\mathbf{x}}(t) = \mathbf{W}(t)\mathbf{x}(t) \approx \mathbf{U}^H(t)\mathbf{s}(t)$. To estimate the separation matrix $\mathbf{U}(t)$, A-SOBI uses a joint diagonalization of K correlation matrices corresponding to K chosen non-zero lags $\tau_1, \cdots, \tau_K$. The latter are adaptively estimated as:

$$\mathbf{R}_t(\tau_k) = \beta\mathbf{R}_{t-1}(\tau_k) + \hat{\mathbf{s}}(t)\hat{\mathbf{s}}^H(t-\tau_k) \tag{8}$$

Where $0 < \beta < 1$ is a forgetting factor and $\hat{\mathbf{s}}(t) = \mathbf{U}(t)\tilde{\mathbf{x}}(t)$. To achieve the joint diagonalization, it is first stated that the unitary separation matrix can be computed as a product of elementary Givens rotations:

$$\mathbf{U} = \prod_{l=1}^{p-1}\prod_{m=l+1}^{p} \mathbf{G}_{l,m}(\theta,\phi) \tag{9}$$

where $\mathbf{G}_{l,m}(\theta,\phi)$ is a $p \times p$ matrix equal to the identity except for its (l,l), (l,m), (m,l) and (m,m) entries. It is given by:

$$\mathbf{G}_{l,m}(\theta,\phi) = \begin{bmatrix} 1 & \cdots & 0 & \cdots & 0 & \cdots & 0 \\ \vdots & \ddots & \vdots & & \vdots & & \vdots \\ 0 & \cdots & c & \cdots & -s^* & \cdots & 0 \\ \vdots & & \vdots & \ddots & \vdots & & \vdots \\ 0 & \cdots & s & \cdots & c & \cdots & 0 \\ \vdots & & \vdots & & \vdots & \ddots & \vdots \\ 0 & \cdots & 0 & \cdots & 0 & \cdots & 1 \end{bmatrix} \quad (10)$$

where $c = \cos(\theta)$ and $s = \sin(\theta)e^{-j\phi}$. Thanks to the mutual decorrelation of the source signals, the separation is achieved when the correlation matrices $\mathbf{R}(\tau_k)$ are diagonalized (see [3] for more details). To perform the latter diagonalization in an adaptive way, one multiplies at each time step $\mathbf{R}(\tau_k)$ at its left and right sides by the elementary Givens rotation $\mathbf{G}(t)$ according to:

$$\mathbf{R}'(\tau_k) = \mathbf{G}(t)\mathbf{R}(\tau_k)\mathbf{G}^H(t) \quad (11)$$

The rotation indices l and m are selected to be the corresponding indices of the entries of largest amplitude according to:

$$(l,m) = \arg \max_{\{(i,j)|i<j\}} \sum_{k=1}^{K} |\mathbf{R}_{ij}(\tau_k)| \quad (12)$$

Remark: Another way to select rotation indices (l,m) at time t would be to visit periodically along the iterations all entries of the correlation matrices, according to:

$$(l,m) = \begin{cases} (l', m'+1) & \text{if } m < p \\ (l'+1, l'+2) & \text{if } m = p \text{ and } l' < p-1 \\ (1,2) & \text{if } m = p \text{ and } l' = p-1 \end{cases} \quad (13)$$

(l', m') being the chosen indices at time $t-1$. Also, instead of one single rotation per time instant, one can use two rotations with indices chosen according to the previous two methods in order to increase the algorithm's convergence rate, at the cost of increased computational complexity.

Finally, the rotation angles are obtained by minimizing the sum of off diagonal elements of the K considered correlation matrices:

$$(\theta,\phi) = \arg\min_{\theta,\phi} \sum_{a\neq b} \sum_{k=1}^{K} |\mathbf{R}'_{ab}(\tau_k)|^2 \quad (14)$$

This is proven to be equivalent to solving

$$(\theta,\phi) = \arg\max_{\theta,\phi} \mathbf{v}^H \mathbf{F}\mathbf{F}^H \mathbf{v} \quad (15)$$

where

$$\mathbf{v} = \begin{bmatrix} \cos(2\theta) \\ \sin(2\theta)\cos(\phi) \\ \sin(2\theta)\sin(\phi) \end{bmatrix}$$

and

$$\mathbf{F} = \begin{bmatrix} \mathbf{R}_{ll}(\tau_1) - \mathbf{R}_{mm}(\tau_1) & \cdots & \mathbf{R}_{ll}(\tau_K) - \mathbf{R}_{mm}(\tau_K) \\ 2\Re\left(\mathbf{R}_{lm}(\tau_1)\right) & \cdots & 2\Re\left(\mathbf{R}_{lm}(\tau_K)\right) \\ 2\Im\left(\mathbf{R}_{lm}(\tau_1)\right) & \cdots & 2\Im\left(\mathbf{R}_{lm}(\tau_K)\right) \end{bmatrix}$$

$\Re(\cdot)$ and $\Im(\cdot)$ denote the real and imaginary parts of their argument and $\mathbf{R}_{lm}(\tau_k)$ is the (l,m)-th entry of matrix $\mathbf{R}(\tau_k)$. An optimal solution is finally given by $\mathbf{v} = [v_1, v_2, v_3]^T = sign(u_1)\mathbf{u}$ (u_1 being the 1^{st} entry of $\mathbf{u}$) where $\mathbf{u}$ is the unit-norm eigenvector corresponding to the principal eigenvalue of matrix $\mathbf{F}\mathbf{F}^H$. The angle parameters are finally obtained as:

$$c = \sqrt{\frac{v_1+1}{2}} \quad \text{and} \quad s = \frac{v_2 - jv_3}{2c} \quad (16)$$

IV. RA-SOBI: Impulsive noise case

Here, we extend the previous algorithm and propose a robust version to deal with impulsive noise.

To do so, we modify A-SOBI algorithm in two spots:

- First, we replace the GOPAST algorithm with a more robust one to estimate the eigen components of the covariance matrix $\mathbf{C}_x(t)$.
- We apply the diagonalization step to robust estimates of the correlation matrices of the whitened signal $\mathbf{R}_t(\tau_k)$.

These two steps are detailed next.

A. *Robust whitening*

In order to estimate the principal components used in the whitening step, we propose here to use the recently robust algorithms proposed in [19]: Givens-Mahalanobis-Fast Approximated Power Iteration (GMFAPI) and its low-cost version Givens-Hard Thresholding-Fast Approximated Power Iteration (GHTFAPI). These algorithms consist of minimizing, under unitary constraint, the following weighted least squares criterion in order to estimate the principal subspace of the covariance matrix $\mathbf{C}_x$ (represented by its $n \times p$ orthonormal basis $\mathbf{D}(t)$):

$$J\left(\mathbf{D}(t)\right) = \sum_{j=1}^{t} \beta^{t-j}\omega(j) \left\|\mathbf{x}(j) - \mathbf{D}(t)\mathbf{D}^H(t)\mathbf{x}(j)\right\|^2 \quad (17)$$

where $\omega(j)$ is a soft weighting (resp. hard thresholding) factor considered by GMFAPI (resp. GHTFAPI). This, implicitly, consists of using a robust instantaneous estimate of the covariance matrix $\mathbf{C}_x(t)$ according to

$$\mathbf{C}_x(t) = \beta\mathbf{C}_x(t-1) + \omega(t)\mathbf{x}(t)\mathbf{x}^H(t). \quad (18)$$

One can solve this minimization problem using the power iteration method resumed by the data compression expressed in (19) and the orthonormalization (20)

$$\mathbf{C}_{xy}(t) = \mathbf{C}_x(t)\mathbf{D}(t-1) \quad (19)$$

$$\mathbf{D}(t)\mathbf{R}(t) = \mathbf{C}_{xy}(t) \quad (20)$$

A fast implementation is reached with the introduction of an intermediate $p \times p$ matrix denoted $\mathbf{Z}(t)$ representing an estimation of $\mathbf{C}_{yy}^{-1}(t)$ with $\mathbf{y}(t) = \mathbf{D}(t-1)^H\mathbf{x}(t)$. This implementation is summarized in table 1 One can refer to [19] for the detailed implementation.

Algorithm 1 (table 1): Subspace basis $\mathbf{D}(t)$ implementation

Initialization

$\mathbf{D}(0) = \begin{bmatrix} \mathbf{I}_p \\ 0_{(n-p)\times p} \end{bmatrix}$; $\mathbf{Z}(0) = \mathbf{I}_p$

for each time step do :

input vector $\mathbf{x}(t)$

$\mathbf{y}(t) = \mathbf{D}^H(t-1)\mathbf{x}(t)$

$\mathbf{h}(t) = \mathbf{Z}(t-1)\mathbf{y}(t)$

$\epsilon^2(t) = ||\mathbf{x}(t)||^2 - ||\mathbf{y}(t)||^2$

weight computation: see table 2

$\mathbf{g}(t) = \frac{\mathbf{h}(t)\omega(t)}{\beta + \mathbf{y}^H(t)\mathbf{h}(t)\omega(t)}$

$\tau(t) = \frac{\epsilon^2(t)}{1+\epsilon^2(t)||\mathbf{g}(t)||^2+\sqrt{1+\epsilon^2(t)||\mathbf{g}(t)||^2}}$

$\eta(t) = 1 - \tau(t)||\mathbf{g}(t)||^2$

$\mathbf{y}'(t) = \eta(t)\mathbf{y}(t) + \tau(t)\mathbf{g}(t)$

$\mathbf{h}'(t) = \mathbf{Z}^H(t-1)\mathbf{y}'(t)$

$\boldsymbol{\epsilon}(t) = \frac{\tau(t)}{\eta(t)}(\mathbf{Z}(t-1)\mathbf{g}(t) - (\mathbf{h}'(t)^H\mathbf{g}(t))\mathbf{g}(t))$

$\mathbf{Z}(t) = \frac{1}{\beta}(\mathbf{Z}(t-1) - \mathbf{g}(t)\mathbf{h}'(t)^H + \mathbf{e}(t)\mathbf{g}^H(t))$

$\mathbf{e}'(t) = \eta(t)\mathbf{x}(t) - \mathbf{D}(t-1)\mathbf{y}'(t)$

$\mathbf{D}(t) = \mathbf{D}(t-1) + \mathbf{e}'(t)\mathbf{g}^H(t)$

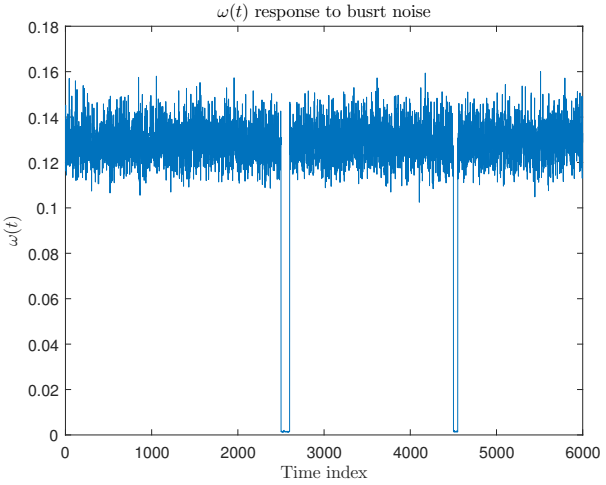

Fig. 2: Illustration of the weight criterion $\omega(t)$ when the burst noise appears in two occasions: at time 2500 and 4500 with duration 100 and 50, respectively.

Now, this criterion aims to mitigate the corrupted observations impact thanks to the weighting factor. Therefore, $\omega(t)$ should take small values when impulsive noises occur (see illustration in Fig. 2 for the weight factor of GMFAPI). To achieve that, GMFAPI and GHTFAPI algorithms use the following approaches:

1— GMFAPI: This algorithm uses the inverse of the Mahalanobis distance [25] to be the weight

$$\omega(t) = \frac{1}{d_M^2\Big(\mathbf{x}(t), \mathbf{C}_x^{-1}(t-1)\Big)} = \frac{1}{\mathbf{x}^H(t)\mathbf{C}_x^{-1}(t-1)\mathbf{x}(t)} \tag{21}$$

The following fast implementation of the latter was proposed in [19]

$$\mathbf{x}(t)^H\mathbf{C}_x^{-1}(t-1)\mathbf{x}(t) = \mathbf{y}(t)^H\mathbf{h}(t) + \frac{||\mathbf{x}(t)||^2 - ||\mathbf{y}(t)||^2}{\sigma_n^2(t-1)} \tag{22}$$

Where $\mathbf{h}(t) = \mathbf{Z}(t-1)\mathbf{y}(t)$. Now, the noise power $\sigma_n^2(t)$ can be estimated as

$$\sigma_n^2(t) = \frac{tr\big(\mathbf{C}_x(t)\big) - tr\big(\mathbf{C}_{yy}(t)\big)}{n-p} \tag{23}$$

Where $tr(\cdot)$ refers to the matrix trace operator. $T_x(t) = tr\big(\mathbf{C}_x(t)\big)$ and $T_y(t) = tr\big(\mathbf{C}_{yy}(t)\big)$ can be effectively calculated as

$$T_x(t) = \beta T_x(t-1) + \omega(t)||\mathbf{x}(t)||^2$$
$$T_y(t) = \beta T_y(t-1) + \omega(t)||\mathbf{y}(t)||^2$$

hence, the weight factor is obtained by $\omega(t) = 1/\delta'(t)$ where

$$\delta'(t) = \mathbf{y}(t)^H\mathbf{h}(t) + \frac{(||\mathbf{x}(t)||^2 - ||\mathbf{y}(t)||^2)(n-p)}{T_x(t-1) - T_y(t-1)} \tag{24}$$

2— GHTFAPI: To reduce further the computational cost of $\omega(t)$, a hard thresholding method was used in GHTFAPI. Indeed, considering the fact that $\epsilon^2(t) = ||\mathbf{x}(t)||^2 - ||\mathbf{y}(t)||^2$ represents approximately the instantaneous noise power, GHTFAPI uses it to determine whether to include the corresponding observation or not, according to

$$\begin{cases} \omega(t) = 0 & \text{if } \epsilon^2(t) > threshold(t) \\ \omega(t) = 1 & \text{if } \epsilon^2(t) < threshold(t) \end{cases} \tag{25}$$

where the threshold is determined using the well known Inter Quartile Range (IQR) method [26] applied on the last L samples. Hence, we define:

$$\tilde{\epsilon}(t) = \{\epsilon^2(t-L+1)\cdots\epsilon^2(t)\}$$
$$IQR(t) = Q3\big(\tilde{\epsilon}(t)\big) - Q1\big(\tilde{\epsilon}(t)\big)$$
$$threshold(t) = Q3\big(\tilde{\epsilon}(t)\big) + 1.5IQR(t) \tag{26}$$

with $Q1(\cdot)$ and $Q3(\cdot)$ representing respectively the lower and the upper quartiles.

One can refer to table 2 for an overview of the two methods regarding the computation of the weighting factor.

At this stage, we have a robust estimate of a basis of the principal subspace as well as an estimate of $\mathbf{Z}(t) \approx \mathbf{C}_{yy}^{-1}(t)$. Thus, we can perform an adaptive diagonalization on $\mathbf{Z}(t)$ using elementary Givens rotations to obtain the principal components $\mathbf{U}_s$ from the principal subspace basis and the principal eigenvalues Λ from $\mathbf{Z}(t)$. Indeed, we have $\mathbf{U}_s = \mathbf{DQ}$ where $\mathbf{Q}$ is a unitary matrix that can be expressed by $\mathbf{Q} = \prod \tilde{\mathbf{G}}_{\tilde{l},\tilde{m}}(\tilde{\theta},\tilde{\phi})$ and $\tilde{\mathbf{G}}_{\tilde{l},\tilde{m}}(\tilde{\theta},\tilde{\phi})$ is a Givens rotation as expressed in (10).

Now, to compute the latter, let us address the fact that the exact matrix $\mathbf{Z}'$ is diagonal. Hence, we define the Givens parameters so that the off diagonal elements of $\mathbf{Z}' = \mathbf{GZG}^H$ are minimized. That is to say:

$$(\tilde{\theta},\tilde{\phi}) = \arg\min_{\tilde{\theta},\tilde{\phi}} \sum_{a\neq b} |Z'_{ab}|^2 = \arg\max_{\tilde{\theta},\tilde{\phi}} |\tilde{\mathbf{v}}^T\tilde{\mathbf{f}}(t)|^2 \tag{27}$$

with

$$\tilde{\mathbf{v}} = \begin{bmatrix} \cos(2\tilde{\theta}) \\ \sin(2\tilde{\theta})\cos(\tilde{\phi}) \\ \sin(2\tilde{\theta})\sin(\tilde{\phi}) \end{bmatrix} \quad \text{and} \quad \tilde{\mathbf{f}}(t) = \begin{bmatrix} Z_{ll}(t) - Z_{mm}(t) \\ 2\Re\left(Z_{lm}(t)\right) \\ 2\Im\left(Z_{lm}(t)\right) \end{bmatrix}$$

Algorithm 2 (table 2): weighting factor computation

for each time step do :

Mahalanobis distance:

$\delta'(t) = \mathbf{y}(t)^H \mathbf{h}(t) + \frac{(||\mathbf{x}(t)||^2 - ||\mathbf{y}(t)||^2)(n-p)}{T_x(t-1) - T_y(t-1)}$

$\omega(t) = 1/\delta'(t)$

$T_x(t) = \beta T_x(t-1) + \omega(t)||\mathbf{x}(t)||^2$

$T_y(t) = \beta T_y(t-1) + \omega(t)||\mathbf{y}(t)||^2$

Hard thresholding:

$\tilde{\epsilon}(t) = [\epsilon^2(t-L+1) \cdots \epsilon^2(t)]$

$IQR(t) = Q3(\tilde{\epsilon}(t)) - Q1(\tilde{\epsilon}(t))$

$threshold(t) = Q3(\tilde{\epsilon}(t)) + 1.5IQR(t)$

if $\epsilon^2(t) < threshold(t)$ **then**

$\omega(t) = 1$

else

$\omega(t) = 0$

end if

Algorithm 3 (table 3): Whitening

Initialization

$\mathbf{D}(t)$ and $\mathbf{Z}(t)$ from Table 1

$(\tilde{l}, \tilde{m}) = (1, 2)$

Givens rotations:

1^{st} rotation:

Select rotation indices as in (28)

$\tilde{\mathbf{f}}(t) = \left[Z_{\tilde{l}\tilde{l}}(t) - Z_{\tilde{m}\tilde{m}}(t); 2\Re(Z_{\tilde{l}\tilde{m}}(t)); 2\Im(Z_{\tilde{l}\tilde{m}}(t))\right]^T$

$\tilde{\mathbf{v}} = sign(\tilde{f}_1(t))\tilde{\mathbf{f}}(t)/||\tilde{f}(t)||$

$c = \sqrt{\frac{\tilde{v}_1+1}{2}}$ and $s = \frac{\tilde{v}_2 - \tilde{v}_3}{2c}$

Determine $\tilde{\mathbf{G}}$ as in equation (10)

$\mathbf{Z}(t) = \tilde{\mathbf{G}}\mathbf{Z}(t)\tilde{\mathbf{G}}^H$

$\mathbf{D}(t) = \mathbf{D}(t)\tilde{\mathbf{G}}^H$

2^{nd} rotation

Select rotation indices as in (13)

Apply the same steps in lines: (5-10)

$\mathbf{W}(t) = \mathbf{Z}(t)^{1/2}\mathbf{U}_s^H(t)$

An optimal solution to that is

$$\tilde{\mathbf{v}} = [\tilde{v}_1, \tilde{v}_2, \tilde{v}_3]^T = sign(\tilde{f}_1(t))\tilde{\mathbf{f}}(t)/||\tilde{\mathbf{f}}(t)||$$

where $sign(\tilde{f}_1(t))$ refers to the sign of the first entry of $\tilde{\mathbf{f}}(t)$. The parameters c and s are defined as in (16) with replacing $\mathbf{v}$ by $\tilde{\mathbf{v}}$.

Then again, to determine the indices $(\tilde{l}, \tilde{m})$, we select the largest off diagonal element of $\mathbf{Z}(t)$:

$$(\tilde{l}, \tilde{m}) = \arg \max_{\{(a,b)|a<b\}} |Z_{ab}(t)| \quad (28)$$

Finally, for a better convergence speed, another rotation per iteration is performed using automatic sweeping as in (13).

The whitening can be performed as in table 3

B. Robust estimation of correlation matrices

To further enhance the robustness od th proposed algorithm, we propose to estimate the correlation matrices via robust estimation techniques.

Algorithm 4 (table 4): Joint diagonalization

Initialization

$\mathbf{W}(t)$ from Table 3 ; $\mathbf{U}(0) = \mathbf{I}_p$

for each time step do :

for $k = 1, \cdots, K$

$\hat{\mathbf{s}}(t - \tau_k) = \mathbf{U}(t)\mathbf{W}(t)\mathbf{x}(t - \tau_k); k = 1, \cdots, K$

$\mathbf{R}_t(\tau_k) = \beta\mathbf{R}_{t-1}(\tau_k) + \sqrt{\omega(t)\omega(t-\tau_k)}\hat{\mathbf{s}}(t)\hat{\mathbf{s}}^H(t-\tau_k)$

end for

determine (l, m) as in (12) or (13)

$$\mathbf{F} = \begin{bmatrix} \mathbf{R}_{ll}(\tau_1) - \mathbf{R}_{mm}(\tau_1) & \cdots & \mathbf{R}_{ll}(\tau_K) - \mathbf{R}_{mm}(\tau_K) \\ 2\Re(\mathbf{R}_{lm}(\tau_1)) & \cdots & 2\Re(\mathbf{R}_{lm}(\tau_K)) \\ 2\Im(\mathbf{R}_{lm}(\tau_1)) & \cdots & 2\Im(\mathbf{R}_{lm}(\tau_K)) \end{bmatrix}$$

$\mathbf{u} = eigs(\mathbf{F}\mathbf{F}^H, 1)$

$\mathbf{v} = sign(u_1)\mathbf{u}$

$c = \sqrt{\frac{\tilde{v}_1+1}{2}}$ and $s = \frac{\tilde{v}_2 - \tilde{v}_3}{2c}$

define $\mathbf{G}(t)$ as in (10)

for $k = 1, \cdots, K$

$\mathbf{R}(\tau_k) = \mathbf{G}(t)\mathbf{R}(\tau_k)\mathbf{G}^H(t)$

end for

$\mathbf{U}(t) = \mathbf{U}(t)\mathbf{G}^H(t)$

Hence, since we consider several correlation matrices with different time lags for the diagonalization step, it is important to take into account whether the observations at these time lags are corrupted or valid. Thus, we propose here to weight the estimates of the correlations with a combination of $\omega(t)$ and $\omega(t - \tau_k)$ to ensure the mitigation of erroneous data.

Hence, the correlation matrices are estimated as

$$\mathbf{R}_t(\tau_k) = \beta\mathbf{R}_{t-1}(\tau_k) + \sqrt{\omega(t)\omega(t-\tau_k)}\hat{\mathbf{s}}(t)\hat{\mathbf{s}}^H(t-\tau_k) \quad (29)$$

Therefore, RA-SOBI performs the diagonalization step exactly as A-SOBI by replacing the correlation matrices estimates in (8) by their robust ones given in (29) and its summary is given in table 4

V. Simulation results

In order to investigate our algorithms performance, we simulate the streaming data vectors $\mathbf{x}(t)$ of dimension $n = 8$ during $N = 6000$ time steps. Those observations are generated using $p = 3$ source signals corresponding to filtered complex circular white Gaussian processes by three AR filters of order 1 with respective coefficients $a_1 = 0.95\exp(j0.5)$, $a_2 = 0.75\exp(j0.7)$ and $a_3 = 0.55\exp(j0.3)$.

These signals are then mixed and corrupted with additive white centered Gaussian noise $\mathbf{n}_G(t)$ imposing an SNR of $5dB$.

We run $M = 100$ Monte Carlo simulations for all scenarios and we evaluate the algorithms performance using the mean rejection level defined in [3] as:

$$I(t) = \frac{1}{M}\sum_{m=1}^{M}\left(\sum_{i=1}^{p}\frac{\sum_{j\neq i}|\mathbf{L}_{ij}(t)|^2}{|\mathbf{L}_{ii}(t)|^2}\right) \quad (30)$$

Where $\mathbf{L}(t) = \mathbf{B}(t)\mathbf{A}(t)$ is close to a diagonal matrix (after removing the permutation indeterminacy).

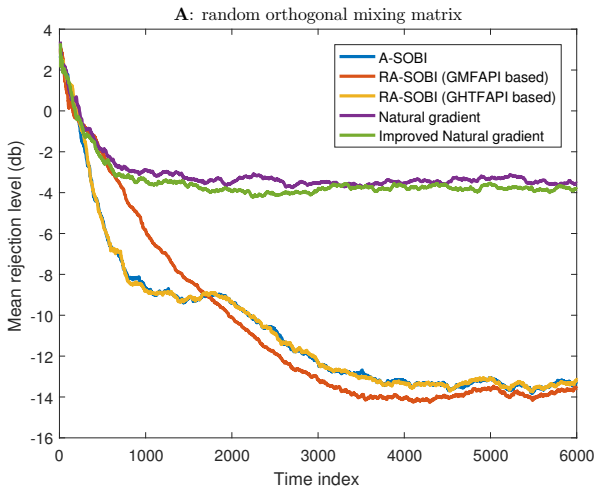

Fig. 3: Algorithms performance in case of random mixing matrix and Gaussian noise only environment

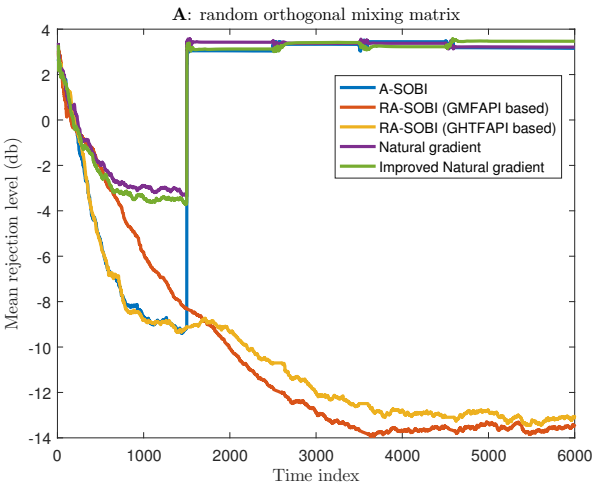

Fig. 4: Algorithms performance in case of random mixing matrix

Note that for all algorithms the forgetting factor is set to be $\beta = 0.999$ and the number of considered correlation matrices is $K = 10$. Also, the number of samples used in the threshold determination for the GHTFAPI algorithm is $L = 1000$.

To make sure our algorithm performs well in an adaptive manner, we first run the simulation without adding the burst noise. From Fig. 3, we can clearly notice that our proposed algorithm RA-SOBI in its two versions as well as the A-SOBI outperform the other state of the art algorithms when dealing with Gaussian noise environment.

In addition, to evaluate the robustness of the algorithm, we simulate a burst noise as defined in (3) that occurs during four periods of time, namely: $P_1 = [1500, 1550]$, $P_3 = [2500, 2600]$, $P_3 = [3500, 3600]$ and $P_4 = [4500, 4600]$ causing the SNR to drop to $-40dB$.

Now, we investigate three scenarios with different mixing matrices:

- First, we consider a general case with $\mathbf{A}$ being an $(n \times p)$ random matrix.
- Then, we investigate a scenario where the mixing matrix $\mathbf{A}$ is structured as:

$$\mathbf{A} = [\mathbf{a}(\omega_1); \mathbf{a}(\omega_2); \cdots; \mathbf{a}(\omega_p)] \tag{31}$$

  where:

  $\mathbf{a}(\omega_k) = [1; e^{j\omega_k}, \cdots, e^{j\omega_k(n-1)}]^T$, with $\omega_k = \pi \sin(\theta_k)$.

  θ_k is a direction of arrival chosen in our second experiment as $\theta_1 = 10°$, $\theta_2 = 30°$ and $\theta_3 = 50°$.

- Finally, we study the case where the system is slowly time varying. For that, we use the latter structure of $\mathbf{A}$ while linearly varying the directions of arrival such that it begins with $\theta_1(0) = 20°, \theta_2(0) = 10°, \theta_3(0) = -10°$ and it ends at $\theta_1(N-1) = 30°, \theta_2(N-1) = 0°, \theta_3(N-1) = -10°$ (i.e. θ_3 is kept time invariant).

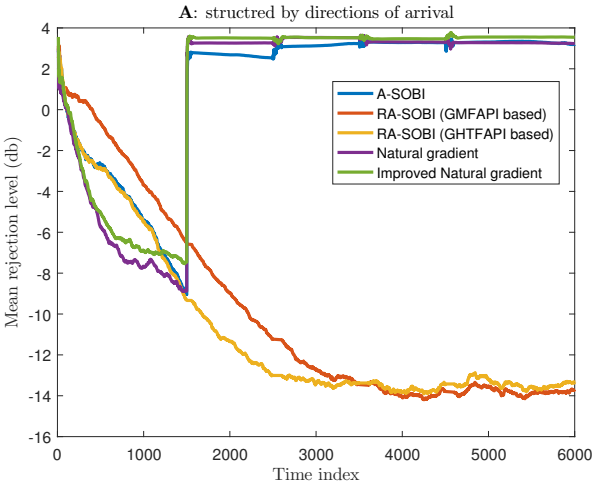

Fig. 5: Algorithms performance in case of directions of arrival dependent mixing matrix

As we can see from Fig. 4, Fig. 5, and 6, it is clear that our robust algorithm RA-SOBI (with its two versions) maintains a good source separation throughout the entire testing period, while the non-robust algorithms (A-SOBI, natural gradient and the improved natural gradient [12]) collapse at the occurrence of the first noise impulse.

VI. Conclusion

In this paper, we introduced robust adaptive algorithms for blind source separation based on second order decorrelation. The latter was achieved thanks to robust fast whitening, as well as Givens rotations based joint diagonalization performed on robust estimates of correlation matrices. Our algorithms are shown, via simulation experiments, to be effective in an impulsive noise environment, while having low computational complexity of order $O(np + pK)$ flops per iteration.

References

[1] S. haykin, "Unsupervised Adaptive Filtering: Blind source separation," John Wiley & Sons, Inc., 2000.

[2] P. Comon and C. Jutten, "Handbook of Blind Source Separa-

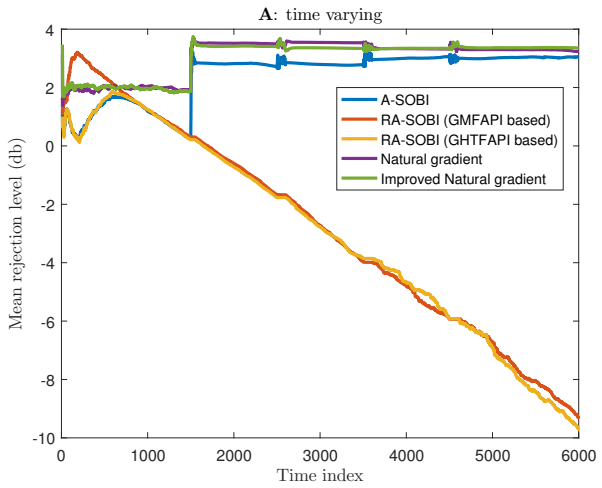

Fig. 6: Algorithms performance in case of time varying mixing matrix

tion: Independent component analysis and applications," 1st ed., Academic press, 2010.

[3] A. Belouchrani, K. Abed-Meraim, J.F. Cardoso and E. Moulines, "A blind source separation technique using second-order statistics," *IEEE Trans. Signal process.*, vol. 42, no. 2, pp. 434-444, 1997. DOI: 10.1109/78.554307

[4] J-F. Cardoso and B.H. Laheld, "Equivariant adaptive source separation," *IEEE Trans. Signal process.*, vol. 44, no. 12, pp. 3017-3030, 1996. DOI: 10.1109/78.553476

[5] L. Jiawen and L. Congxin, "A two-step adaptive blind source separation for machine sound," in *6th World Congress on Intelligent Control and Automation*, Dlaian, China, pp. 5424-5427, 2006. DOI: 10.1109/WCICA.2006.1714108

[6] C. Mühlmann (Ph.D. Dissertation), "Advances in blind source separation for spatial data," Dept, Math. Stat., Univ. Jyväskylä, Wien, Austria, 2021.

[7] Y. Pan, M. Matilainen, S. Taskinen and K. Nordhausen, "A review of second-order blind identification methods," *Wiley interdisciplinary reviews: computational statistics*, e1550, 2021. DOI: 10.1002/wics.1550

[8] A. Ziehe, P. Laskov, G. Nolte and K-R. Mãžller, "A fast algorithm for joint diagonalization with non-orthogonal transformations and its application to blind source separation," *Journal of Machine Learning Research*, vol. 5, pp. 777-800, Jul. 2004.

[9] Y. Xiang, K. Abed-Meraim and Y. Hua, "Adaptive blind source separation by second order statistics and natural gradient," in *ICASSP*, Phoenix, AZ, USA, pp. 2917-2920, 1999. DOI: 10.1109/ICASSP.1999.761373

[10] X-L. Zhu and X-D. Zhang, "Adaptive RLS algorithm for blind source separation using a natural gradient," *IEEE Signal Processing Letters*, vol. 9, no. 12, pp. 432-435, 2002. DOI: 10.1109/LSP.2002.806047

[11] X. Xie, Q. Shi and R. Wu, "A new variable step-size equivariant adaptive source separation algorithm," in *Asia-Pacific Conference on Communications*, pp. 479–482, 2007. DOI: 10.1109/APCC.2007.4433478

[12] M. Thameri, K. Abed-Meraim and A. Belouchrani, "New algorithms for adaptive BSS," in *11th ISSPA*, pp. 590–594, 2012. DOI: 10.1109/ISSPA.2012.6310620

[13] H.A. Al-Barhan, S.M. Elyass, T.R. Saeed, G.M. Hatem and H.T. Ziboon, "Blind Source Separation Based on random mixing coefficient," in *3rd IICETA*, pp. 164-168, 2020. DOI: 10.1109/IICETA50496.2020.9318954

[14] A. Belouchrani and A. Cichocki, "Robust whitening procedure in blind source separation context," *Electronics letters*, vol. 36, no. 24, pp. 2050-2051, 2000.

[15] F.J. Theis, N.S. Müller, C. Plant and C. Böhm, "Robust second-order source separation identifies experimental responses in biomedical imaging," in *International conference on latent variable analysis and signal separation*, pp. 466-473, 2010. DOI: 10.1007/978-3-642-15995-4_58

[16] J. Miettinen, M. Matilainen, K. Nordhausen, and S. Taskinen, "Extracting conditionally heteroskedastic components using independent component analysis," *Journal of time series analysis*, vol. 41, no. 2, pp. 293-311, 2020. DOI: 10.1111/jtsa.12505

[17] P. Ilmonen, K. Nordhausen, H. Oja and F. Theis, " An affine equivariant robust second-order BSS method," in *International Conference on Latent Variable Analysis and Signal Separation*, pp. 328-335, 2015. DOI: 10.1007/978-3-319-22482-4_38

[18] N. Lietzén, K. Nordhausen and P. Ilmonen, "Complex valued robust multidimensional SOBI," in *International Conference on Latent Variable Analysis and Signal Separation*, pp. 131-140, 2017. DOI: 10.1007/978-3-319-53547-0_13

[19] Z. Bekhtaoui, K. Abed-Meraim and A. Meche, "Robust adaptive algorithms for fast principal component analysis," *Digital signal processing*, vol. 127, p. 103561, 2022. DOI: 10.1016/j.dsp.2022.103561

[20] M. Thameri, K. Abed-Meraim and A. Belouchrani, "Low complexity adaptive algorithms for Principal and Minor Component Analysis," *Digital Signal Processing*, vol. 23, no. 1, pp. 19-29, 2013. DOI: 10.1016/j.dsp.2012.09.007

[21] L. Clavier, G.W. Peters, F. Septier & I. Nevat, "Impulsive noise modeling and robust receiver design," *EURASIP Journal on Wireless Communications and Networking*, vol. 2021, no. 1, pp. 1-30, 2021. DOI: 10.1186/s13638-020-01868-1

[22] A. Awad, "Denoising images corrupted with impulse, Gaussian, or a mixture of impulse and Gaussian noise," *Engineering Science and Technology, an International Journal*, vol. 22, no.3, pp. 746-753, Jun 2019. DOI: 10.1016/j.jestch.2019.01.012

[23] H. Gao, M. Chen, Y. Du and A. Jakobsson, "Monostatic MIMO radar direction finding in impulse noise," *Digital Signal Processing*, Vol. 117, p. 103198, Oct 2021. DOI: 10.1016/j.dsp.2021.103198

[24] R. Wilcox, "Introduction to Robust Estimation and Hypothesis Testing," 5th Ed. Elsevier, Sep 2021.

[25] P.C. Mahalanobis (1936), "On the generalised distance in statistics," *Proceedings of the National Institute of Sciences of India*, vol. 2, no. 1, pp. 49–55, Retrieved 2016.

[26] P.D. Domanski, "Study on statistical outlier detection and labelling," *International Journal of Automation and Computing*, vol. 17, no. 6, pp. 788-811, 2020. DOI: 10.1007/s11633-020-1243-2

[27] H. Shongwe, A.J. Han Vinck, and H.C. Ferreira, "A study on impulsive noise and its models," *J. of South African Institute of Electrical Engineers*, vol. 106, no. 3, pp. 119-131, Sep 2015. DOI: 10.23919/SAIEE.2015.8531938

Zineb Bekhtaoui was born in 1993. She received her State Engineering degree from Institut National des Télécommunications et des Techniques de l'Information et de la Communication (INTTIC), Oran, Algeria, in 2016, and the M.Sc. degree from INTTIC in the same year. She is currently a Ph.D. student at Université des Sciences et de la Technologie d'Oran, Mohamed

Boudiaf (USTOMB) affiliated to Signals and Images Laboratory (Laboratoire Signaux et Systèmes).

Karim Abed-Meraim was born in 1967. He received the State Engineering Degree from the École Polytechnique, Palaiseau, France, in 1990, the State Engineering Degree from the École Nationale Supérieure des Télécommunications (ENST), Paris, France, in 1992, the M.Sc. degree from Paris XI University, Orsay, France, in 1992, and the Ph.D. degree in the field of signal processing and communications from ENST, in 1995. From 1995 to 1998, he was a Research Staff with the Electrical Engineering Department, The University of Melbourne, where he worked on several research project related to "Blind System Identification for Wireless Communications", "Blind Source Separation," and "Array Processing for Communications." From 1998 to 2012, he has been an Assistant Professor, then an Associate Professor with the Signal and Image Processing Department, Télécom ParisTech. In September 2012, he joined the University of Orléans, France (PRISME Laboratory), as a Full Professor. Since October 2021, he is a member of the Institut Universitaire de France. His research interests include signal processing for communications, adaptive filtering and tracking, array processing, and statistical performance analysis. He is the author of about 500 scientific publications, including book chapters, international journal and conference papers, and patents. Dr. Abed-Meraim is currently a member of the IEEE SAM-TC and a Senior Area Editor of the IEEE Transactions on Signal Processing. Professor Karim Abed-Meraim is an IEEE Fellow.

Abdelkrim Meche was born in 1975. He received his B.S., M.S. and Ph.D. in 1997, 2004 and 2013, respectively, from the University of Sciences and Technology, Mohamed Boudiaf, (USTO, MB), Oran, Algeria. He is currently an associate professor at the Department of Automation, and also a member at the Signal and Image Laboratory at the Electrical Engineering Faculty of the same university. His research interests are in the fields of Statistical Signal Processing, Array Processing, Adaptive and Kalman Filtering, Image/Video Processing and Target Tracking.

Messaoud Thameri was born in 1985 (M'Sila, Algeria). He received the State Engineering Degree from Ecole Polytechnique Algiers, Algiers, Algeria, in 2009, and the Ph.D. degree in signal and images processing from Telecom ParisTech, Paris, France, in 2013. Currently, he is an assistant professor at Ecole Supérieure Ali Chabati, Algiers. His research interests include array and radar signal processing, adaptive filtering and subspace tracking, parameter estimation, and asymptotic performance analysis.

Design of a Compact UWB-MIMO Antenna with Isolation Enhancement through Extended Elliptical Ground Plane

Dalal Zahaf, Soufiane Tebache, Abderrahim Kouar, Samy Labandji, and Ali Mansoul

Abstract- This paper deals with the design of a Multiple Input Multiple Output (MIMO) antenna for UWB applications. It is composed of two identical radiating elements (parallel monopoles) symmetrically arranged on a FR-4 substrate. The monopoles are closely spaced (about 0.2λ, center to center). A decoupling mechanism based on vertical extension of the Ground plane with elliptical edges (stub) allows to achieve high isolation (>20 dB). Further, the designed system presents good diversity performance, as the obtained Envelope Correlation Coefficient is less than 0.01. The antenna array is compact (36×30 mm^2), with ultra-wide operating frequency range (2.6 to 10.8 GHz). Simulations and measurements demonstrate good agreement. The obtained results make the proposed structure a good candidate for any UWB applications and modern wireless communications systems thanks to its wide frequency band, compactness and performance.

***Keywords*- UWB, Antenna array decoupling, MIMO systems, Elliptical Ground Plane.**

NOMENCLATURE

MIMO	Multiple Input Multiple Output.
UWB	Ultra Wideband.
ECC	Envelope Correlation Coefficient .
CST	Computer Simulation Technology.

I. INTRODUCTION

With the increasing demand for connectivity to multiple wireless systems and the need to transmit data at high speed, the ultra-wideband (UWB) standard (3.1 to 10.6 GHz) was considered to be key solution as it has a very high data rate, low power consumption and low cost [1]. Despite all these advantages, the UWB standard suffers from several constraints such as short range due to fast signal fading and multipath [2], and inter-symbol interference (ISI). Multi-Input Multi-output (MIMO) technology has been introduced to combine with the UWB standard due to the advantages of achieving higher range, reducing multipath fading, eliminating interferences and providing higher channel capacity [3].

Manuscript received May 21, 2022; revised July 2, 2022.

D. Zahaf is with the Telecommunications Department, University of Science and Technology Houari Boumediene, Algiers, ALGERIA (e-mail: dallelzahaf@gmail.com).

S. Tebache is with the Electronics Department, LDCCP Laboratory, Ecole Nationale Polytechnique, Algiers, ALGERIA (e-mail: Soufiane.;tebache@g.enp.edu.dz).

A. Kouar is with the Telecommunications Department, University of Science and Technology Houari Boumediene, Algiers, ALGERIA

S. Labandji is with the Telecommunications Department, University of Science and Technology Houari Boumediene, Algiers, ALGERIA (e-mail: samy.labandji@gmail.com).

A. Mansoul is with Division Telecom, Centre de Developpement des Technologies Avancees (CDTA), Algeria (e-mail : amansoul@cdta.com).

Lot of researchers have devoted tremendous efforts to tackle the MIMO challenge, as this kind of designs is highly constrained with compact size, given the limited space in mobile devices leading to the increase of mutual coupling between adjacent radiators. Consequently, the overall antenna array performances are severely degraded [4].

To overcome mutual coupling task, several techniques have been proposed in the literature such as neutralization line (NL) [9], defected ground structure (DGS) [5], decoupling mechanism network (DMN) [10], electromagnetic band gap (EBG) [6, 7, 8], parasitic elements [11, 18] etc.

In this paper, a printed two element UWB antenna for MIMO systems is proposed. The design is compact with small size of 36× 30 mm^2 and small antenna spacing of about 0.2λ. We apply to the array a decoupling technique based on vertical extension of the ground plane that acts as a stub. The latter provides in the overall operating band an isolation higher than 20 dB. Simulation and measurement of ECC, DG and radiation pattern confirm the array diversity performance. The obtained results show the effectiveness of the proposed design and its attractive performance.

II. THE PROPOSED DESIGN

The design is composed of two identical monopoles symmetrically printed on the top layer of a FR-4 substrate (dielectric constant=4.4, thickness=1.6 mm, and tangent loss=0.02) and closely spaced (0.2λ), where λ refers to the free space wavelength evaluated at the lower frequency of the operating band (Fig. 1). Dimensions are optimized by using CST Microwave Studio and the overall size of the design is 36 × 30 × 1.6 mm^3. 50-Ohm input ports fed the antennas.Before decoupling, the antenna array is carefully studied and analyzed. Fig. 2 illustrates the simulation results of the S- parameters (S21 and S11).

Digital Object Identifier (DOI): 10.53907/enpesj.v2i1.94

It is noticed that the monopoles operate from 2.6 to 9.2 GHz (S11 <10 dB) with high mutual coupling of about 5 to 10 dB. The high coupling is due to the close proximity of the two monopoles (< 0.5λ).

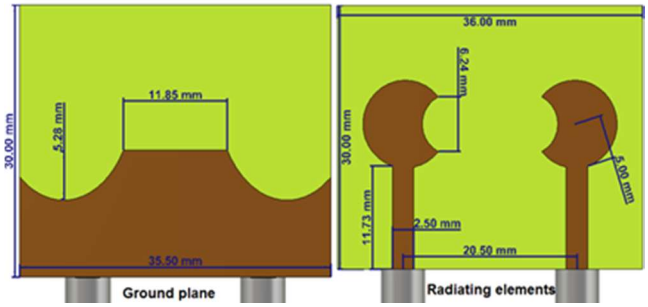

Fig. 1: Proposed antenna Geometry before decoupling.

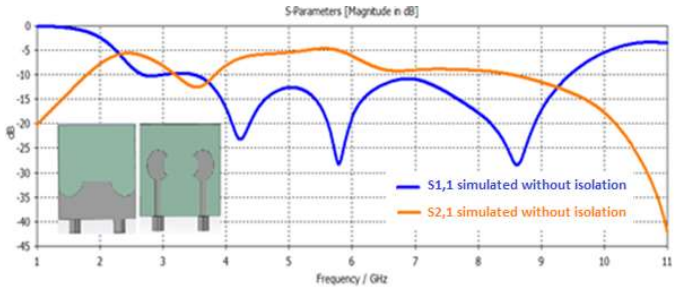

Fig. 2: S-parameters of the proposed antenna before decoupling.

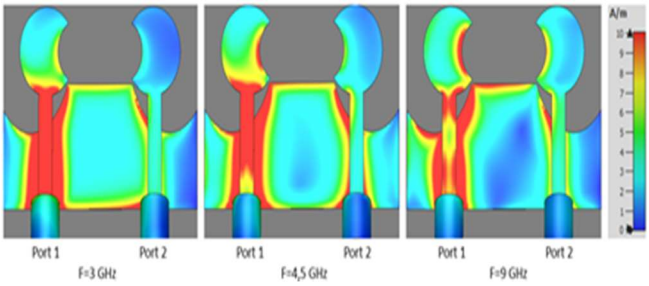

Fig. 3: Current distribution before decoupling (Port 1 excited).

Next, the Port 1 of the proposed antenna is excited and its Port 2 terminated with a 50-Ohm load. In Figure 3, the CST tool analyzes the surface current distribution of the designed antenna before decoupling at 3, 4.5 and 9 GHz. One observes high-density current flows from port 1 to port 2. The latter confirms the above S parameter results and shows the strong coupling between the two elements over the considered frequency band.

III. DECOUPLING MECHANISM OF THE PROPOSED ANTENNA ARRAY

A. Mechanism description

To solve the coupling problem, we try to find a method to trap surface currents flowing between the two ports (port 1 and port 2). Figure 4 depicts the proposed technique. A vertical extension of the ground plane with elliptical edges is added in the middle of the array ground plane. As seen in Fig. 4, the shape of the ground plane extension (stub) is optimized to operate in wide frequency range with enhancement of the antenna isolation.

B. Simulation results and discussion

The simulation results of the S parameters are illustrated in Fig. 5. After decoupling, it is noticed that the monopoles demonstrate a good impedance matching with weak mutual coupling (S21 ≤ -20 dB) in the frequency band of 2.6 to 10 GHz. In order to check the effectiveness of the proposed decoupling mechanism, current distribution is analyzed as well. As seen in Fig.6, the elliptical slots etched in the ground plane trap the current on their perimeter. As they behave like a microstrip line terminated with an open circuit, hence they prevent induced currents from flowing between excited ports.

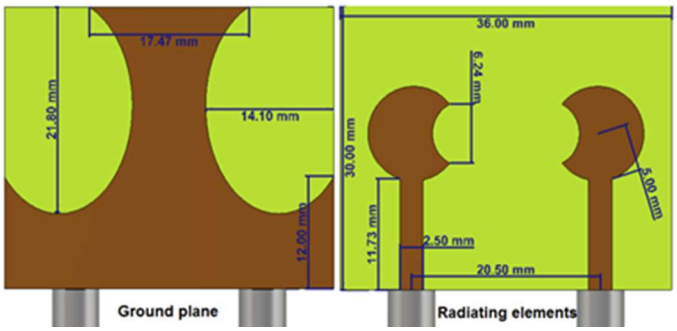

Fig. 4: Proposed antenna Geometry after decoupling.

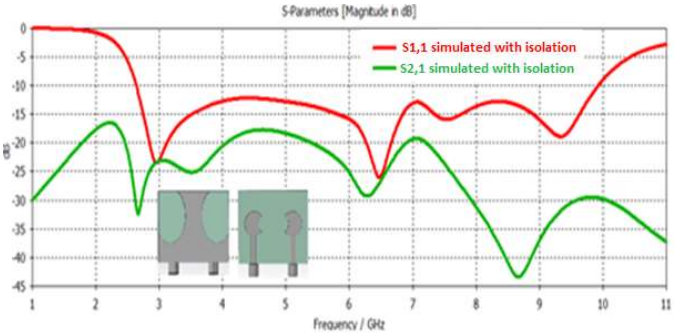

Fig. 5: S-parameters of the proposed antenna after decoupling.

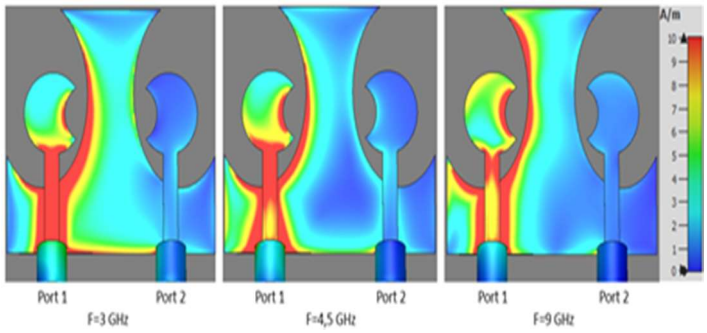

Fig. 6: Current distribution after decoupling (Port 1 excited).

The decoupled proposed antenna array is compared with respect to the coupled one through their S21 parameters in Figure 7. Hence, an improvement of about 15 dB is observed in the simulated transmission coefficient that indicates the effectiveness of the proposed decoupling mechanism.

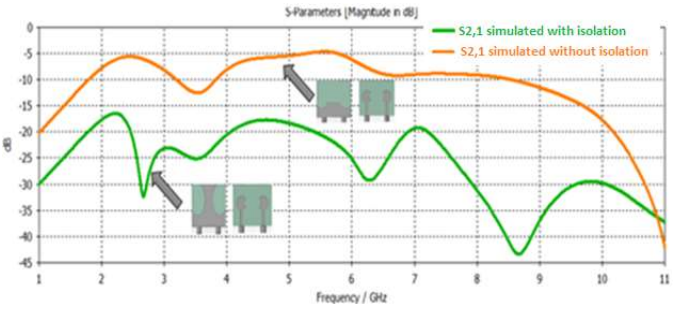

Fig. 7: Transmission coefficient (S21) with and without decoupling mechanism.

IV. MANUFACTURING AND EXPERIMENTAL DEMONSTRATION

The proposed design is manufactured and tested (Fig. 8).

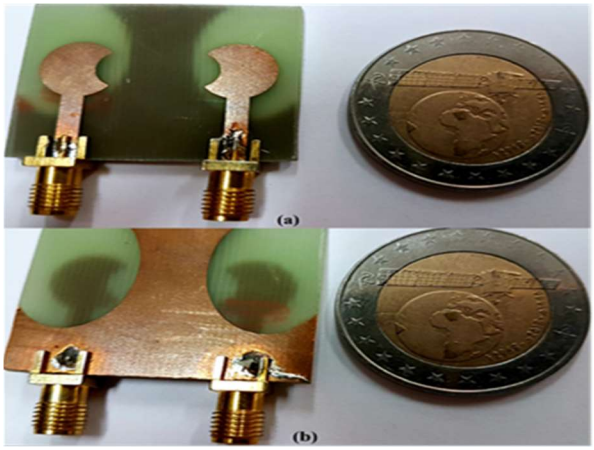

Fig. 8: Manufactured array antenna (a) Top layer (b) Bottom layer.

The simulated and measured S-parameters are shown in Figures 9 and 10. The obtaining results show an excellent match between the simulated and measured S-parameters in almost the entire UWB band as the reflection coefficients are less than -10 dB (see Fig. 9) with high isolation of more than 22 dB in the entire operating band (see Fig. 10). This agreement between simulation and measurement is obtained with slight discrepancies attributed to imprecision in the manufacturing process, instability of the substrate's relative permittivity, and SMA connectors mismatching. Figure 12 shows the radiation patterns of the proposed design evaluated both by the CST tool and by measurements in an anechoic chamber. Figure 11 shows the simulated and measured radiation patterns of the proposed decoupled antenna array at 3, 4.5 and 9 GHz in the planes H (Ø = 0°) and E (Ø = 90°). The radiation patterns are quasi-omnidirectional in the lower frequencies and more directional in higher ones which is due to the presence of the second antenna in closed proximity (behaves as a reflector). This behavior is an attractive feature as it helps in mitigating multipath effect and signal fading phenomenon.

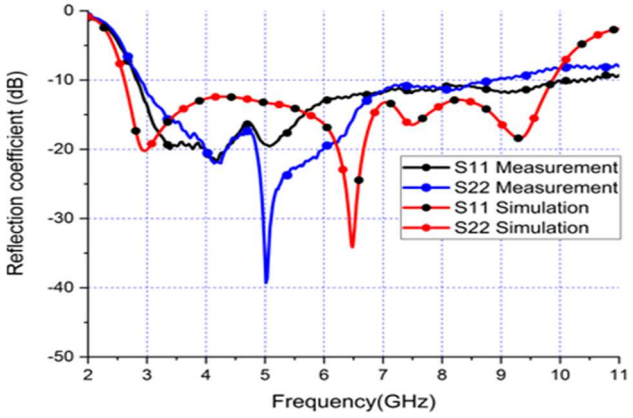

Fig. 9: Simulated and measured S11 and S22 parameters of the decoupled antenna array.

Moreover, acceptable agreement is achieved between simulation and measurement.

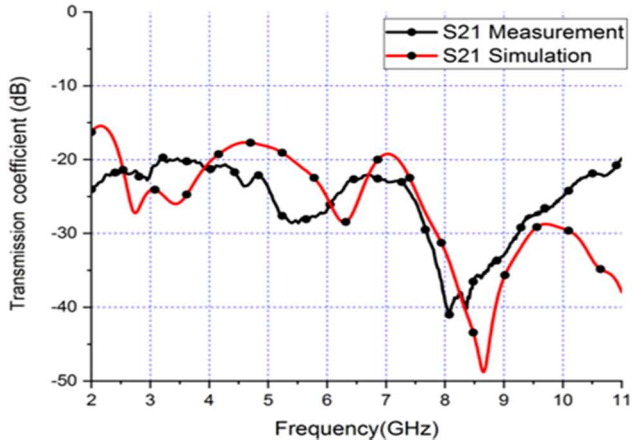

Fig. 10: Simulated and measured S21 parameter of the decoupled antenna array.

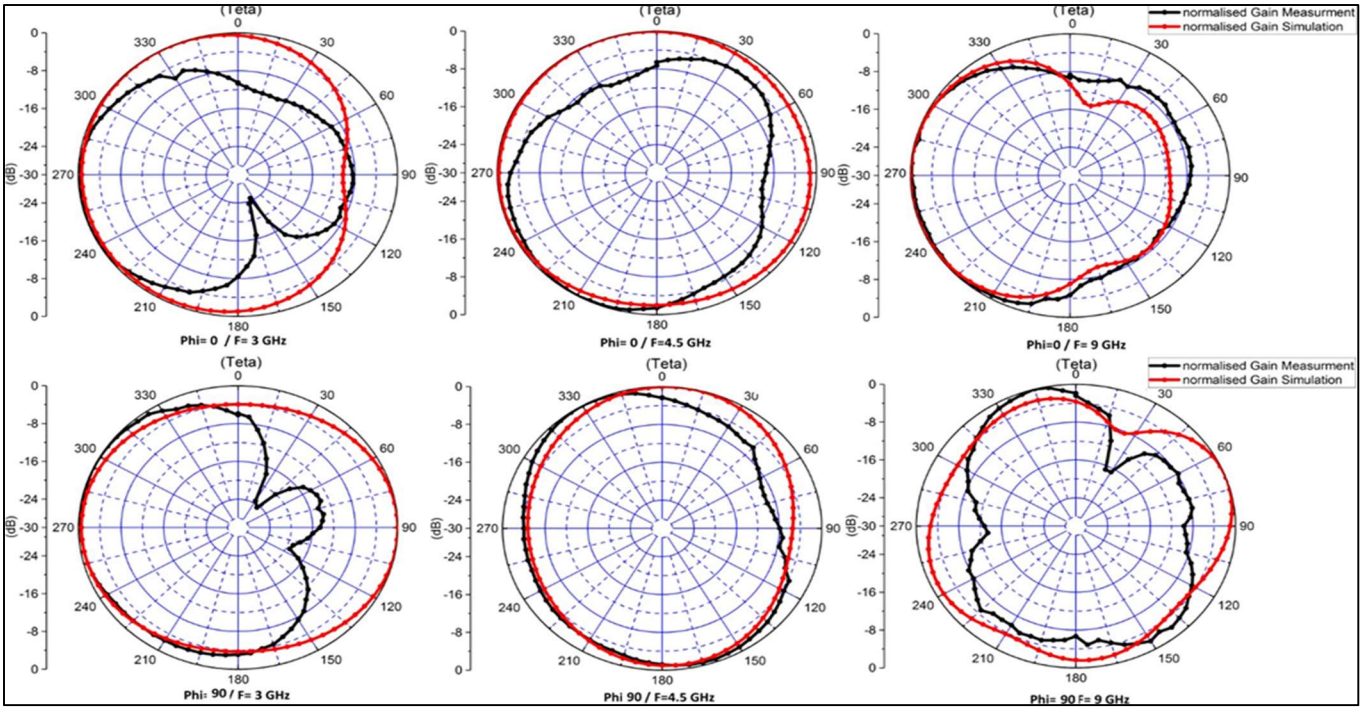

Fig. 11: Normalized simulated and measured radiation patterns in the plans E and H.

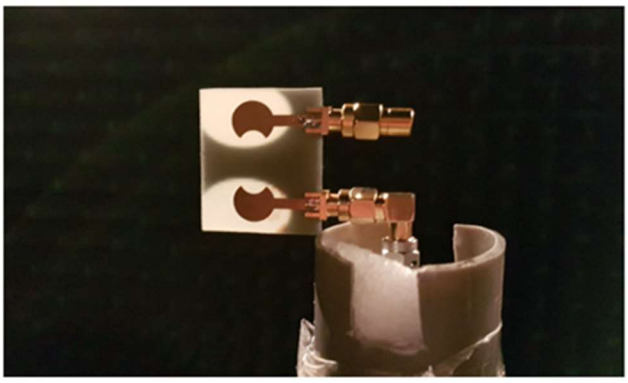

Fig. 12: Measurements in an anechoic chamber.

The Envelope Correlation Coefficient (ECC) is used as a metric for the evaluation of the diversity capabilities of the proposed MIMO antenna. The expression of this coefficient is given in equation (1) and measures the similarity between the received signals from the two Ports of the antenna array [4, 13].

$$ECC = \frac{|S_{11}^{*}\,S_{12} + S_{21}^{*}S_{22}|^2}{\left(\left(1-(|S_{11}^2| + |S_{21}^2|)\right)\left(1-(|S_{22}^2| + |S_{12}^2|)\right)\right)} \quad (1)$$

An ECC value of less than 0.5 is usually considered as acceptable in the design and evaluation of the mutual coupling between antennas [12].

The ECC results of our measured and simulated proposed antenna array are shown in Figure 13. The simulations and the measurements are in good agreement. The obtained measured ECC is close to zero (less than 0.01). This confirms the effectiveness of our achievement.

V. COMPARISON WITH RELATED WORK

A comparative study between our proposed UWB-MIMO antenna with respect to recent work is carried out and presented in Table 1. The comparison is based on various criteria such as bandwidth, mutual coupling reduction, size, design complexity and isolation technique. As a result, one can notice that the proposed design demonstrates outstanding features due to its high isolation, wide bandwidth, compact size, simplicity, low correlation and good diversity performances. Hence, the two antenna array can be good candidate for UWB portable devices.

Table. I
COMPARISION WITH RELATED WORK

Reference	Band Wide (GHz)	Size (mm)	Isolation (dB)	Spacing (λ)
[14]	2.8-10.1	55×34	≥17	0.27λ
[15]	3.1-5	35×16	≥22	0.15λ
[16]	4.4-10.7	35×46	≥17	0.19λ
[17]	4.4-9.5	36×40	≥15	0.2λ
Our work	2.6-10.8	36×30	≥22	0.2λ

VI. CONCLUSION

This paper proposed a new compact UWB-MIMO antenna. The proposed two-monopole array has attractive performance thanks to the simplicity of its structure and its high radiator isolation of about 22 dB. The decoupling mechanism considers the introduction of a vertical transition with elliptical edges in the GND plane allowing trapping currents from flowing between the antenna ports. The system can operate in very wide frequency range extending from 2.6 to 10.8 GHz. Moreover, the structure is compact as it is only 36×30×1.6 mm^3 PCB size which makes the design an attractive candidate for next wireless portable devices.

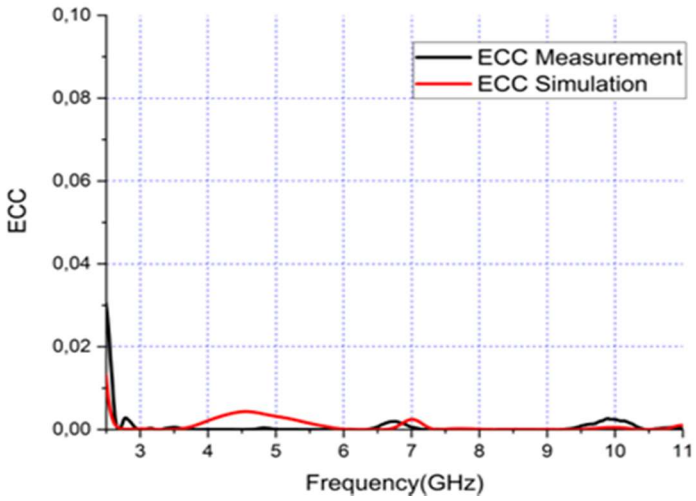

Fig 13: Envelope Correlation Coefficient (ECC) versus Frequency.

REFERENCES

[1] IBRAHIM, Ahmed A., ABDALLA, Mahmoud A., et VOLAKIS, John L. 4 elements UWB MIMO antenna for wireless applications. In: 2017 IEEE International Symposium on Antennas and Propagation, USNC/URSI National Radio Science Meeting. IEEE, 2017. p. 1651-1652. DOI: 10.1109/APUSNCURSINRSM.2017.8072868

[2] HUANG, He., LIU, Ying., et GONG, Shuxi. A novel uniplanar differentially-fed UWB polarization diversity antenna with dual notch bands. In: 2015 9th European Conference on Antennas and Propagation (EuCAP). IEEE, 2015. p. 1-4.

[3] SRIVASTAVA, Garima., KANUIJIA, K., et PAULUS, Rajeev. UWB MIMO antenna with common radiator. International Journal of Microwave and Wireless Technologies, 2017, vol. 9, no 3, p. 573-580.

[4] TEBACHE, Soufiane, BELOUCHRANI, Adel, GHANEM, Farid, et al. Novel Reliable and Practical Decoupling Mechanism for Strongly Coupled Antenna Arrays. IEEE Transactions on Antennas and Propagation, 2019, vol 67, no 9, p.5892-5899.

[5] ZAKARIA, Z., SHAIRI, N. A., SULAIMAN, R., et al. Design of reconfigurable defected ground structure (DGS) for UWB application. In: 2012 IEEE Asia-Pacific Conference on Applied Electromagnetics (APACE). IEEE, 2012. p. 195-198.

[6] EILY, A. R., ESSELLE, K. P., BIRD, T. S., et al. Experimental woodpile EBG waveguides, bends and power dividers at microwave frequencies. Electronics Letters, 2006, vol. 42, no 1, p. 32-33.

[7] GUO, Zheng., TIAN, Huiping., WANG, Xudong., et al. Bandwidth enhancement of monopole UWB antenna with new slots and EBG structures. IEEE Antennas and Wireless Propagation Letters, 2013, vol. 12, p. 1550-1553. DOI: 10.1109/LAWP.2013.2292063

[8] M. Y. Koledintseva, S. Radu and J. Nuebel, Design and Sensitivity Analysis of EBG Stripline Common-Mode Filters, in IEEE Transactions on Electromagnetic Compatibility. DOI: 10.1109/TEMC.2018.2889441.

[9] YU, Yantao., LIU, Xiaoya., GU, Zhaokai., et al. A compact printed monopole array with neutralization line for UWB applications. In : 2016 IEEE International Symposium on Antennas and Propagation (APSURSI). IEEE, 2016. p. 1779-1780.

[10] CHEN, Shin-Chang., WANG, Yu-Shin., et CHUNG, Shyh-Jong. A decoupling technique for increasing the port isolation between two strongly coupled antennas. IEEE Transactions on Antennas and Propagation, 2008, vol. 56, no 12, p. 3650-3658.

[11] RADHI, Alaa H., NILAVALAN, R., WANG, Yi, AL-RAWESHIDY, H.S., ELTOKHY, Amira A. and AB AZIZ, Nur, Mutual coupling reduction with a wideband planar decoupling structure for UWBMIMO antennas. International Journal of Microwave and Wireless Technologies.2018. Vol. 10, no. 10p. 11431154.

[12] HENG, Yong., LU, Wen-jun., CHENG, Chong-hu., et al. Printed diversity antenna with cross shape stub for ultra-wideband applications. In: 2008 11th IEEE Singapore International Conference on Communication Systems. IEEE, 2008. p. 813-816.

[13] BLANCH, S., ROMEU, J., et CORBELLA, I. Exact representation of antenna system diversity performance from input parameter description. Electronics letters, 2003, vol. 39, no 9, p. 705-707.

[14] P. Bambarkar and S. Kulkarni, Design of ultra-wideband (UWB) MIMO antenna, 2017 International Conference on Intelligent Computing and Control (I2C2), Coimbatore, 2017, pp. 1-4.

[15] Yong Cheng., Wen-jun Lu., Chong-hu Cheng., Wei Cao., and Yong Li, Printed diversity antenna with cross shape stub for ultra-wideband applications, 11th IEEE Singapore International Conference on Communication Systems, Guangzhou, 2008, pp. 813-816.
[16] K. M. Prasanna and S. K. Behera, Compact two-port UWB MIMO antenna system with high isolation using a fork-shaped structure, International Conference on Communication and Signal Processing, Melmaruvathur, 2013, pp. 726-729. DOI: 10.1109/iccsp.2013.6577151
[17] Manuel Prasanna.K and S.K. Behera, A Hexagonal MIMO Antenna System With Defected Ground Structure to Enhance Bandwidth and Isolation, IEEE International Conference on Communication and Signal Processing (ICCSP), Melmaruvathur, India, April 2013, pp. 3-5.
[18] Abderrahim Kouar, Soufiane Tebache, Dalal Zahaf, Samy Labandji. UWB Decoupling Approach for Two Extremely Close Monopole Antennas, 2019 6th International Conference on Image and Signal Processing and their Applications (ISPA), 2019.

Dalal Zahaf received the Master's degree in the Telecommunications in 2019 from University of Science and Technology Houari Boumediene, Algiers, ALGERIA.

Soufiane Tebache received the Engineering degree from Polytechnic School, Algeria, in 2009, with honors (first class), and the Magister degree in Signals & Communications from Biskra University, in 2013 with honors as well (first class). In 2021, he defended his PhD thesis in telecommunications at Ecole Nationale Polytechnique (ENP), Algeria. His current research interests include: Antenna & RF system- design, Microwaves, Electromagnetic field theory and Propagation, MIMO systems, Wireless communications, IoT and 5G.

Abderrahim Kouar received the Master's degree in the Telecommunications in 2019 from University of Science and Technology Houari Boumediene, Algiers, ALGERIA.

Samy Labandji is an assistant professor at the Telecommunications Department of University of Science and Technology Houari Boumediene, Algiers, ALGERIA.

Ali Mansoul received the Engineering degree from the University of Jijel, Jijel, Algeria, in 2006, the M.Sc degree in telecommunications from the Ecole militaire polytechnique, Bordj El Bahri, Algeria, in 2010, and the Ph.D. degree from the Ecole National Polytechnique, Algiers, Algeria, in 2016. He is currently the Head of the Antenna Team with the Centre de Development des Technologies Avancées. His current research interests include antenna design, reconfigurable antennas, multiple-input multiple-output systems, and wireless communications.

Phosphate Amendments for the Inhibition of Acid Mine Drainage Generated from Sidi Kamber Tailings Facility

Amira Merchichi, Malek Ould Hamou, Mostafa Benzaazoua, Farid Aghilasse Mansour, Nabil Babahoum, and Hakim Rabia

Abstract− The aim of this paper was to evaluate the efficiency of phosphates product and by-products from the Djebel Onk mine for the control of acidic mine drainage generated by exposure of Sidi Kamber mine tailings to climatic conditions. Kinetic tests in humidity cells were carried out according to the modified ASTM standard, was used to investigate the geochemical behaviour of the Sidi Kamber tailings mixed with phosphate materials (phosphatic limestone wastes, raw low grade phosphate ore and phosphate mine tailings) after being charcaterized. All amendment compositions led to an increase of the pH of the leachate from approximately 3 to circum-neutral values. Humidity cells experiments indicated that the materials were adequate to immobilize Pb, Zn, Cu and Fe by about 99% and prevent their release from the tailings. The tests have also shown that the metals concentrations within the leachate are lower than the limits allowed by Algerian legislation for industrial liquid effluents. Among the tested material amendments, PLW was more effective than other products in immobilizing metals. The result are most probably related to their Ca-carbonate content and/or adsorption capacity.

***Keywords*− Sidi Kamber mine, Acid Mine Drainage (AMD), Phosphate material, Mining tailings, humidity cell leaching test, Neutralization.**

NOMENCLATURE

SK	Sidi Kamber.
SKF	Flotation Sidi Kamber tailings.
SKG	Gravimetry Sidi Kamber tailings.
PLW	Phosphatic Limestone Wastes.
RLGP	Raw Low Grade Phosphate ore.
PMT	Phosphate Mine Tailings.
AMD	Acid Mine Drainage.

I. INTRODUCTION

The mining industry is one of the most important and fundamental industries for the Algerian economy. It generates substantial inflows of foreign currency and contributes to the national development. However, it generates large amounts of liquid and solid wastes, which affect the environment, in particular water, soil, landscape, fauna and flora.

The oxidation of sulphide minerals within solid mine wastes can occur under natural conditions, according to the succession of climatic seasons. During acid-neutralization reaction, acidic aqueous effluent enriched with high metal concentrations and sulphates can be generated [1] [2] [3] [4]. In the presence of oxygen and water, the sulphide can be oxidized according to the following reaction (Eq.(1)):

$$FeS_2 + 7/2O_2 + H_2O \rightarrow Fe^{2+} + 2SO_4^{2-} + 2H^+ \quad (1)$$

This reaction depends on the oxygen concentration, the water saturation index of the porous media and the temperature. Also, the sulphide oxidation can be induced by aqueous ferric iron (Eq.(2, 3)).

$$FeS_2 + 14Fe^{3+} + 8H_2O \rightarrow 15Fe^{2+} + 2SO_4^{2-} + 16H^+ \quad (2)$$

$$Fe^{2+} + 1/4O_2 + H^+ \rightarrow Fe^{3+} + 1/2H_2O \quad (3)$$

The presence of some bacteria, such as *Thiobacillus*, are known to be strong catalyzers at acidic pHs of oxidation reactions, which consequently increase their kinetics [5]. These bacteria oxidize the surface of the mineral and favour the production of sulphates and the conversion of Fe^{2+} ions into Fe^{3+} ions [6].

Moreover, the ferric iron hydrolysis can increase the acidity of the effluent and metal leaching. Any change of physicochemical conditions (during climate seasons) can lead to dissolution, and precipitation/co-precipitation, which can affect the overall drainage water quality.

The secondary minerals formed can again release metals into the natural environment at varying concentrations [7] [8]. In order to reduce the effect of contaminants on the environment, the contaminated effluent must be treated [6] [9].

Manuscript received November 3, 2021; revised July 22, 2022.

This work was financially supported by the Research Laboratory on Mining Engineering of Ecole Nationale Polytechnique.

A. Merchichi, M. Ould Hamou, F.A. Mansour and H. Rabia are with the Mining Engineering Department, Laboratoire de Recherche de Génie Minier, Ecole Nationale Polytechnique, Algiers, ALGERIA. (e-mail: amira.merchichi@g.enp.edu.dz, malek.ould_hamou@g.enp.edu.dz, farid_aghilasse.mansour@g.enp.edu.dz, hakim.rabia@g.enp.edu.dz).

N. Babahoum is with SONATRACH, Algiers, Algeria (e-mail: nabil.babahoum@g.enp.edu.dz)

M. Benzaazoua is with the University of Quebec at Abitibi-Temiscamingue (UQAT), Research Institute on Mines and Environment (RIME), 445 boul de l'Universite, Rouyn-Noranda J9X 5E4, QC, Canada / Mining Environment and Circular Economy, Mohammed VI Polytechnic University, Lot 660, Hay Moulay Rachid, Ben Guerir 43150, Morocco. (e-mail: Mostafa.Benzaazoua@uqat.ca).

Digital Object Identifier (DOI): 10.53907/enpesj.v2i1.67

The design of contaminant effluent treatment plant and the choice of treatment method are based on several parameters such as the chemical characteristics of AMD, climatic conditions, type of residues, hydraulic retention time, etc. [10]. Acid production can be reduced to very low levels by eliminating one of the three components of sulphide oxidation reaction (i.e., mining waste, water, oxygen; [9] [11]). Recent improvements in AMD waters treatment techniques have allowed lowering the level of contamination to acceptable environmental limits regarding many elements [12] [13].

Recently, several AMD treatment techniques have been developed to neutralize the acidity of AMD and reduce hazardous and toxic effluents. AMD treatment methods are divided into two main categories: a) Active methods: which involve the continuous addition of an alkaline compound to AMD to neutralize acidic effluents produced at mine sites and to precipitate metal contaminants [14] [15] [16] [17]; b) Passive methods: which use economical and environmentally friendly processes to achieve the same effects with a long-term, effective treatment, and offer the possibility of re-using materials at low cost [18] [19].

The alkaline amendment is one of the AMD control methods that involves mixing the tailings with alkaline materials to limit the oxidation of sulphides and neutralize the acidity generated [20] [21]. The purpose of this study is to evaluate the effectiveness of an amendment consisting of phosphatic materials (phosphatic limestone wastes, Raw low grade phosphate ore and phosphate mine tailings) for the control of the DMA phenomenon. The effectiveness of these materials for the remediation of contaminated water and soil has been widely studied [22] [23] [24] [25]. The main originality of this research compared to previous studies on AMD treatment using phosphate amendments relies on the nature of the tailings (high concentration of heavy metals) and the variety of P products and by-products that have been used. Indeed, the used materials, i.e.,These later include phosphatic limestone waste, raw low-grade phosphate ore and phosphate mine tailings that are locally available at low cost and efficient for AMD control and treatment.

II. Material and Methods

A. Sidi Kamber mine site description and sampling

The abandoned Sidi-Kamber mine is located south of the Collo massif and about 36 km west of the town of Skikda **(Fig. 1)**. This mining site fall within the Oued Es-Essouk sub-watershed (12.49 km^2), which supplies the Guenitra dam [26] [27]. Sidi Kamber region is characterized by a Mediterranean climate (wet and cool winter and a dry and arid summer) with average annual precipitation of around 742.35mm, average annual temperatures of 19 °C and average monthly humidity of around 68, 8% [28]. The mined ore deposit consisted of eight quartz veins mainly hosted in gneiss and granulite formations belonging to the metamorphic Precambrian Kabyli bedrock [30] [37] .The mineralization is composed of sulphide minerals (pyrite, pyrrhotite, marcasite, sphalerite and galena) and gangue minerals such as magnetite, hematite, barite and aluminosilicates [27] [30] [38]. The Sidi Kamber fine and coarse tailings stockpiled in dyke/piles are highly acid generating, with NNPs varying from -31.13 and -152.38 kg/$CaCO_3$/t [30]. This mine is a major source of contamination of surface water and groundwater [27] [29] [30] [31]. Oxidized minerals dissolved over several years generate acidic effluents that disturb the environment. Chemical analyses of weathering products in mine wastes (tailings and waste rock) and soil contaminated by AMD, showed serious contaminations with some metals (Zn, Fe, Pb, Mn, Hg, and Cd) [27].

Sidi Kamber samples were collected using an auger and were then air-dried for 2 weeks. These tailings were crushed and sieved through a 1mm.The sieved samples were stored for analysis.

B. Phosphate amendments

The phosphate deposits are concentrated in the Djebel Onk mining district situated in the northeastern part of Algeria (Tebessa department). The studied sedimentary succession is about 500 m thickness and aged of Upper Cretaceous (Maastrichtian) to Middle Eocene (Lutetian). The Thanetian phosphate layer is about 30 to 35 m thick [39] [40] [41]. Three types of materials from the Djebel Onk phosphate deposits, raw low-grade phosphate ore (RLGP), phosphatic limestone wastes (PLW), and phosphate mine tailings (PMT) were used to amend the Sidi Kamber tailings. The samples were dried, crushed, sieved and stored in plastic bags before testing.

C. Physical, chemical and mineralogical characterization

The samples were sieved using a series of sieves with standardized openings (ISO R-20 series sieves) and by a laser analyser (Malvern Mastersizer S) to measure the particle size distribution of particles from 0.06 to 80 µm.

For solid samples, metals concentrations were analyzed by fluorescence using Niton XL3t 900SHE instrument. This device can measure concentrations ranging from ppm to high levels but less accurate than ICP-AES spectroscopy.

The mineralogy of the samples was determined using an optical microscope and a Bruker AXS Advance D8 diffractometer (in θ / 2θ mode for diffraction angles between 5 ° to 70 °). Eva and TOPAS software are used for the identification and quantification of mineral phases.

D. Kinetic tests in weathering cells (method developed by Cruz et al., 2001, modified by Villeneuve, 2004)

The geochemical behavior of samples was evaluated in weathering cell (WC) kinetic test [43]. The WC simulates an accelerated and natural oxidation of mine discharges [44]. These tests have been recommended due to the small quantity of sample, the rapidity and stability of the geochemical behaviour during the leaching cycles of wetting/drying [45]. [46]. Two WCs were set up, for SKG and SKF tailings. Approximately 67 g of tailings were placed in a 10 cm diameter Buchner funnel, equipped with a 0.45 µm filter **(Fig.2).**
A 250 mL vacuum flask was installed under every Büchner to collect the filtrate after flushing. Twice a week, the samples were allowed to contact 50 ml deionized water for 3h.
Between two flushes, WCs were exposed to ambient air. Leachates from each WC were analyzed for pH, Eh, electrical conductivity and metal (Fe, Ca, Mn, Ni and Zn) [42] [43] [47].

E. Alkaline amendment tests

Alkaline amendment is the technique which prevent and control the formation of acid mine drainage [32]. It consists of an alkaline addition (limestone, dolomite, phosphate) directly in contact with the tailings, in order to limit the oxidation of sulfides and maintain the pH of the pore water in the tailings close to neutrality [20] [33].

Three alkaline materials (carbonate phosphate waste rock, crude phosphates and tailings) were used to control the formation of DMA and improve water quality. To this end, kinetic tests in humidity cells were carried out according to the modified ASTM standard (American Society for Testing and Materials D5744-07). The experimental cells (10.2 cm high and 20.3 cm in diameter), five in number, contained about 1 kg of mine tailings SK (SKG + SKF), mixed with phosphate materials. Leaching involves circulating approximately 500 ml of deionized water through the cell once a week for six months **(Table.1).**

Table. I Different configurations chosen for the alkaline amendment tests

Tests	Composition	
C1	2/3 SK + 1/3 PLW	SKG: Gravimetry tailings SKF: Flotation tailings SK: Sidi Kamber tailings (SKG+ SKF) PLW: Phosphatic limestone wastes RLGP: Raw phosphate PMT : Phosphatic tailings
C2	2/3 SK + 1/3 RLGP	
C3	2/3 SK + 1/3 PMT	
C4	2/3 SK + 1/3 (PLW+ PMT)	
C5	2/3 SK + 1/3 (PLW + RLGP)	

The cycle begins with a rinse with deionized water which remains in contact with the sample for a period of 4 hours, followed by 3 days of dry air circulation and 3 days of humidified air circulation between 90% and 100%. The airflow is maintained at 1 to 10 l/min **(Fig. 3)**

F. Analysis of leachate quality

A Starter ST310 electrode was used for the pH measurements, coupled with a Jeneway 3510 pH meter (precision ± pH 0.01). Buffer solutions (pH4, pH 7 and pH10) were used for the calibration of the pH meter.
The redox potential is measured using an electrode and an Eutech Instruments Ion2700 device. The obtained values were corrected to the standard hydrogen electrode (SHE; 200 mV).
The Conductivity was measured using an OHAUS ST 20 C-A conductivity meter. The device was calibrated with a standard solution (200 µS/cm).
The concentrations of chemical elements were measured by atomic absorption spectrometry of the Contraa 800 (Analytik Jena) type.
The samples were first filtered at 0.45 µm, then acidified with 2% nitric acid (HNO_3) and refrigerated until analysis.

III. Results and discussion

A. Physical, chemical and mineralogical characterization

Sidi Kamber tailings

The results of the sieve analysis were presented in **Table.II**. The calculated values of the coefficients of uniformity and curvature (Table 11), were estimated at 2.5 ($2 \leq Cu \leq 5$) and 0.98 ($Cc < 1$) for the flotation tailings, the material is poorly graduated with a tight particle size. More than 80% of the particles had a diameter between 63µm and 160µm. The gravimetric separation tailings curve is continuous; the material is well graded ($1 < Cc < 3$) and the particle size was semi-spread ($5 < Cu \leq 20$).
The mineralogical composition of Sidi Kamber tailings determined by XRD was summarized in **Table.II**.

The samples SKF and SKG were generally composed of the same mineralogical phases but with different proportions: quartz (20 – 61.9%), muscovite (32.4 – 8.2%), barite (4.7 – 5.4%), pyrite (3.05 – 4.3%), and galena (1.34 – 0.96%). The secondary minerals identified in the SKF sample include jarosite (14.2%) and gypsum (2.2%). Barium hydroxides (12.2%) and gypsum (7%) were also present in SKG tailings.

Chemical compositions of Sidi Kamber samples were presented in **Table II**. The analyses showed similar concentrations of SiO_2 (21.65-23.54%), MgO (0.63-0.79), Al_2O_3 (7.22-7.98%), K_2O (2.38-3.45%), CaO (0.67-0.876%) and a higher variation in Fe_2O_3 (3.12-6.96%) (Table 2). Total sulphur had very high levels ranging from 3.18% to 5.36%, this is explained by the presence of sulphide minerals.
Significant concentrations of Zn (1052-1423 mg/kg) and lead (847-954) were measured, corresponding to the sphalerite and galena minerals that are abundant in SKF and SKG tailings.

Phosphate amendments

Phosphate materials (PLW, RLGP and PMT) showed more than 50% of the elements by weight > 80 µm, so there is the presence of gravel, sand and silt while tailings are mostly fine.
The mineralogical characterization of the raw phosphates was determined by X-ray diffraction spectrometry, which mainly identified gangue minerals. Phosphatic waste rock was mainly composed of carbonate minerals (dolomite and calcite), quartz, and ilmenite, whereas the minerals present in the raw phosphates include dolomite, calcite and fluorapatite **(Table. II).** The tailings had similar mineralogical compositions as raw phosphates [31].

The chemical composition of phosphatic limestone wastes is characterised by very high (32.5% CaO and 2.2% MgO) contents. Phosphate ore (RLGP) and phosphate mine tailings (PMT) had high levels of CaO (45.2%), P_2O_5 (28.8%) and SiO_2 (4.0%). Cobalt, Zinc, Barium and lead are also present at low concentrations [31].

B. Kinetic tests in mini weathering cells

Kinetic tests in weathering cells were carried out over a period of 175 days to assess the environmental risks of metal contamination (Fe, Cd, Zn and Pb). **Figure 4** shows the evolution of pH, Eh, conductivity and metal concentrations in the leachates obtained from SKF, and SKG samples. The geochemical behaviour of the two samples is similar.
During the first cycles of the experiments, the pH of the leachates was about 3.43 and 3.02 for the SKF and SKG tailings respectively. Then, the pH increased to stabilize at 4.25 after 20 weeks for SKG sample. At the end of the test, the pH decreased to strongly acidic values (pH less than 3.9) for SKF. These values indicate strong bacterial activity that oxidises iron (*Acidithiobacillus Ferrooxidans*, *Leptospirillium Ferrooxidans*) [48] [49]. It should be noted that a pH below 6.5 does not meet the Algerian environmental criterion for the final discharge of industrial liquid effluents.
The redox potential values ranged from 450 mV to 490 mV for SKF and from 420 mV to 540.3 mV for SKG, indicating that the environment is oxidizing. The conductivity showed a decreasing trend for the two samples (1365 µS/cm to 260 µS/cm for SKF and 1100 to 255 µS/cm for the SKG).

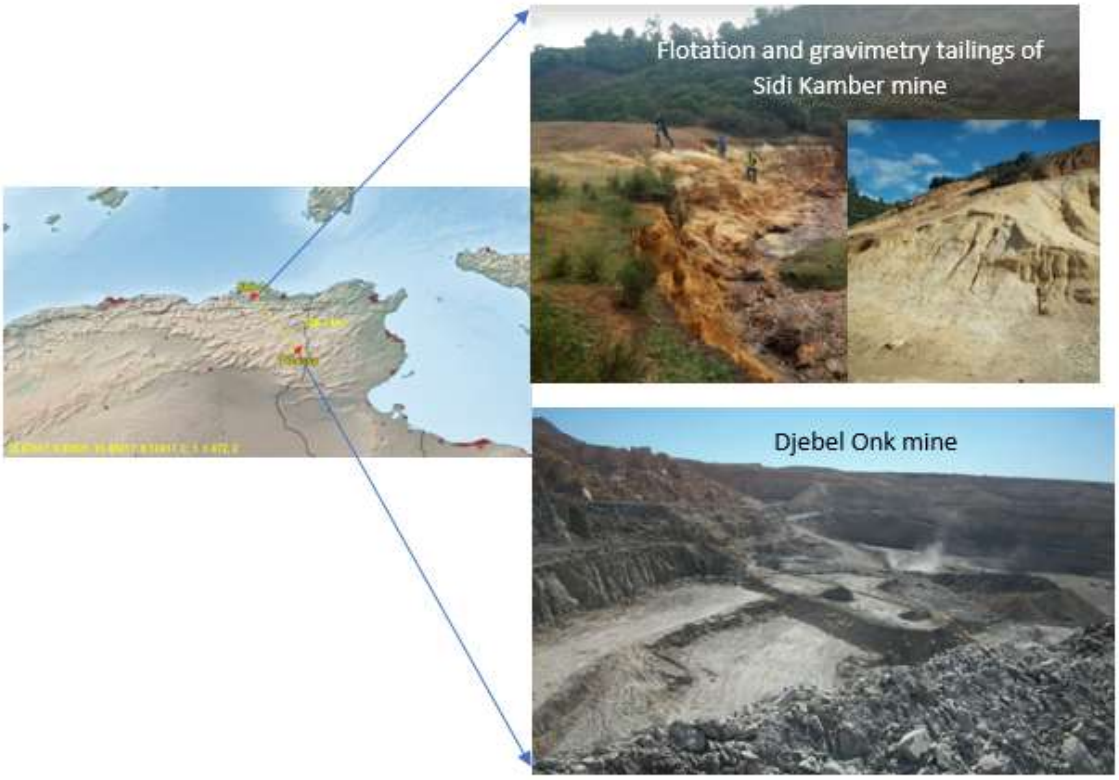

Fig. 1: Geographical sites location of the Djebel Onk phosphate mine and Sidi-Kamber polymetallic mine

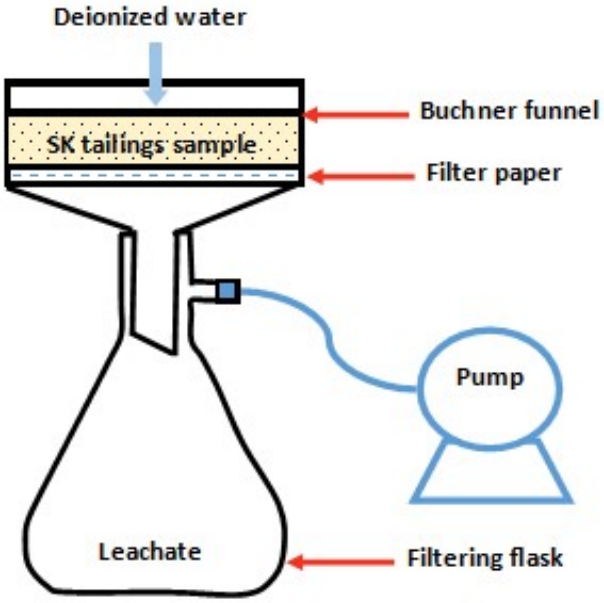

Fig.2 Schematic diagram of the weathering cell test

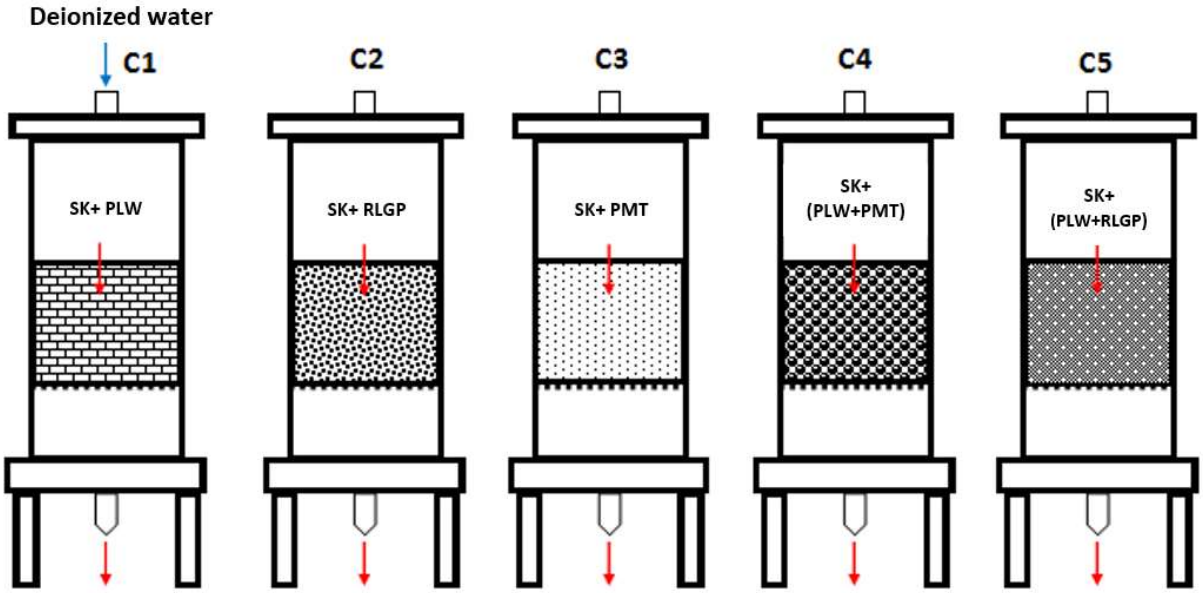

Fig. 3: Schematic presentation of the hymidity cells testing procedure (phosphate amendments)

In fact, Mayer [50] explained this decrease in Eh values by a pre-oxidation of the sulphide grains which can lead to a change in their reactivity.

F**igure 4** shows high initial concentrations that may be related to the dissolution of ultrafine particles [51] [52] [53] and to the dissolution of highly reactive mineral surfaces [51]. Weakly adsorbed elements were then quickly released into solution.

Lead concentrations in leachates ranged from 0.48 to 0.78 mg/L for SKF and from 0.39 to 1.1 mg/L for SKG. The assembly of minerals (galena PbS, anglesite $PbSO_4$ and cerussite $PbCO_3$) is the most cause of the release of lead. The measured Zn concentrations showed high values during the first over cycles (SKF, 6.5 mg/L), (SKG, 2.8 mg/L). This result can be explained by the oxidation and high reactivity of the ZnS sphalerite. At the end of the tests, Zn concentrations were about 0.38 mg/L for SKF and SKG. Cadmium concentrations in the leachates decreased from 0.7 to 0.43 mg/L for both Sidi Kamber samples. **Figure 4** showed that low Fe concentrations were leached from residues (0.36 mg/L for SKF and 0.32 mg/L for SKG). The iron had probably precipitated into the cells.

The initial leachates had low pH (from 3.02 to 4.9) and high metal concentrations such as Cd (from 0.7 to 0.8 mg/L), Zn (from 3 to 7 mg/L) and Pb (from 0.6 to 1.2 mg/L). The measured concentrations do not meet the Algerian environmental standards: 1.5 mg/L for Cu, 5 mg/L for Fe, 3 mg/L for Zn, and 0.2 mg/L for Pb and Cd (Executive Decree No. 06–141). It should be noted that in terms of AMD prediction, weathering cell tests do not realistically reflect natural conditions compared to humidity cells or real field, since AMD takes a long period of time to achieve equilibrium and it depends on several specific factors (grain size distribution, mineralogical and chemical compositions, and climatology) [1] [54]

C. Alkaline amendment

Figure 5 showed the water quality of the leachates (variations in pH, conductivity, redox potential and metal concentrations) at different time during the humidity cell tests for the 5 phosphate amendments tested.

The pH value in the first leaching cycle for the five humidity cells exceeded 7.5. In cells C1 (SK+PLW); C3 (SK+PMT) and C4 (SK+PLW+PMT), the pH increased considerably to reach maximum values of 8.25, 8.27 and 7.91 respectively for cell C1, C4, and C3. Cells C2 and C5 contained respectively (SK+RLGP) and (SK+PLW+RLGP) had a neutral pH (7.25 to 7.56) at the last leaching cycle (**Fig. 5a**).

This increase in pH is due to the contact between the tailings and each of the materials tested and was a result of the high buffering effect of the amendments consisting mainly of carbonate and apatite minerals.

Redox potential values during the humidity cells tests are shown in **Fig. 5b**. As with the pH variation, the graphs showing the variation of the redox potential as a function of time had the same allure. The Redox potential of leachates containing each of the materials decreased significantly, reaching similar values of 329 mV and 326 mV respectively for C3 and C4 cells and lower values of 317 mV for C1 cell contained PLW. For leachate from cells C2 and C3, the redox potential varied from 360 to 395 mV throughout the test period.

The results indicated a chemical reaction between SK tailings and phosphate alkaline materials, explained by an acid neutralization.

The conductivity values measured in the cells are shown in **Fig. 5c.** The conductivity is proportional to the concentration of ions in solution. Ions resulting from carbonate dissolution and SO_4^{2-} ions contribute to conductivity variations. Conductivity decreased during leaching cycles in 5 cells from 6500 to 3300 µS/cm.

In order to assess the effectiveness of phosphate treatment, metal concentrations were measured and used as a criterion for performance [34] [35]. The evolution of metal concentrations in solution during the amendment tests is shown in **Figure 5.**

The variation in the concentrations of iron in leachate showed that it was easily eliminated by the phosphate materials with final concentrations of 0.005 mg/L for cell C1, 0.012 mg/L for C2, 0.009 mg/L for C3, 0.0085 mg/L for C4 and 0.01 mg/L for C5 (**Fig. 5d**).

Table. II Physical, chemical and mineralogical characterization of Sidi Kamber mine tailing

Sidi Kamber mine tailings			
Physical characteristics			
Symbol	Unit	SKF	SKG
D_{10}	µm	160	160
D_{30}	µm	250	630
D_{60}	µm	400	2000
$Cu = D_{60}/D_{10}$	-	2.5	12.5
$Cc = D_{30}^2/(D_{60}*D_{10})$	-	0.98	1.24
W	%	1.71	2.07
pH		3.72	2.87
Chemical characteristics			
Mg	%	0.63	0.79
Al	%	7.98	7.22
Si	%	23.54	21.65
K	%	3.45	2.38
Ca	%	0.67	0.87
Fe	%	3.12	6.96
Mn	%	0.03	0.01
S_{tot}	%	3.18	5.36
Cu	mg/kg	120	116
Zn	mg/kg	1052	1423
Pb	mg/kg	847	954
Mineralogical characteristics			
Baryte	%	4.7	5.4
Barium hydroxide	%	-	12.2
Quartz	%	20.1	61.9
Muscovite	%	32.4	8.2
Nacrite	%	22,01	-
Pyrite	%	3.05	4.3
Galène	%	1.34	0.96
Gypse	%	2.2	7
Jarosite	%	14.2	-

Phosphate amendments				
Mineralogical characteristics				
Minerals	Unit	PLW	RLGP	PMT
Dolomite	%	95.96	55.69	59.24
Calcite	%	0.22	18.48	20.52
Quartz	%	2.45	-	-
Fluorapatite	%	-	25.83	19.76
Ilmenite	%	1.37	-	-
Kaolinite	%	-	-	0.48

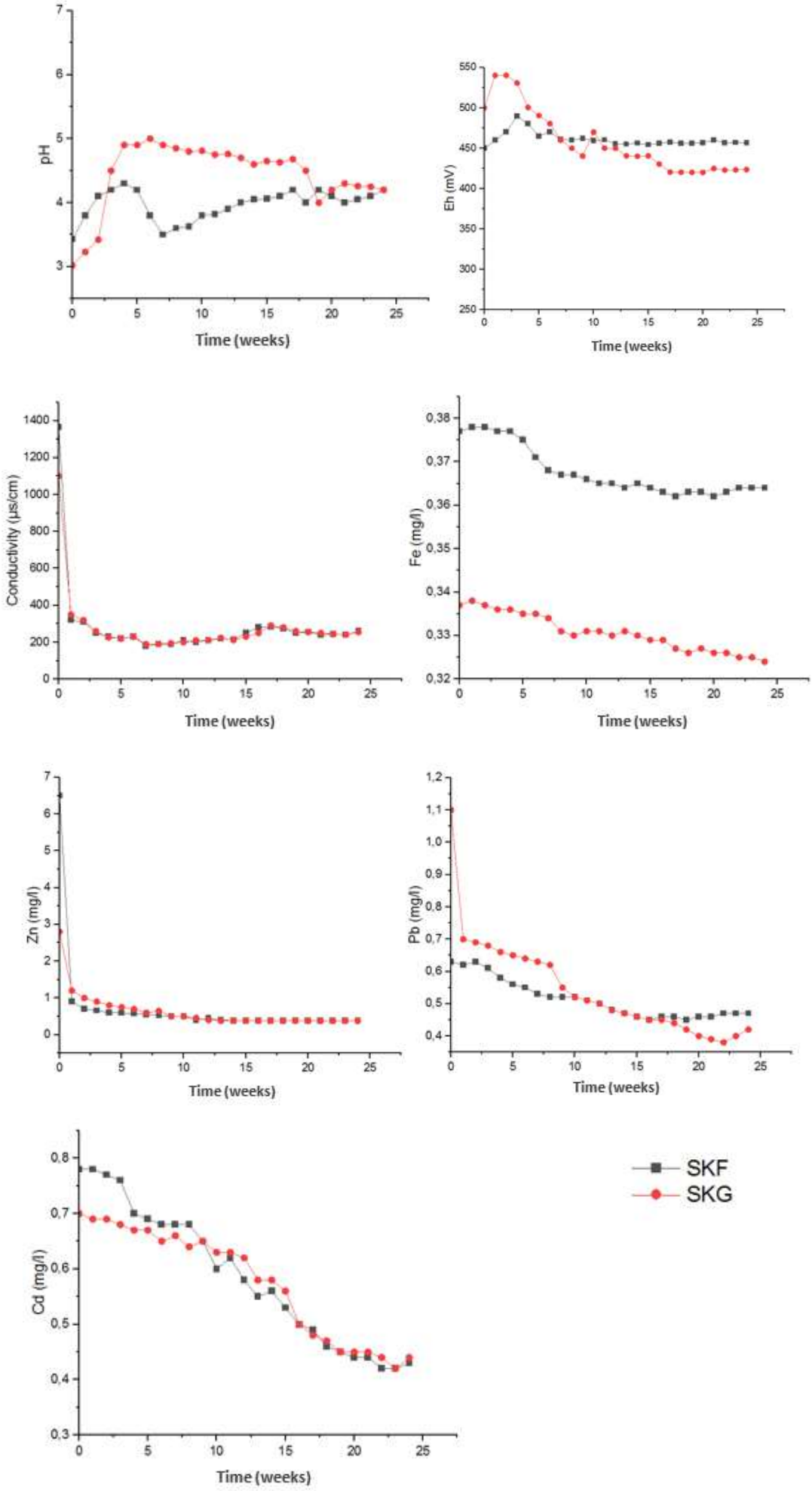

Fig.4 Water quality evolution during kinetic weathering cell test

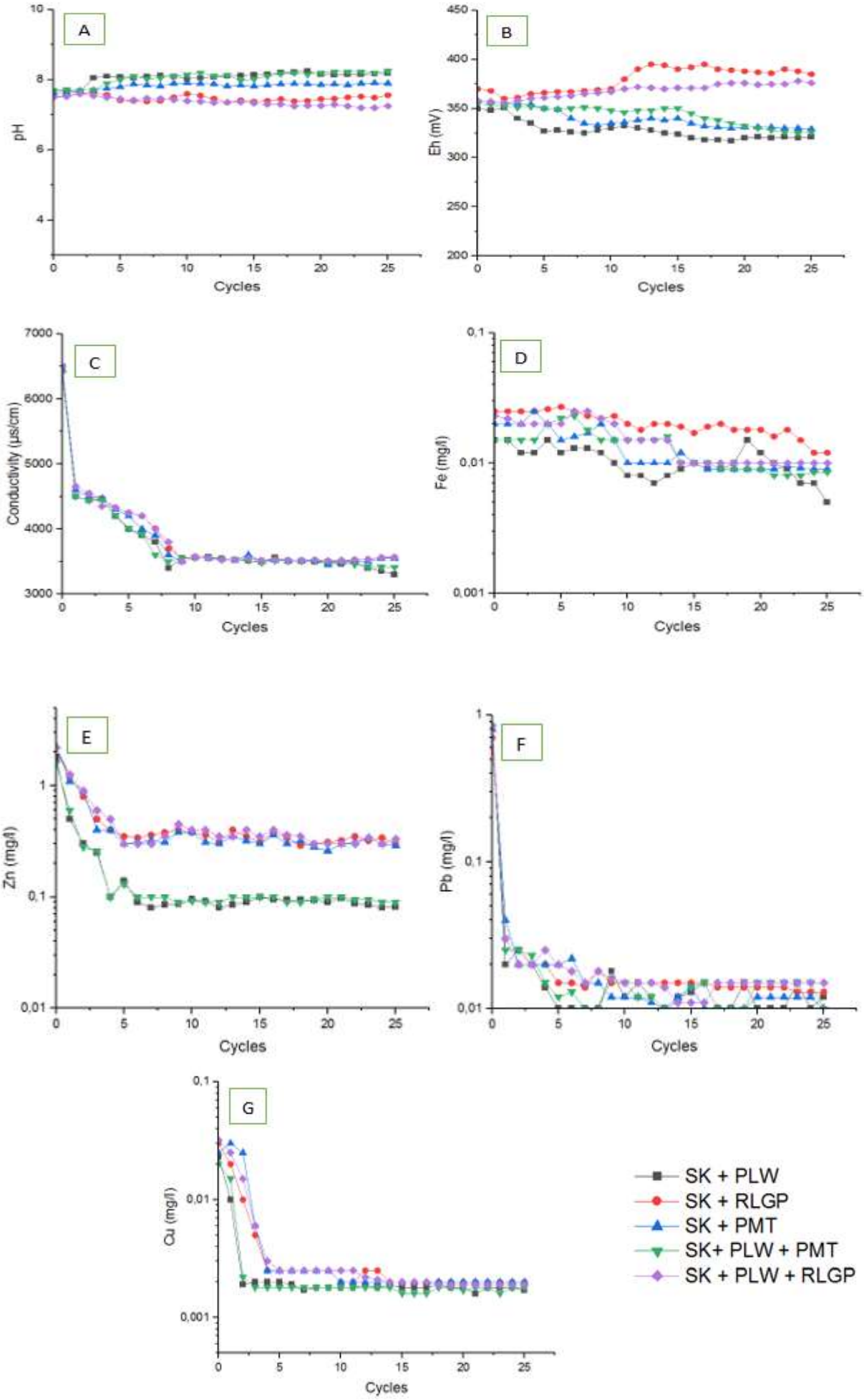

Fig.5: Water quality evolution of the amended tailings in the humidity cells tests

Low iron values were explained by precipitation of iron oxyhydroxides and/or iron phosphate. These results are consistent with those of Hakkou et al [33] using phosphate waste rock to control AMD from Kettara tailings (Morocco). The addition of 15 wt% alkaline phosphate wastes to these tailings produced leachates with lower acidities (7<pH<7.5) and metal concentrations than unamended controls.

Figure. 5e shows changes in Zn concentrations in leachate for 25 flushing cycles. Zinc showed a gradual decrease in concentration over time. The final concentrations of this metal in cells remained between 0.081 mg/L (C1) and 0.33 mg/L (C5). Zinc probably precipitated into all the cells. Zn immobilization is due to the ion exchange and complexation mechanisms; it results in the formation of Zn-containing phosphates [54]. The variation curves for lead concentration in all leachates indicated a descending trend from an initial concentration of (0.80 to 0.012 mg/L for C1), (0.71 to 0.013 mg/L for C2), (0.80 to 0.01 mg/L for C3), (0.82 to 0.01 mg/L for C4) and (0.85 to 0.015 mg/L for C5) **(Fig. 5f).** Xu et al [55] reported that lead can be immobilized in contaminated soils by phosphate rock (PR) amendment, but its efficiency is generally limited by low solubility of PR. Indeed, phosphate solubilizing bacteria (PSB) (*Pantoea ananatis* and *Bacillus thuringiensis*) can promote Pb immobilization through PR by producing citric, glucose, and a-Ketoglutaric acids. The variation of copper in leachates indicated that it had been easily eliminated by all alkaline amendments with final concentrations not exceeding 0.01 mg/L. These findings are in agreement with previous studies reported by Mignardi et al [56] where natural phosphate rock (PR) were used to heavy metal polluted soils from sulfide mine areas in Sardinia and Tuscany (Italy). The application of phosphate amendments to the polluted mine waste soils reduced water-soluble concentrations of metals by about 99 %. Mechanisms involved in the immobilization of metals by phosphates are: 1) ion exchange, 2) surface complexation, 3) precipitation of new metal phosphates, and 4) substitution of Ca in phosphate rocks by metals during recrystallization [22] [31] [36].

The results showed that phosphate compounds (PLW, RLGP and PMT) are effective amendments to immobilize metals (Pb, Zn, Cu, Fe,) in Sidi Kamber tailings. The Phosphate stabilization of metal-contaminated soils and wastes can be achieved in 3 phases: (1) dissolution of soluble, metal-bearing phases that need to be stabilized, (2) dissolution of a phosphate source, and (3) precipitation of insoluble metal phosphates. Previous studies suggested that acid buffering and metal retention in phosphate-amended materials can be the results of phosphate precipitation, Fe hydroxide formation, or carbonate dissolution and resultant acid neutralization [35] [57].

IV. CONCLUSION

The main objective of this study were to reduce the risk of environment contamination caused by AMD and metal leaching potential emanating from Sidi Kamber mine tailings. Weathering cell tests showed that higher concentrations of trace elements such as Cd, Cu, Pb, Zn and Fe were leached from these tailings. Humidity cell kinetic testing evaluated the effect of alkaline changes based on phosphate products and by-products from the Djebel Onk mine (phosphate limestone wastes, low phosphate crude ore, phosphate mine tailings) on the neutralization of the AMD. The results of the electrochemical and geochemical analysis of the leachates showed that all materials (used alone or in a mixture) are capable of immobilizing the metal elements (Pb, Zn, Cu, Fe) through the combination of highering the pHs and others processes such as adsorption/or co-precipitation. The insitu tests are recommended to evaluate the performance of this technique and its feasibility.

ACKNOWLEDGMENT

The authors thank the Research Institute on Mines and Environment (RIME- Canada) and its staff for their collaboration in the sample characterization, Dr Ema Bobocioiu from LGL-TPE of ENS Lyon (France) for assistance with mineralogical analysis.

REFERENCES

[1] M. Benzaazoua, B. Bussière, A.M. Dagenais, M. Archambault, "Kinetic tests comparison and interpretation for prediction of the Joutel tailings acid generation potential", Environmental geology, 46(8), 1086-1101. 2004. https://doi.org/10.1007/s00254-004-1113-1

[2] B. Bussière, M. Benzaazoua, M. Aubertin, M. Mbonimpa, "A laboratory study of covers made of low-sulphide tailings to prevent acid mine drainage". Environmental Geology 45(5):609-622, 2004. https://doi.org/10.1007/s00254-003-0919-6.

[3] Kitobo, "Dépollution et valorisation des rejets miniers sulfurés du katanga « cas des tailings de l'ancien concentrateur de kipushi »', thèse de Doctorat en Sciences de l'ingénieur, Univ de Liège, 2009, 254p.

[4] B. Plante, G. Schudel, M. Benzaazoua, "Generation of acid mine drainage. In: Hard rock mine reclamation: From prediction to management of acid mine drainage". Bussière, B., Guittonny, M. (Eds.), CRC Press, pp. 1-20. 2021.

[5] R. Pelletier, "Caractérisation et neutralisation du drainage minier acide par une dolomie à haute pureté". Sherbrooke University, Canada. 2014

[6] R. Potvin, "Évaluation à différentes échelles de la performance de systèmes de traitement passif pour des effluents fortement contaminés par le drainage minier acide". Thèse de Doctorat, Université du Québec en Abitibi-Témiscamingue, Rouyn-Noranda, QC, Canada, 367 p, 2009.

[7] Y. Itard, R. Bosc, "Traitements et préventions des drainages acides provenant des résidus miniers". Revue bibliographique, BRGM/RP-50829-FR, 88p. 2001.

[8] M. Jouini, M. Benzaazoua, C.M. Neculita, "Stabilization/solidification of acid mine drainage treatment sludge." In: Low carbon stabilization and solidification of hazardous wastes. Wang, L., Tsang, C.W. (Eds.), Elsevier (in press), 2021.

[9] T. Genty, B. Bussière, R. Potvin, M. Benzaazoua, G.J. Zagury, "Dissolution of calcitic marble and dolomitic rock in high iron concentrated acid mine drainage: application to anoxic limestone drains". Environ. Earth Sci. 66, 2387–2401. 2012 https://doi.org/10.1007/s12665-011-1464-3

[10] A. Akcil, S. Koldas, "Acid Mine Drainage (AMD): causes, treatment and case studies". Journal of Cleaner Production. 14, 1139-1145, 2006 https://doi.org/10.1016/j.jclepro.2004.09.006

[11] M.P. Éthier, "Évaluation du comportement géochimique en conditions normale et froides de différents stériles présents sur le site de la mine Raglan". Mémoire de Maîtrise, École Polytechnique de Montréal, Montréal, QC, Canada, 237 p. 2011. https://depositum.uqat.ca/id/eprint/647

[12] G. S. Simate, S. Ndlovu, "Acid mine drainage: Challenges and opportunities". Journal of Environmental Chemical Engineering, Volume 2, Issue 3, Pages 1785-1803. 2014. https://doi.org/10.1016/j.jece.2014.07.021.

[13] A. Shane, X. Xu, J. Siame, A. Nguvulu, T. Tena, M. Lungu, S. Chinyanta, J. Kawala, V. Bowa, B. Chirambo, "Removal of Copper from Acid Mine Drainage (AMD) or Acid Rock Drainage (ARD)". Journal of Water Resource and Protection, 13, 435-454. 2021. doi: 10.4236/jwarp.2021.137026.

[14] C.A. Cravotta, "Size and performance of anoxic limestone drains to neutralize acid mine drainage". J. Environ. Qual. 32, 1277, 2003. https://doi.org/10.2134/jeq2003.1277

[15] T.M. Valente, M. Antunes, M.A. Sequeira Braga, M.I. Prudêncio, R. Marques, J. Pamplona, "Mineralogical attenuation for metallic remediation in a passive system for mine water treatment". Environmental Earth Sciences, 66, Issue 1: 39-54, 2012. https://doi.org/10.1007/s12665-011-1205-7

[16] O. Ouakibi, S. Loqman, R. Hakkou, M. Benzaazoua, "The potential use of phosphatic limestone wastes in the passive treatment of AMD: A laboratory study". Mine Water Environ. 32, 266–277, 2013. https://doi.org/10.1007/s10230-013-0226-8

[17] J. Skousen, C.E. Zipper, A. Rose, P.F. Ziemkiewicz, R. Nairn, L.M. McDonald, R.L. Kleinmann, "Review of passive systems for acid mine drainage treatment". Mine Water Environ. 36, 133-153. 2017. https://doi.org/10.1007/s10230-016-0417-1

[18] K. Rambabu, F. Banat, Q.M. Pham, S.H. Ho, N.Q. Ren, P.L. Show, "Biological remediation of acid mine drainage: Review of past trends and current outlook". Environ. Sci. Ecotechnol. 2, 100024, 2020. https://doi.org/10.1016/j.ese.2020.100024

[19] C.M. Neculita, G.J. Zagury, B. Bussière, "Passive treatment of acid mine drainage at the reclamation stage". In: Hard rock mine reclamation: From prediction to management of acid mine drainage. Bussière, B., Guittonny, M. (Eds.), CRC Press, pp. 271-296, 2021.

[20] S. Nfissi, S. Alikouss, Y. Zerhouni, Z. Baroudi, M. Samir, "Alkaline amendment based of sludge pulp of sweets and clays: application to the tailings of the abandoned kettara mine (morocco)". Ann. Soc. Géol. Nord, T. 25 (2e série), p. 75-81, 2018.

[21] A. Elghali, M. Benzaazoua, B. Bussière, T. Genty, "In situ effectiveness of alkaline and cementitious amendments to stabilize oxidized acid-generating tailings". *Minerals 9*, 314, 2019. https://doi.org/10.3390/min9050314

[22] S. Mignardi, A. Corami, V. Ferrini, "Evaluation of the effectiveness of phosphate treatment for the remediation of mine waste soils contaminated with Cd, Cu, Pb, and Zn". Chemosphere 86(4), 354-360, 2012. https://doi.org/10.1016/j.chemosphere.2011.09.050

[23] M. Andrunik, M. Wołowiec, D. Wojnarski, S. Zelek-Pogudz, T. Bajda, "Transformation of Pb, Cd, and Zn minerals using phosphates". *Minerals 10*, 342, 2020. https://doi.org/10.3390/min10040342

[24] M. Ettoumi, M. Jouini, C.M. Neculita, S. Bouhlel, L. Coudert, Y. Taha, M. Benzaazoua, "Characterization of phosphate processing sludge from Tunisian mining basin and its potential valorization in fired bricks making". J. Clean. Prod. 284, 124750, 2021. https://doi.org/10.1016/j.jclepro.2020.124750

[25] M. Ettoumi, M. Jouini, C.M. Neculita, S. Bouhlel, L. Coudert, I. Haouech, M. Benzaazoua, "Characterization of phosphate sludge at GPC, Gafsa, Tunisia, and optimization of its dewatering". J. Environ. Manage. 254, 109801, 2020. https://doi.org/10.1016/j.jenvman.2019.109801

[26] Chaguer, "Analyse et Spéciation des Métaux dans un Oued en zone minière. Cas de l'Oued Essouk". University Constantine I, Algeria, 146p, 2013.

[27] M. Khelfaoui, M.S. Medjram, A. Kabir, D. Zouied, K. Mehri, O. Chikha, M. AyadiTrabelsi, "Chemical and mineralogical characterization of weathering products in mine wastes, soil, and sediment from the abandoned Pb/Zn mine in Skikda, Algeria". Environ EarthSci. 79, 293, 2020. https://doi.org/10.1007/s12665-020-09043-x

[28] N. Charchar, L. Bouchaala, H. Bouyahmed, G. Gherib, A. Lehout, "Effect of heavy metals on soil microbial quality of an abandoned mining area Sidi Kamber, North-East of Algeria". Eurasian Journal of Soil Science, 9 (3), 254-263, 2020. https://doi.org/10.18393/ejss.735971

[29] C. Boukhalfa, M. Chaguer, "Characterisation of sediments polluted by acid mine drainage in the northeast of Algeria". Int.J. Sediment Res. 27, 402-407, 2012. https://doi.org/10.1016/S1001-6279(12)60045-6

[30] M. Issaad, A. Boutaleb, O. Kolli, M. Edahbi, M. Benzaazoua, R. Hakkou, "Environmental characterization of mine waste at the Pb–Zn Sidi Kamber abandoned mine (NE Algeria)". Rend. Fis. Acc. Lincei30,427-441, 2019.https://doi.org/10.1007/s12210-019-00806-8

[31] A. Merchichi, M. Ould Hamou, M. Edahbi, E. Bobocioiu, C.M Neculita, M. Benzazoua, "Passive treatment of acid mine drainage from the Sidi-Kamber minewastes (Mediterranean coastline, A Algeria) using neighbouring phosphate material from the Djbel Onk Mine". Science of the Total Environment, https://doi.org/10.1016/j.scitotenv.2021.151002

[32] M. Aubertin, B. Bussière, L. Bernier, "Environnement et gestion des résidus miniers". Cédérom, Les Éditions de l'École Polytechnique de Montréal, 2002.

[33] R. Hakkou, M. Benzaazoua, B. Bussière, "Laboratory evaluation of the use of alkaline phosphate wastes for the control of acidic mine drainage". Mine Water Environ. 28, 206, 2009. https://doi.org/10.1007/s10230-009-0081-9

[34] M. Chrysochoou, D. Dermatas, D.G. Grubb, "Phosphate application to firing range soils for Pb immobilization: the unclear role of phosphate". J Hazard Mater 144:1–14, 2007. https://doi.org/10.1016/j.jhazmat.2007.02.008

[35] N. C. Munksgaard, B. G. Lottermoser, "Phosphate amendment of metalliferous tailings, Cannington Ag–Pb–Zn mine, Australia: implications for the capping of tailings storage facilities". Environ Earth Sci (2013) 68:33–44, 2012. https://doi.org/10.1007/s12665-012-1711-2

[36] X. Cao, "Immobilization of Heavy Metals in Contaminated Soils Amended by Phosphate-, Carbonate-, and Silicate-Based Materials: From Lab to Field". In: Luo Y., Tu C. (eds) Twenty Years of Research and Development on Soil Pollution and Remediation in China. Springer, Singapore, 2018. https://doi.org/10.1007/978-981-10-6029-8_32

[37] J. Aubouin, H. Gaussen, H. Harant, "Méditerranéenne aire. Encyclopædia Universalis". Accessed, 2018.

[38] J.A. Bolfa, "Contribution à l'étude des gîtes métallifères de la Kabylie de Collo et de la région de Bône". impr. Berger-Levrault. Nancy, Paris, Strasbourg, 1948.

[39] S. Chabou-Mostefai, "Étude de la série phosphatée tertiaire du Djebel Onk, Algérie, Stratigraphie, Pétrographie, Minéralogie et Analyse Statistique". PhD Thesis, Université de Droit, d'Économie et des Sciences d'Aix-Marseille, France,376p, 1987.

[40] R. Kechiched, R. Laouar, O. Bruguier, S. Salmi-Laouar, L. Kocsis, D. Bosch, A. Foufou, O. Ameur-Zaimeche, H. Larit, "Glauconite-bearing sedimentary phosphorites from the Tébessa region (eastern Algeria) : Evidence of REE enrichment and geochemical constraints on their origin". J. Afr. Earth Sci. 145, 190-200,2018. https://doi.org/10.1016/j.jafrearsci.2018.05.018

[41] R. Kechiched, R. Laouar, O. Bruguier, L. Kocsis, S. Salmi-Laouar, D. Bosch, O. Ameur-Zaimeche, A. Foufou, H. Larit, "Comprehensive REE + Y and sensitive redox trace elements of Algerian phosphorites (Tébessa, eastern Algeria): A geochemical study and depositional environments tracking". J. Geochem. Explor. 208, 106396, 2020. https://doi.org/10.1016/j.gexplo.2019.106396

[42] M. Jouini, C.M. Neculita, T. Genty, M. Benzaazoua, "Environmental behavior of metal-rich residues from the passive treatment of acid mine drainage". Sci. Total Environ. 712, 136541, 2020. https://doi.org/10.1016/j.scitotenv.2020.136541

[43] H. Bouzahzah, M. Benzaazoua, B. Bussiere, B. Plante, "Prediction of Acid Mine Drainage: Importance of Mineralogy and the Test Protocols for Static and Kinetic Tests". Mine Water Environ 33, 54–65, 2014. https://doi.org/10.1007/s10230-013-0249-1

[44] K. Lounate, L. Coudert, T. Genty, G. Mercier, J.F. Blais, "Performance of a Semi-passive Sulfate-reducing Bioreactor for Acid Mine Drainage Treatment and Prediction of Environmental Behavior of Post-treatment Residues". Mine Water Environ 39, 769–784, 2020. https://doi.org/10.1007/s10230-020-00702-w

[45] M. Villeneuve, "Evaluation du comportement géochimique à long terme de rejets miniers à faible potentiel de génération d'acide à l'aide d'essais cinetiques". Mémoire de maitrise en sciences appliquées (Génie minéral), Département des génies civil, géologique et des mines. Université de Montréal, Quebec, Canada, 2004.

[46] B. Plante, M. Benzaazoua, B. Bussière, "Predicting Geochemical Behaviour of Waste Rock with Low Acid Generating Potential Using Laboratory Kinetic Tests". Mine Water and the Environment: 1-20, 2010. https://doi.org/10.1007/s10230-010-0127-z

[47] M. Jouini, T.V. Rakotonimaro, C.M Neculita, T.Genty, M. Benzaazoua, "Prediction of the environmental behavior of residues from the passive treatment of acid mine drainage". Applied Geochemistry, Volume 110, 104421. 2019. https://doi.org/10.1016/j.apgeochem.2019.104421.

[48] R.L.P Kleinmann, P.M Erickson, "Field evaluation of a bactericidal treatment to control acid drainage. In: Graves DH (ed) Proceedings of the symposium on surface mining hydrology, sedimentology and reclamation". University of Kentucky, Lexington, KY, pp 325–329, 1981.

[49] R. Hakkou, M. Benzaazoua, B. Bussière, "Environmental characterization of the abandoned kettara mine wastes (MOROCCO)". Post-Mining, Nancy, France, 2005.

[50] K. U. Mayer, E. O. Frind, D. W. Blowes, "Multicomponent reactive transport modeling in variably saturated porous media using a generalized formulation for kinetically controlled reactions". Water Resources Research, 38(9), 2002. https://doi.org/10.1029/2001WR000862

[51] R. Hakkou, M. Benzaazoua, B. Bussière, "Acid mine drainage at the abandoned Kettara mine (Morocco): 2. Mine Waste Geochemical Behavior". Mine Water Environment 27, 160–170, 2008.

[52] G. Furrer, W. Stumm, "The coordination chemistry of weathering I. dissolution kinetics of Al2O3 and BeO". Geochim Cosmochim Acta 50:1847–1860, 1986. https://doi.org/10.1016/0016-7037(86)90243-7

[53] J. Schott, O. S. Pokrovsky, E. H. Oelkers, "The Link Between Mineral Dissolution/Precipitation Kinetics and Solution Chemistry". Reviews in Mineralogy and Geochemistry, 70(1), 207–258, 2009. https://doi.org/10.1515/9781501508462-008

[54] Y. Charuseiam, S. Chotpantarat, C. Sutthirat, "Acid mine drainage potential of waste rocks in a gold mine (Thailand): application of a weathering cell test and multivariate statistical analysis". Environ Geochem Health 44, 1049–1079, 2022. https://doi.org/10.1007/s10653-021-00976-1

[55] J. Xu, L. Huang, C. Chen, J. Wang, X. Long, "Effective lead immobilization by phosphate rock solubilization mediated by phosphate rock amendment and phosphate solubilizing bacteria", Chemosphere, Volume 237, 124540, 2019. https://doi.org/10.1016/j.chemosphere.2019.124540

[56] S. Mignardi, A. Corami, V. Ferrini, "Immobilization of Co and Ni in Mining-Impacted Soils Using Phosphate Amendments". Water Air Soil Pollut 224, 1447, 2013. https://doi.org/10.1007/s11270-013-1447-y

[57] A. Mauric, B.G. Lottermoser, "Phosphate amendment of metalliferous waste rocks, Century Pb–Zn mine, Australia: Laboratory and field

trials", Applied Geochemistry, Volume 26, Issue 1, Pages 45-56, 2011. https://doi.org/10.1016/j.apgeochem.2010.11.002.

Amira Merchichi is an assistant professor at Ecole Nationale Polytechnique, Algiers, Algeria, since 2014. Her research interests are mining environment, mineral processing, biomining.

Malek Ould Hamou is a professor at Ecole Nationale Polytechnique, Algiers, Algeria. He was the head of mining engineering department and the director of the mining engineering laboratory of the same establishment. His research interests are mineralurgy, bio-processing and mining environment.

Mostafa Benzaazoua joined the University of Quebec (UQAT) in 1996, as postdoctoral fellow. He became professor in June 1997 in the same university. His research interests are in Sediments, Cement, Solidification, Ore Geology, Exploration Geology, Mineralogy, Waste Management, Geochemistry, Acid Mine Drainage.

Farid Aghilas Mansour is a PhD student at the Department of Mining Engineering, Ecole Nationale Polytechnique, Algiers, Algeria. His research interests are in Geochemistry, Geostatistics and Mineralogy.

Nabil Babahoum received the degree of Engineer and Master's degree in 2014 and Ph.D in 2022, in mining engineering from Ecole Nationale Polytechnique (ENP) of Algiers. He is a WellSite Geologist at SONATRACH since 2015.

Hakim Rabia received the degree of Engineer and Master's degree in 2015 and Ph.D in 2021, in mining engineering from Ecole Nationale Polytechnique (ENP) of Algiers.

Kernel SVM Classifiers based on Fractal Analysis for Estimation of Hearing Loss

Mohamed Djemai and Mhania Guerti

Abstract− Hearing screening consists of analyzing the hearing capacity of an individual, regardless of age. It identifies serious hearing problems, degree, type and cause of the hearing loss and the needs of the person to propose a solution. Auditory evoked potentials (AEPs) which are detected on the EEG auditory cortex area are very small signals in response to a sound stimulus (or electric) from the inner ear to the primary auditory areas of the brain. AEPs are noninvasive methods used to detect hearing disorders and to estimate hearing thresholds level. In this paper, due to the nonlinear characteristics of EEG, Detrented Fluctuation Analysis (DFA) is used to characterize the irregularity or complexity of EEG signals by calculating the Fractal Dimension (FD) from the recorded AEP signals of the impaired hearing and the normal subjects. This is to estimate their hearing threshold. In order to classify both groups, hearing-impaired and normal persons, support vector machine (SVM) is used. For comparably evaluating the performance of SVM classifier, three kernel functions: linear, radial basis function (RBF) and polynomial are employed to distinguish normal and the abnormal hearing subjects. Grid search technique is selected to estimate the optimal kernel parameters. Our results indicate that the RBF kernel SVM classifier is promising; it is able to obtain a high training as well as testing classification accuracy.

***Keywords*− Auditory evoked potentials, Hearing Thresholds, Detrented Fluctuation Analysis, Grid search, Support Vector Machine.**

NOMENCLATURE

AEP	Auditory evoked potentials.
ABR	Auditory Brainstem Response.
DFA	Detrented Fluctuation Analysis.
EEG	Electroencephalogram.
FD	Fractal Dimension.
RBF	Gaussian radial basis function.
SVM	Support Vector Machine.

I. INTRODUCTION

Hearing loss is a pathological state of hearing characterized by a partial or total loss or even early or late loss of sound perception. The consequences of hearing impairment include miscommunication and psychological problems [1]. In the absence of corrective measures, there could be 630 million people with hearing loss by 2030 and almost 900 million by 2050 [2].

Hearing screening consists of analyzing the hearing capacity of an individual, regardless of age. It identifies serious hearing problems, degree, type and cause of the hearing loss and the needs of the person to propose a solution.

AEP signal is the screening technique used to distinguish between pathological and healthy cases. AEP signals are a recording of a subject's electroencephalogram (EEG) from the auditory pathways leading sound from the inner ear to the primary auditory areas of the brain in response to a short auditory stimulus. AEPs are an objective tool for assessing hearing function, used to identify potential problems in the auditory neural pathway and to estimate hearing thresholds [3].

Fractals are mathematical objects used to describe natural phenomena such as clouds, branches of trees, rocky coasts, leaves, the bronchi of our lungs that present a certain irregularity or roughness, in the face of which Euclidean geometry does not allow correctly describe this irregularity. Fractals have a character called self-similarity or scale invariance. Several natural phenomena have longer-term time dependencies: the correlations in the series remain in a durable way. These properties indicate the presence of a fractal structure. It is thanks to the introduction of the theory of fractals (from the Latin fractus: irregular, interrupted) by Benoît Mandelbrot in the 1970s that a new description of these complex objects could be established [4]. The fractal dimension (FD) is a non-integer number; it can be a fraction, an irrational number or a whole number which measures the degree of irregularity of an object and also makes it possible to quantify the notion of self-similarity or the degree of fluctuation of time series.

DFA is prominent method to quantify the fractal-scaling index of time series. In this study, DFA method is employed to estimate the FD of hearing impaired and normal subjects.

Manuscript received April 26, 2022; revised July 25, 2022.

M. Djemai is with Ziane Achour university, Djelfa, Algeria.
(e-mail: mohamed_djemai2@yahoo.fr)
M. Guerti is with Ecole Nationale Polytechnique
(e-mail: mhania.guerti@g.enp.edu.dz).

Digital Object Identifier (DOI): 10.53907/enpesj.v2i1.88

I. RELATED WORK

A. Detrended Fluctuation Analysis (DFA)

DFA is a method specially designed for the analysis of signals possessing the property of self-similarity [5] and detection of long-term correlations in non-stationary time series. It is the most frequently used method in different areas due to its simple construction and to its excellent results [6] such as: DNA sequencing, Study of heart rate variability, long-time weather records, structure clouds, geology, ethnology, economic time series and solid state physics [7]. Ivan Seleznov et al. applied DFA method to identify activation changes in brain dynamics

during mental computations, which reveals a permanent information communication during brain activity [8]. Jing et al. [9] used the DFA to assess the temporal correlation properties of the EEG in drug dependence. The results obtained confirmed the effect of the drug-related stimulus on the EEG scaling behavior.

We compute the integrated series from each data point:

$$y(k) = \sum_{k=1}^{K} (x(k) - \bar{x}), \quad (1)$$

where $\bar{x}$ is the average of the global signal.

The integrated series $y(k)$ is then divided into equal-sized, non-overlapping boxes of length n. In each box, the linear fit is calculated by using least squares, the resulting vector, $y_n(k)$, is then substracted to y(k) as follows:

$$F(n) = \sqrt{\frac{1}{N}\sum_{k=1}^{N}\left(y(k) - y_n(k)\right)^2}, \quad (2)$$

The above computation will be repeated for segment sizes n (different scales) to give a relationship between F (n) and n. Typically, $F(n)$ will increase linearly with segment size n. The slope of the line F(n) determines the scaling α exponent [10]. FD = 3- α.

B. Support Vector Machine

SVMs are a class of supervised learning algorithms designed to solve discrimination and regression or anomaly detection problems. It seeks to find among an infinity of linear classifiers (hyperplanes), the optimal hyperplane which separates the data into two different classes by following the criterion of maximum margin.

The margin is the distance between the separation boundary and the observations closest to the hyperplane (support vectors) [11].

SVM is the most widely used technique due to its better generalization performance and capability to work well in higher dimensional space [12]. It has better learning ability and smaller test errors than other methods for different datasets [13].

B.1. Separable Data

For two-classes, separable training data sets, there is an equation hyperplane $w.x + b = 0$ such as:

$$\begin{cases} w.x_i + b \geq 1 & \text{for } y_i = +1 \\ w.x_i + b \leq -1 & \text{for } y_i = -1 \end{cases} \quad (3)$$

The last two constraints can be combined into:

$$y_i(w.x_i + b) \geq +1. \quad (4)$$

The optimal separating hyper plane can be obtained by solving the following optimization problem :

$$\min \frac{1}{2} w^T w \quad \text{subject to} : y_i(w.x_i + b) \geq +1. \quad (5)$$

The problem is a quadratic optimization problem; the Lagrangian associated to the problem becomes:

$$L(w, b, \alpha) = \frac{1}{2} w^T w - \sum_{i=1}^{m} \alpha_i (y_i(w.x_i + b) - 1), \quad (6)$$

Where $\alpha_i \geq 0$ are the Lagrange multiplier.

By differentiating L with respect to w and b, L is converted into a dual Lagrangian $L_D(\alpha)$

$$\max_{\alpha} L_D(\alpha) = \sum_{i=1}^{m} \alpha_i - \frac{1}{2}\sum_{i=1}^{m}\sum_{j=1}^{m} \alpha_i \alpha_j y_i y_j x_i x_j, \quad (7)$$

$$s.t : i = 1, \dots, m \ \ \alpha_i \geq 0 \text{ and } \sum_{i=1}^{m} \alpha_i y_i = 0,$$

$L_D(\alpha)$ should be maximized with respect to α_i to obtain the best hyperplane. The α_i vector can be calculated also as a quadratic optimization problem.

B.2. *Non-separable Data*

In the nonlinearly separable case, SVM is modified by introducing slack variables ξ_i for measuring classification errors with $\xi_i \geq 0 \ i = 1, \dots, m$

Therefore, we can write the optimization problem as:

$$\min_{w,b,\xi} \frac{1}{2} w^T w + C \sum_{i=1}^{m} \xi_i, \quad (8)$$

$$s.t : y_i(w.x_i + b) + \xi_i \geq +1, \qquad \xi_i \geq 0.$$

The parameter C > 0 controls the tradeoff between increasing the margin and reducing the errors. The Lagrange multipliers α_i should be employed to solve the Optimization problem Eq. (8) that transforms it to dual form.

In the linearly separable case, a non-linear vector mapping function (ϕ) should be used to transform the data to a higher-dimensional feature space. This process is done through the kernel function, presumably making the separation easier in that space [14].

The optimal hyperplane can be obtained by solving:

$$\max_{\alpha} L_D(\alpha) = \sum_{i=1}^{m} \alpha_i - \frac{1}{2}\sum_{i=1}^{m}\sum_{j=1}^{m} \alpha_i \alpha_j y_i y_j K(x_i, x_j), \quad (9)$$

$$s.t : 0 \leq \alpha_i \leq C \ i = 1, \dots, m \ \text{ and } \sum_{i=1}^{m} \alpha_i y_i = 0,$$

where $\alpha = (\alpha_1, \alpha_2, \dots, \alpha_m)$ is the vector of non negative Lagrange multipliers associated with the constraints $\sum_{i=1}^{m} \alpha_i y_i = 0$ and $0 \leq \alpha_i \leq C$, $i = 1, \dots, m$.

Three commonly used kernel functions are listed below:

The Gaussian radial basis function (RBF): $K(x_i, x_j) = exp\frac{-\|x_i - x_j\|^2}{2\sigma^2}$;

The polynomial kernel: $K(x_i, x_j) = (x_i.x_j + 1)^d$;

The linear kernel: $K(x_i, x_j) = (x_i.x_j + 1)$.

Here, σ and d are kernel parameters. σ is the spread of the Gaussian function.

The order of the polynomial kernel d controls the flexibility of SVM model and affects its accuracy [15].

C. Grid Search

There are many optimization Kernel parameters methods for SVM such as: particle swarm optimization algorithm, genetic algorithm and Grid Search.

Huang et al [16]. used wavelet features and traditional spectral features as input features to construct fusarium head blight

detection models in combination with the particle swarm optimization support vector machines (PSO-SVM) approach. PSO is applied to simultaneously optimize both the penalty parameter c and the radial basis function parameter gamma. The results show that the PSO-SVM detection method yielded a higher overall accuracy compared to the back propagation neural network (BPNN) detection method.
Djemai et al [17]. developed a hybrid approach in whereby they combined the genetic algorithm and SVM model to classify normal and abnormal hearing subjects using FD features that were extracted from the AEP responses of the subjects applying DFA algorithm. This combination leads to achieve considerably higher performance compared to standard SVM.

In this study, Grid Search is chosen because it straightforward hyperparameter tuning method [18]. It is easier to implement and it is that it cannot get struck in local maximum.
The Grid Search method is a technique whose goal is to methodically determine the best combination of hyperparameters over the designated range that can facilitate the construction of a model in a given set. It consists of exploring all the possible combinations of values on a set of models that differ from each other in their parameter values, which are on a grid seeking the best combination that has achieved the best performance score on the test data. X. Wang et al. developed a hybrid algorithm based on SVM and the search grid method to make better use of soil salinization information [19]. F. Budiman applied the search grid method to analyze and test the optimization range of SVM-RBF kernel parameter values to recognize the image possessing geometric decorative motifs [20].

D. K-fold Cross Validation (KCV)

Cross-validation (CV) is an approach employed to evaluate the efficiency of machine learning models. It is used in modeling based on data that has properties such as: complexity, distribution, correlation between variables, etc [21].

The KCV randomly splits the training data T into k equal groups. One fold is going to be used as the validation set, and the rest $T_1 \ldots T_K, T_{K-1}$ are for the training set. This procedure should be done k times but using a different fold for the validation set.

II. MATERIALS AND METHODS

A. *Dataset*

Twenty participants, ages 15 to 29 (15 men, 5 women), took part in the experiment, divided into two groups: the normal hearing group consisting of ten participants between the ages of 21 and 28; The hearing-impaired group consists of five females and five males, ages 15 to 29. Participants in both groups are in good health and are not taking any medicines.
First, the hearing threshold t_h is measured for all participants using screening pure-tone audiometry [10].

- Normal hearing was defined as having $t\_h \leq 20$ dB.
- Hearing impaired was defined as having $t\_h > 20$ dB.

B. Data analysis

EEG signals were recorded using 10-20 electrode positioning system with 19 electrodes [10]. Using the headphones, the participants were prepared to perceive click sound at 4000 Hz, 2000 Hz, 1000 Hz and 500 Hz with an intensity of 20 dBHL in the right and the left ear. We record the AEP signals with a sampling frequency of 256 Hz. This procedure should be done for five trials and the participants are given a one-minute rest period between trials.

For all participant, FD was estimate from AEP signals obtained from 19 channels by DFA method [10].
We obtained the database that was used in this experiment by acoustic research lab, University Malaysia Perlis.
For comparably evaluating the efficiency of linear kernel SVM classifier, polynomial kernel SVM classifier and RBF kernel SVM classifier, we perform experiments to distinguish between the normal hearing subjects and the hearing impaired subjects using FD vectors obtained from the subject's recorded AEP.

In this work, 5-fold CV technique was selected to estimate the competence of the SVM classifiers. The results obtained will be optimized by grid search method.
Grid search technique is selected to estimate the optimal parameters for three kernel functions: linear, radial basis function (RBF) and polynomial, in which the values of the parameters are changed over the selected parameter ranges with fixed step sizes, and the efficiency of all groups of parameters is measured and compared.
The range of C,σ and d values tested is as follows:
For the linear and RBF kernel SVM classifiers, The range of C is from $2^{-5}$to 2^{10}, increasing in steps of the power of two ;
The Gaussian width σ for the RBF kernel ranged from 2^{-1} to 2^{5}, increasing in steps of the power of two ;
The order of the polynomial kernel d ranged from 1 to 10 by integers.
The model with the optimized parameters has the highest classification rate.
Fig. 2 shows the flowchart of SVM classifier model using grid search.

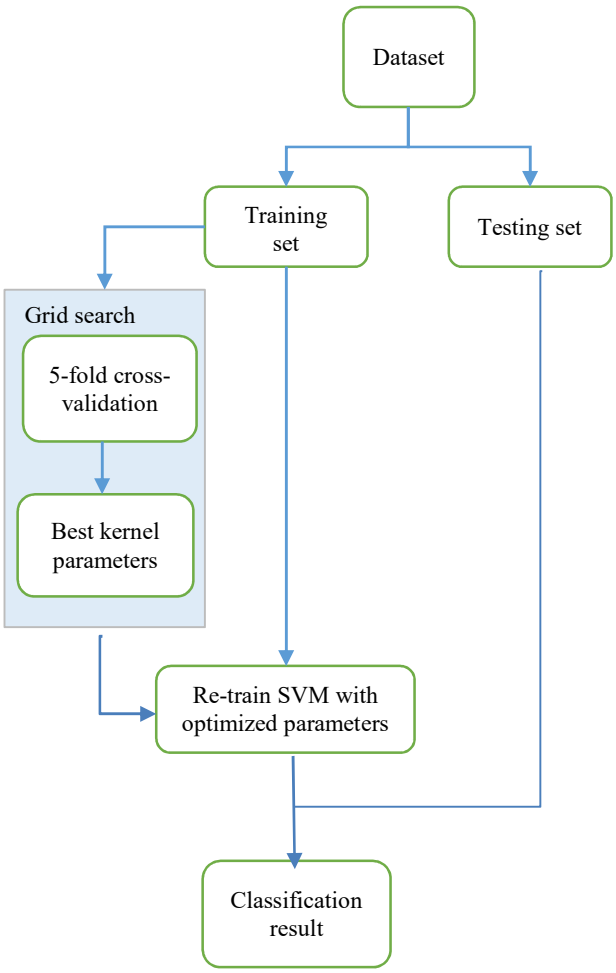

Fig. 1: Flowchart of SVM classifier model using grid search

III. RESULTS AND DISCUSSION

The linear kernel SVM classifier yields accuracy equal to 82.86% with parameter C worth 2^5. As shown in Fig.2.

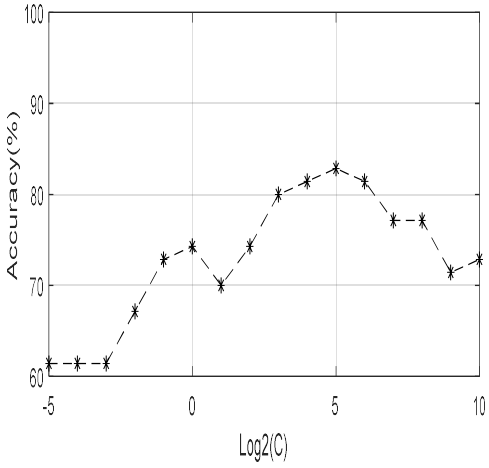

Fig. 2: Linear kernel parameter optimization using grid search

Figures 3 shows the parameters optimization results of polynomial kernel SVM classifier, using grid search method. The best classification accuracy of 85.71% achieves at $C=2^{-2}$ and d=2.

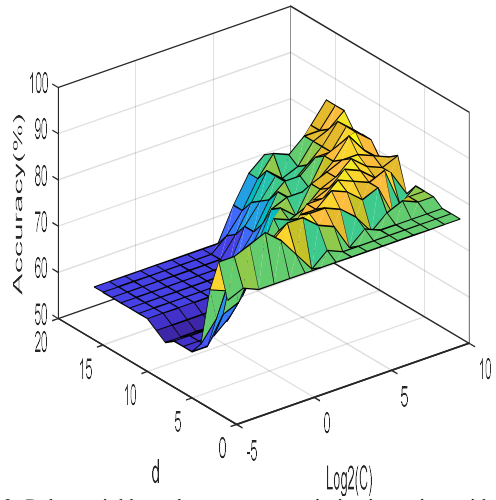

Fig. 3: Polynomial kernel parameters optimization using grid search

As shown in Fig. 4, Using grid search method, find out the optimal values of σ and margin parameter C. Which gives $\sigma = 2^{-1}$ and $C=2^2$ with the classification accuracy 95.82%.

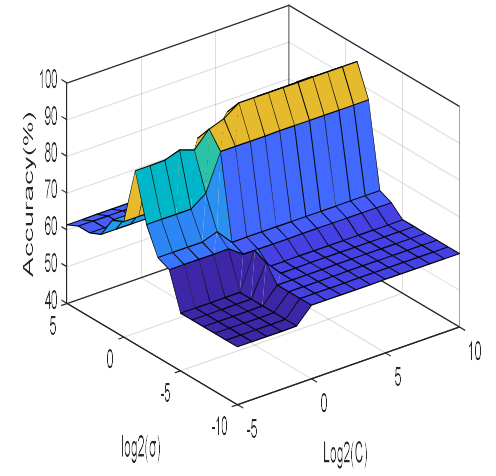

Fig. 4: RBF kernel parameters optimization using grid search

The classification rates of linear kernel SVM classifier, RBF kernel SVM classifier and polynomial kernel SVM classifier and are given in Table. I.

Table. I
CLASSIFICATION OF HEARING PERCEPTION LEVELS USING LINEAR KERNEL SVM CLASSIFIER, RBF KERNEL SVM CLASSIFIER AND POLYNOMIAL KERNEL SVM CLASSIFIER

Classifier		Linear SVM		Polynomial SVM		RBF-SVM	
Frequency (Hz)	Ear	Training Accuracy %	Testing Accuracy %	Training Accuracy %	Testing Accuracy %	Training Accuracy %	Testing Accuracy %
500	R	84.16	81.73	85.27	81.93	96.40	94.13
1000	R	76.23	72.13	77.89	74.40	85.43	84.30
2000	R	78.54	74.33	80.99	77.50	90.09	90.70
4000	R	81.09	77.43	82.59	78.63	89.04	86.73
500	L	82.30	78.57	83.74	78.63	91.06	88.77
1000	L	90.24	88.20	90.79	89.90	92.66	90.03
2000	L	83.06	80.13	85.74	83.17	93.30	91.10
4000	L	84.59	83.70	85.94	83.73	93.49	91.30

For a frequency of 500 Hz for the right ear, the classification accuracy obtained from the comparison result indicates that grid search method could to choose the most appropriate σ and C parameters among a big set of parameters, which allowed RBF kernel SVM algorithm to obtain the highest training and testing classification accuracy of 96.40% and 94.13% respectively. For a frequency of 4000 Hz for the left ear, RBF kernel SVM classifier has the maximum training and testing classification accuracy of 93.49 % and 91.30% respectively.

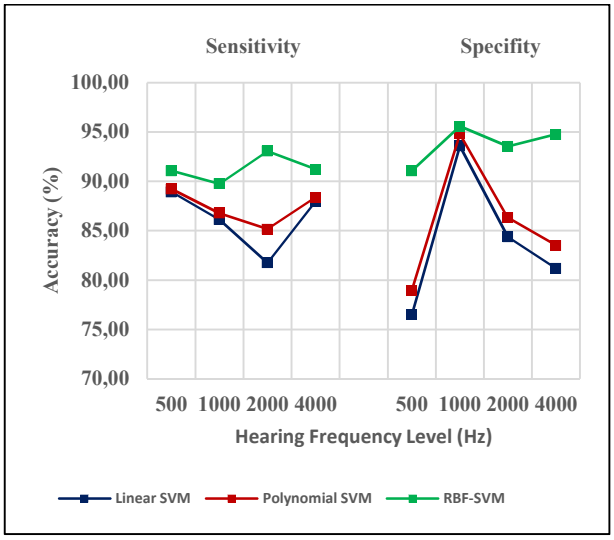

Fig. 5: Sensitivity and specificity of linear kernel SVM classifier, polynomial kernel SVM classifier and RBF kernel SVM classifier (left ear).

From Fig. 5, for a frequency of 2000 Hz for the left ear, RBF kernel SVM classifier yields the sensitivity of 93.06%. For a frequency of 500 Hz for the left ear, linear kernel SVM classifier and polynomial kernel SVM classifier yield the sensitivity of 88.92% and 89.21% respectively. It is also noticed that for the a frequency of 1000 Hz for the left ear, RBF kernel SVM classifier has the specificity of 95.57% while linear kernel SVM classifier and polynomial kernel SVM classifier have the sensitivity of 93.57% and 94.8% respectively.

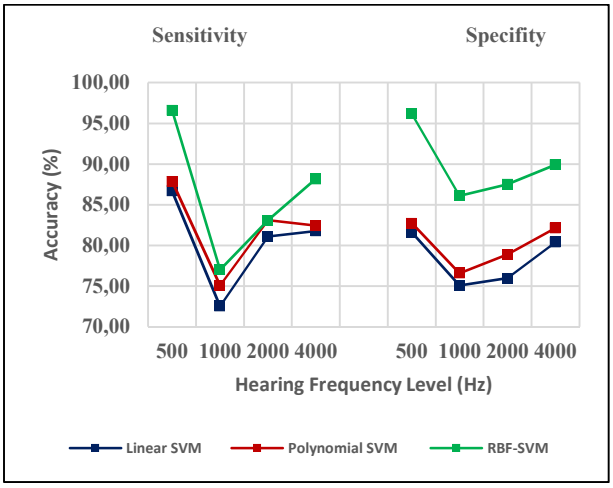

Fig. 6: Sensitivity and specificity of linear kernel SVM classifier, polynomial kernel SVM classifier and RBF kernel SVM classifier (right ear).

From Fig. 6, for a frequency of 500 Hz for the right ear, RBF kernel SVM classifier has the sensitivity and specificity of 96.63% and 96.17% respectively, while linear kernel SVM classifier has the sensitivity and the specificity of 86.69% and 81.63% respectively and polynomial kernel SVM classifier has the sensitivity and specificity of 87.89% and 82.75% respectively.

The results show that the SVM with the RBF kernel is robust, very flexible and can adapt to complex decision limits. The RBF kernel has a greater ability to map data to a high-dimensional space compared to other kernel functions. The RBF kernel is the most suitable choice to be used on datasets with different characteristics than the linear kernel and the polynomial kernel.

The experimental results show that Grid Search method is an effective tool to search for more solutions and find the best of them.

IV. CONCLUSION

In this paper, we have developed three SVM classifier models including RBF kernel, polynomial and linear functions to distinguish the normal hearing group and the abnormal hearing group using FD features obtained from the subject's recorded AEP signals applying DFA method. The AEP signal is stimulated at four distinct frequency in the right and left ear at a fixed sound intensity level. Grid search is selected to optimize the kernel parameters.
Through the results obtained, it can be considered that the FD extracted from the AEP signals is an appropriate parameter for estimating the threshold of perception for hearing. It is also considered that DFA method more efficient and faster to find this parameter. From the results obtained in this experiment, for hearing impaired persons, the values of the FD are relatively high compared to normal hearing ones due to the longer response time to the stimulus.

Our results indicate that the grid search was able to find near optimal parameter combination within given ranges. RBF kernel SVM classifier is promising; it is able to obtain a high training as well as testing classification accuracy and to achieve considerably higher performance compared to linear SVM classifier and polynomial SVM classifier.

REFERENCES

[1] D.W.Swanepoel, K.C.De Sousa, C.Smits, D.R.Moore, "Mobile applications to detect hearing impairment: opportunities and challenges", Bulletin of the World Health Organization., vol.97, no. 10, pp. 717-718 Sep, 2019, DOI:10.2471/BLT.18.227728.
[2] K. Neumann, S. Chadha, G. Tavartkiladze, X. Bu, K.R. White, "Newborn and Infant Hearing Screening Facing Globally Growing Numbers of People Suffering from Disabling Hearing Loss ", Int. J. Neonatal Screen., vol.5, no.7, Jan, 2019, DOI:10.3390/ijns5010007.
[3] A.Ballas, P. Katrakazas, "Ωto_abR: A Web Application for the Visualization and Analysis of Click-Evoked Auditory Brainstem Responses", Digital. vol. 1, no. 4, pp. 188-197, Oct, 2021, DOI:10.3390/digital1040014.
[4] S.OUDJEMIA, "Analyse des signaux biomédicaux par des approches multifractales et entropiques : Application à la variabilité du rythme cardiaque fœtal", Ph.D. dissertation, Dept. Elec, Mouloud Mammeri Univ., Tizi-Ouzou, Algeria, 2015.
[5] Z.M.H. Almurad, Didier Delignières, "Evenly spacing in Detrended Fluctuation Analysis", Physica A., vol.451, pp. 63-69 Jun, 2016.
[6] Mark Höll, KKiyono, Holger Kantz, "Theoreticalfoundation of detrending methodsfor fluctuation analysis such as detrended fluctuation analysis and detrending moving average", PRE journal, vol. 99, no. 3, pp. 1-20 Mar, 2019, DOI: 10.1103/PhysRevE.99.033305.
[7] S.Das, S.Dalai, S.Chakravorti, "Diagnosis of Power Quality Events based on Detrended Fluctuation Analysis", IEEE Transactions on Industrial Electronics., vol. 65, no. 9, pp. 7322-7331, Jan, 2018.
[8] IvanSeleznov, IZyma, KKiyono, STukaev, APopov, MChernykh, OShpenkov," Detrended FluctuationCoherence, and Spectral Power Analysis of Activation Rearrangement in EEG Dynamics During Cognitive Workload", Front. Hum. Neurosci journal. vol.13, Aug, 2019.
[9] P. Jing, Y. Bo, Z. Xu, L. Hong, "Correlation Properties Applied Detrended Fluctuation Analysis Method for Cue-induced EEG in Drug Dependence", IEEE International Conference on Computer Science and Electronics Engineering, Hangzhou, China, 23-25 Mar 2012, pp.446-450, DOI:10.1109/ICCSEE.2012.189.
[10] M.P. Paulraj, K. Subramaniam, S. Yaccob, A.H. Adom, C.R Hema, "Auditory Evoked Potential Based Detection of Hearing Loss: A prototype System", 2014 IEEE 5th Control and System Graduate Research Colloquium. (2014) Shah Alam, Malaysia, Aug, 2014. pp. 164-169, DOI: 10.1109/ICSGRC.2014.6908715.
[11] A. Gasmi, H. Zouari, A. Masse, D. Ducrot, "Potential of the Support Vector Machine (SVMs) for clay and calcium carbonate content classification from hyperspectral remote sensing", International Journal of Innovation and Applied Studies., vol.13, no. 3, pp. 497–506, Nov, 2015.
[12] M. M. Manjurul Islam, J.Kim, Sheraz A. Khan, J.M, Kim, "Reliable bearing fault diagnosis using Bayesian inference-based multi-class support vector machines ", J. Acoust. Soc.Am., vol.141, no.2, Feb, 2017, DOI: 10.1121/1.4976038.
[13] K.Y.Bae, H.S. Jang, D. K. Sung, " Hourly Solar Irradiance Prediction Based on Support Vector Machine and Its Error Analysis", IEEE Transactions on Power Systems., vol.32, no.2, pp. 935- 945, Mar, 2017.
[14] Z. Nazari, D. Kang, "Density Based Support Vector Machines for Classification", International Journal of Advanced Research in Artificial Intelligence., vol.4, no.4, pp. 69-76, Apr, 2015, DOI:10.14569/IJARAI.2015.040411.
[15] C. Savas, F.Dovis, "The Impact of Different Kernel Functions on the Performance of Scintillation Detection Based on Support Vector Machines", Sensors. vol.19, no.23, Nov, 2019, DOI:10.3390/s19235219.
[16] L. Huang et al., "Detection of Fusarium Head Blight in Wheat Ears Using Continuous Wavelet Analysis and PSO-SVM", Agriculture, 2021 - mdpi.com, vol.11, no. 998, Oct, 2021, DOI : 10.3390/agriculture11100998.
[17] M. Djemai, M. Guerti, "A genetic algorithm-based support vector machine model for detection of hearing thresholds", Australian Journal of Electrical and Electronics Engineering, vol.19, no. 2, pp. 194–201, Jan, 2022, DOI : 10.1080/1448837X.2021.2023080.
[18] E. Elgeldawi, A. Sayed, A.R. Galal, A.M. Zaki, "Hyperparameter Tuning for Machine Learning Algorithms Used for Arabic Sentiment Analysis", Informatics, 2021 - mdpi.com, vol.8, no. 79, Nov, 2021, DOI :10.3390/informatics8040079.
[19] X. Wang, F. Zhang, H. Kung, V. C. Johnson, A. Latif, "Extracting soil salinization information with a fractional-order filtering algorithm and grid-search support vector machine (GS-SVM) model ", International Journal of Remote Sensing., vol.41, no.3, pp. 953-973, Aug, 2019, DOI: 10.1080/01431161.2019.1654142.
[20] F. Budiman, "SVM-RBF Parameters Testing Optimization Using Cross Validation and Grid Search to Improve Multiclass Classification ", Scientific Visualization., vol.11, no.1, pp. 80- 90, Jan, 2019, DOI: 10.26583/sv.11.1.07.
[21] R.M. Adnan et al., " Comparison of LSSVR, M5RT, NF-GP, and NF-SC Models for Predictions of Hourly Wind Speed and Wind Power Based

on Cross-Validation", Energies., vol.12, no.2, Jan, 2019, DOI: 10.3390/en12020329.

Mohamed Djemai received the Engineer Diploma degree from Ziane Achour University, Djelfa, Algeria in 2006 and the Magister degree in Electronic engineering from Ecole Nationale Polytechnique, Algiers, Algeria, in 2011. He is currently a teacher at Ziane Achor university, Djelfa, Algeria. His research fields are speech processing, automatic classification and feature selection.

Mhania Guerti received her MSc in Language and linguistic communication sciences from the ILP Algiers, Algeria in collaboration with the CNET Lannion (France), in 1984, and Ph.D. from ICPINPG, Grenoble, France, in 1993. She is an Ex-Full Professor in the Department of Electronics at Ecole Nationale Polytechnique. Her research fields are speech processing, acoustics and audiovisual systems.

Effect of Surface Preparation on Mechanical Properties of Anodized A6061 in Sulfuric Acid Bath

Amane Sahli, Oussama Djema, Mabrouk Bouabdallah, and Djaffar Saidi

Abstract− The aims of this work are to examine the effect of the pickling conditions on the mechanical behavior of anodized A6061. Pickling was explored at 60°C for 30, 60, 90 and 120 second. The growth rate of the anodic layer, surface roughness, microhardness and tensile strength of anodized samples treated by alkaline pickling were investigated. The experimental results showed that the thickness of the anodic layer is directly related to the roughness of the substrate. In addition an important growth in thickness layer affects slightly the mechanical proprieties.

***Keywords*− A6061 aluminum alloy, Sulfuric anodizing, Microstructure, Surface morphology, Surface roughness, Microhardness, Tensile strength.**

I. INTRODUCTION

The aluminum alloy A6061 is widely used in the aircraft, automotive industries and nuclear industry, because of their low density, good mechanical properties and easily manufactured [1]. However, due to his heterogeneous microstructure the A6061 is prone to localized corrosion, a drawback that limits its technical applications especially in an aggressive environment [2-4]. Currently, many researchers have investigated anodizing process to improve the surface performance and corrosion resistance of aluminum alloys [5-7].

Anodizing is an electrochemical process to produce an aluminum oxide film Al2O3 with a thickness that can reach 500 times the oxide layer naturally formed [8-10]. Aluminum anodization can be processed in an acid or alkaline bath [11]. The sulfuric acid anodizing is the most commonly bath used in the industry due to lower cost and rapid action. Researchers [12] focused their work on the influence of the current density, concentration, compositions, temperature of electrolyte and anodization time on the quality and thickness of the anodic film. T.C. Cheng et al [13] studied the effect of the sulfuric acid concentration, and anodizing voltage. They demonstrated that 0.3 M sulfuric acid bath and the range of 30 - 50 V are the optimum conditions to anodizing of A6061. C.C. Lee et al [14] prepared AA6061 oxide films in 10 % H2SO4 electrolyte solutions for 20 min at 0°C and 22°C. The results showed that anodic oxide film with a higher hardness can be obtained at a lower anodization temperature (0 °C) than at room temperature.

Manuscript received May 11, 2022; revised July 27, 2022.

A. Sahli and D. Saidi are with the nuclear research center of Draria, Algeria (e-mail: sahliamane@gmail.com)
O. Djema is with the research center in semiconductors technology for energetics (CRTSE), Algiers, Algeria (e-mail: oussama.djema16@gmail.com)
M. Bouabdallah is with Ecole Nationale Polytechnique, Algeria (e-mail: mabrouk.bouabdallah@g.enp.edu.dz)

Digital Object Identifier (DOI): 10.53907/enpesj.v2i1.93

In this aluminum anodizing experiment, the A6061 sheets anodized with sulfuric acid were obtained using different conditions of pickling. The surface morphology, surface roughness and the mechanical properties of the samples, including their microhardness, tensile strength and elongation were analyzed in order to observe the influence of surface preparation against the mechanical properties of anodized A6061.

II. MATERIALS AND METHODS

II.1. MATERIALS

The material investigated in this study was aluminum alloy 6061-T6 with the composition as given in Table 1. The tested samples were machined according to the tensile test specimen before anodizing treatment.

Table. I
Chemical composition of the A6061 (wt.%)

Element	Al	Mg	Si	Cr	Mn	Ti	Cu	Zn	Fe
Composition	Bal	1.06	0.64	0.24	0.77	0.06	0.2	0.01	0.04

II.2. SAMPLE PREPARATION

In order to investigate the effect of anodizing process on the mechanical behavior of A6061 alloy, a number of specimens were treated by means of sulfuric acid anodizing. Before the anodizing process, the samples were subjected to degreasing using Acetone and pickling sequences as defined in Table 2 in order to produce a chemically clean and decontaminated surface. According to the surface treatment applied to the samples, they were divided in different groups as summarized in Table. II.

Table. II
Surface pretreatment conditions

Groups	Pickling	Neutralization
G1	15 g / l of NaOH at 60°C for 30 s	910 g/l HNO_3 for 2 min
G2	15 g / l of NaOH at 60°C for 60 s	910 g/l HNO_3 for 2 min
G3	15 g / l of NaOH at 60°C for 90 s	910 g/l HNO_3 for 2 min
G4	15 g / l of NaOH at 60°C for 120 s	910 g/l HNO_3 for 2 min
G5	30 g / l of NaOH at 60°C for 30 s	910 g/l HNO_3 for 2 min
G6	30 g / l of NaOH at 60°C for 60 s	910 g/l HNO_3 for 2 min
G7	30 g / l of NaOH at 60°C for 90 s	910 g/l HNO_3 for 2 min
G8	30 g / l of NaOH at 60°C for 120 s	910 g/l HNO_3 for 2 min
G9	45 g / l of NaOH at 60°C for 30 s	910 g/l HNO_3 for 2 min
G10	45 g / l of NaOH at 60°C for 60 s	910 g/l HNO_3 for 2 min
G11	45 g / l of NaOH at 60°C for 90 s	910 g/l HNO_3 for 2 min
G12	45 g / l of NaOH at 60°C for 120 s	910 g/l HNO_3 for 2 min

Subsequently, the specimens without a natural oxide film were placed in a prepared sulfuric acid solution with a concentration of 20% under constant voltage at 20 V for 30 min. The aluminum sheet (anode) and the lead plate (cathode) were connected to the DC power supply. A schematic of the anodizing process is presented in Fig. 1.

All the specimens were anodized at 20 °C thanks to a thermostatically controlled electrochemical cell (±2 °C) and a continuous agitation to prevent local violent reactions and to keep initial electrolyte concentration and temperature.

After the anodizing process, the samples were immediately rinsed with deionized water to avoid acid attack and then sealed in boiling water at 97 °C for 30 min.

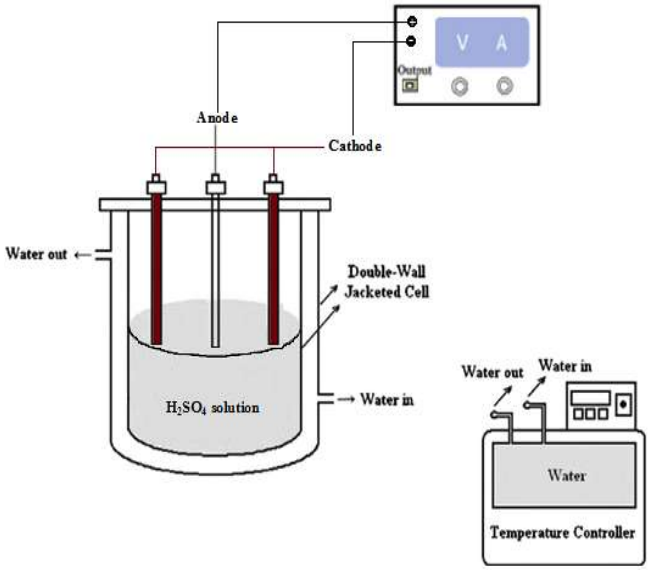

Fig. 1: Anodizing process

II.3. CHARACTERIZATION

II.3.1. METALLOGRAPHIC CHARACTERIZATION

The specimens were prepared using fine grinding, polishing and etched with Keller's reagent. The surface morphology and the thickness of the anodic films were examined using an optical microscope (Carl Zeiss-Axioteck 100).

II.3.2. MECHANICAL TESTING

Tensile strength testing is carried out using a MTS Criterion Model 45 X 100 KN machine with a strain rate of 1.2mm/min at room temperature.

Test specimens (Fig. 2) were machined according to the standards and specifications of ASTM E8 [15]

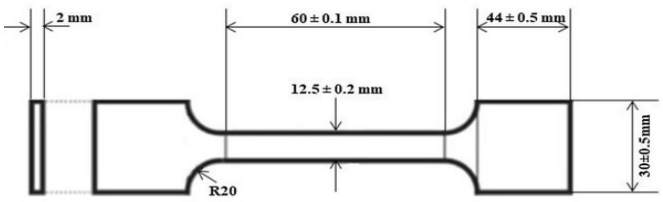

Fig. 2: Shape and dimension of tensile strength testing specimen

Vickers microhardness of the anodic layer was measured from the surface of the samples under a load of 0.5 N for 20 s. Each data point represents the mean of three values at least.

Surface roughness (Ra) was measured using RUGOSURF 10 G from three different regions of each sample with an evaluation length of 10 mm.

III. RESULTS AND DISCUSSION

III.1 Surface Morphology

Fig. 3 shows the relationship between the roughness of the pickled samples and the pickling parameters. It appears that samples pickled with 45g/l during 120s has a higher roughness compared to the others concentrations bath for the same time pickling.

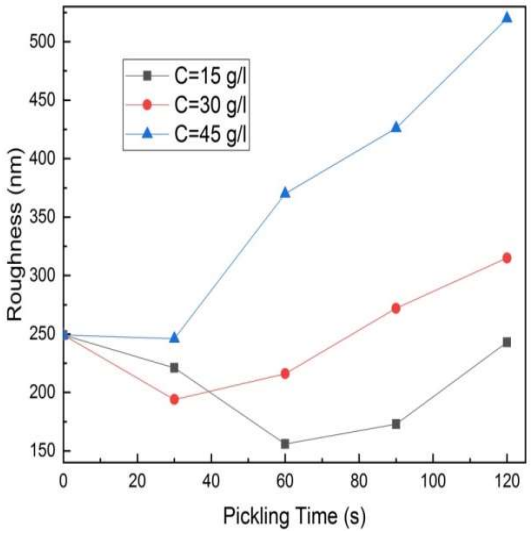

Fig. 3: Roughness of the substrate as function of pickling time and bath concentration

The effect of pickling treatment on A6061 substrate, slightly roughen the surface. Prolong the immersion time in the sodium hydroxide bath had slightly increased the surface roughness as shown in Fig.3. A long exposure to the caustic soda at high concentrations accelerates significantly the pickling process. This conclusion has been proven by other researchers [16].

To show the changes induced by the pickling treatment in the surface morphology of the substrate, optical microstructure images of A6061 as received and after pickling have been presented in Fig.4

The Fig.4 (a) shows the surface morphology of A6061before pickling. Figures 4 (b) and (c) reveal inhomogeneous morphologies which have the appearance of an eroded surface with random distribution of several small and large pits.

The curve of Fig. 5 shows the effect of the roughness of the substrate on the roughness of the anodic layer. It is clear that the roughness of the anodic layer increase with increasing the roughness of the substrate. This was due to the fact that on a rough surface, the localized current density is high; therefore, the electric field-assisted dissolution of the oxide is also high [17]. This could leads to the formation of a more porous anodic layer leading to high rough anodic layer. This result is supported by P. F. A. Bijlmer's results [18] which confirm that the anodic layer reproduce the roughness of the substrate in the case of anodizing in sulphuric acid solutions.

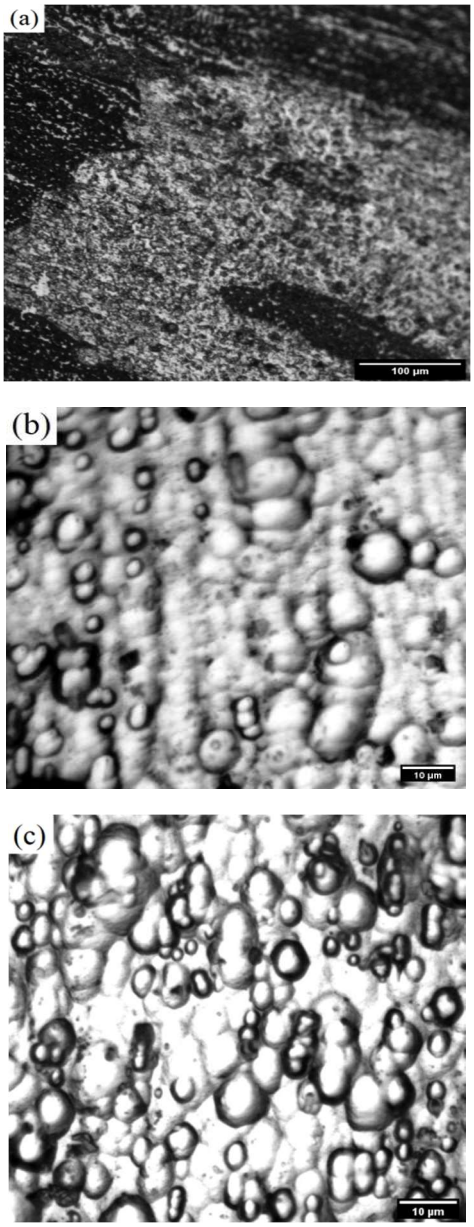

Fig. 4: Surface morphology of A6061-T6: (a) as received, (b) and (c) after pickling with 45g/l of NaOH during 60s and 120s respectively.

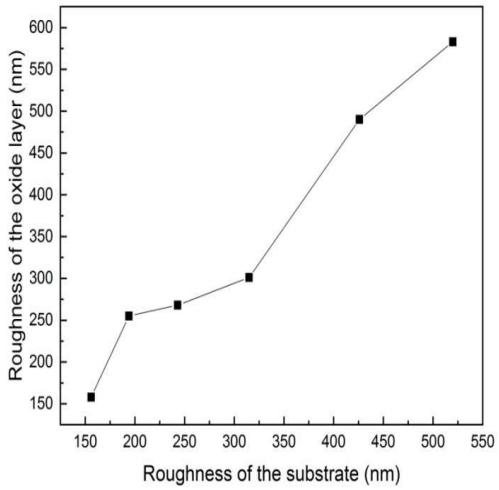

Fig. 5: Roughness of the anodic layer as function of substrate roughness

III.2 ANODIC LAYER THICKNESS

The thickness of the anodized layer depends on the roughness of A6061 after pickling .This dependences is presented in Fig. 6. The thickness of the anodic layer did change significantly with the substrate roughness. A significant increase in the anodic layer thickness until a roughness of 310 nm, and then a reduction has been noticed.

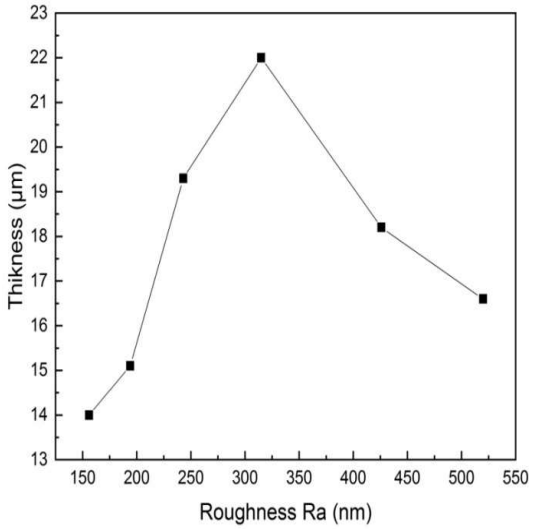

Fig. 6: Thickness of the anodic layer as function of substrate roughness

Fig.7 (a), (b) and (c) show an example for the anodic layer thickness measurement, of anodized A6061 formed on aluminum substrates having Ra value of 187, 310 and 521 um, respectively.

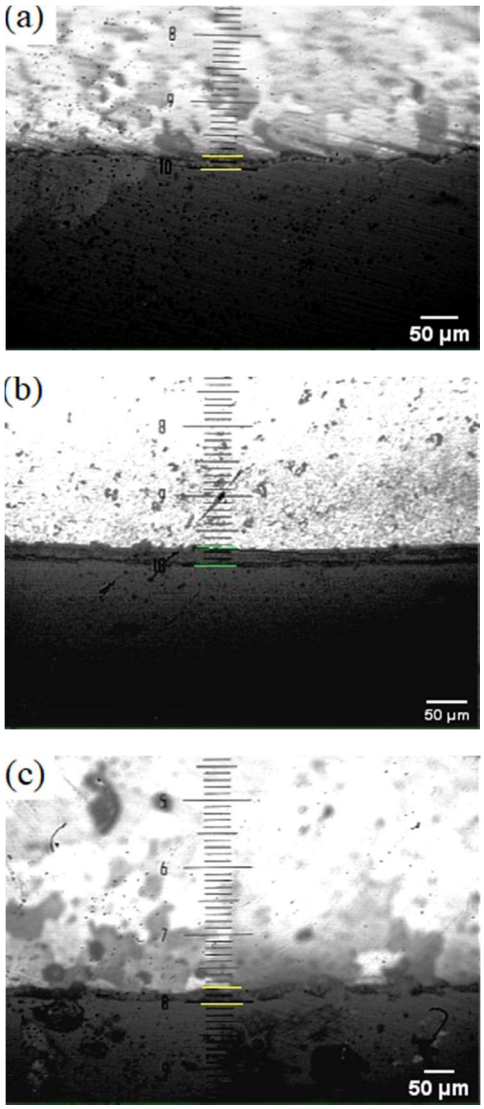

Fig. 7: Cross-sectional optical micrographs of anodized A6061 alloy after different surface preparation conditions: (a) pickling with 15g/l of NaOH during 60s, (b) pickling with 30g/l of NaOH during 120s and (c) pickling with 45g/l of NaOH during 120s

III.3 MICROHARDNESS EVOLUTION

The evolution of the microhardness as a function of the substrate roughness is represented in Fig. 8. In these analyses, the model of Jonsson and Hogmark [21] has been used to measure the microhardness of the anodic layer. This model uses a geometrical approach to combine the hardness of the anodic layer and of the substrate according to the area mixture model.

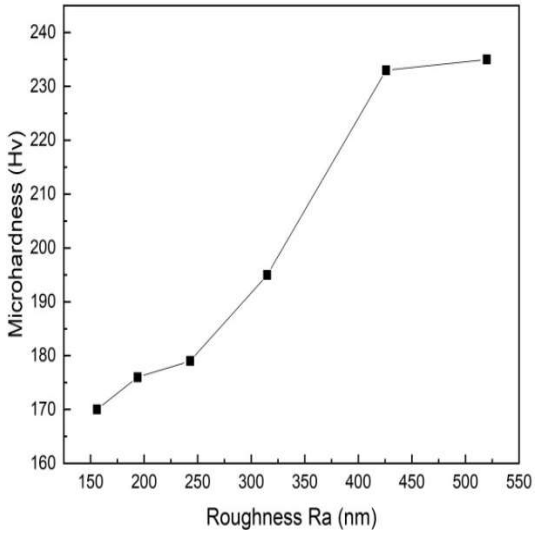

Fig. 8: Microhardness of the anodic layer as function of the substrate roughness

From Fig.8, it can be observed that the microhardness of the anodic layer increased significantly with increasing roughness of the substrate. The measured average microhardness values were in the range of 170 and 240 Hv.

The low microhardness of the anodic layer was attributed to the low O/Al ratio of the layer [22]. As there is lower oxygen content in the sample the film is more metallic and soft. According to R.K. Choudhary et al [19], the O/Al ratio of the anodic layer was found to be relatively high for the layer formed on a more rough aluminum surface and also resulted in increased hardness.

III.4 TENSILE PROPERTIES

Fig.9 shows the changes in the mechanical properties of A6061 alloy before and after anodization, as a function of the thickness of the anodic layer.

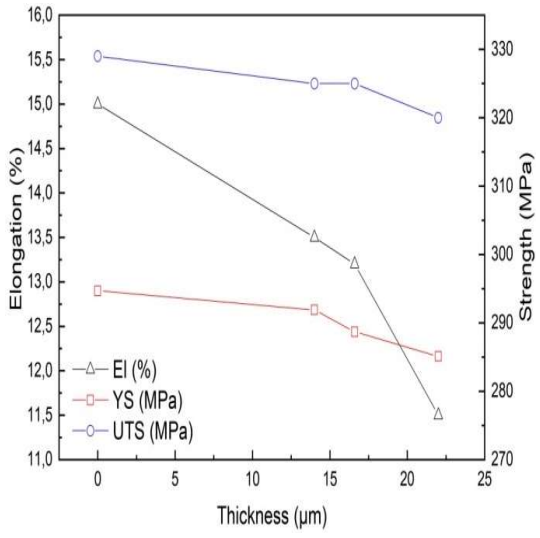

Fig. 9: Mechanical properties as a function of thickness of anodic layer

IV. CONCLUSION

In this paper, the influence of surface preparation on mechanical properties of A6061 anodized in sulfuric acid bath was investigated, and compared with those of A6061 without anodization. The results obtained were summarized below:

(1) - The roughness of the substrate A6061 increases with increasing time of pickling, and/or pickling bath concentration.

(2) - The thickness of the anodic layer and its roughness are directly related to the roughness of the substrate

(3) - The surface microhardness of the anodized A6061 is improved by increasing the thickness of the anodic layer

(4) - A slight decrease in yield strength, ultimate tensile strength and elongation compared to non-anodized A6061 alloy.

(5) - Mechanical proprieties of anodized A6061 decrease slightly with increasing anodic layer thickness.

ACKNOWLEDGMENT

The authors wish to thank Pr. M. Bouaziz from ENP, Algiers, Algeria and Mrs. S. Brazane from CRTI, Algiers, Algeria for their help during the characterization of the investigated alloy.

REFERENCES

[1] A. Sahli, M. Bouaballah, D. Saidi, S. Grine, S. Allaoua, O. Djema, B. Rahal, M. Khalfa, K. Lazazi and R. Zekri, "Effect of an addition of vanadium on the mechanical properties of the A6061 alloy deformed by accumulative roll bonding," J. Mater. Eng. Perform. , vol. 30, no 10, p. 7510-7522.May, 2021, DOI: https://doi.org/10.1007/s11665-021-05882-2

[2] P. Blanchard, C. Colombie, V. Pellerin, S. Fayeulle and L. Vincent ,"Material effects in fretting wear: application to iron, titanium, and aluminum alloys," Metall. Trans. A, vol. 22, no 7, p. 1535-1544. July,1991, DOI: https://doi.org/10.1007/BF02667367

[3] D. G. Piercey and T. M. Klapötke, "Nanoscale aluminum-metal oxide (thermite) reactions for application in energetic materials," Cent. Eur. J. Energ. Mater., vol. 7, no 2, p. 115-129. July, 2010.

[4] J.A. Puszynski, "Reactivity of Nanosize Aluminum with Metal Oxides and Water Vapor," MRS Online Proc. Libr., vol. 800, p. AA6.4. 2003, DOI: 10.1557/PROC-800-AA6.4.

[5] S. Lee, Kim, Y. Kim, U. Jung and W. Chung, "Effect of aluminum anodizing in phosphoric acid electrolyte on adhesion strength and thermal performance," Met. Mater. Int., vol. 22, no 1, p. 20-25. January, 2016,DOI: https://doi.org/10.1007/s12540-015-5426-2

[6] I. Ali, M. M. Quazi, E. Zalnezhad, A. A. D. Sarhan, N. L. Sukiman and M. Ishak, "Hard anodizing of aerospace AA7075-T6 aluminum alloy for improving surface properties," Trans. Indian Inst. Met., vol. 72, no 10, p. 2773-2781. July, 2019, DOI: https://doi.org/10.1007/s12666-019-01754-5

[7] P. H. Setyarini, R. Soenoko, A. Suprapto, Y.S. Irawan and Purnomo," Corrosion characterization of anodized AA 6061," MM Science Journal., p. 2415-2420. June, 2018,DOI: DOI: 10.17973/MMSJ.2018_06_201803

[8] T. Ito, Y. Matsuda, T. Jinba, N. Asai, T.Shimizu and S. Shingubara,"Fabrication and characterization of nano porous lattice biosensor using anodic aluminum oxide substrate," Jpn. J. Appl. Phys., vol. 56, no 6S1, p. 06GG02. May, 2017, DOI: https://doi.org/10.7567/JJAP.56.06GG02

[9] Ö. Ö. Çapraz, P. Shrotriya, P. Skeldon, G. E.Thompson, K. R. Hebert, " Role of oxide stress in the initial growth of self-organized porous aluminum oxide," Electrochim. Acta., vol. 167, p. 404-411. June, 2015,

[10] J. Lee, D. Kim, C. Choi and W. Chung, "Nanoporous anodic alumina oxide layer and its sealing for the enhancement of radiative heat dissipation of aluminum alloy," Nano energy, vol. 31, p. 504-513. January, 2017,DOI: https://doi.org/10.1016/j.nanoen.2016.12.007

[11] C. E. Michelson, "Process for coloring an anodized aluminum sheet," U.S. Patent No 3,218,243, 16 nov. 1965.

[12] C. Alexander and G. L. Hager , "Method of multi-coloring anodized aluminum," U.S. Patent No 3,099,610, 30 juill. 1963.

[13] T. C. Cheng and C. C. Chou, "The electrical and mechanical properties of porous anodic 6061-T6 aluminum alloy oxide film," J. Nanomater.,

2015, vol 16, no 16, p.141. January, 2015, DOI: https://doi.org/10.1155/2015/371405
[14] C. C. Lee, C. W. Chen, LIN, J. S. Lin , S. H. Wang, C. S. Lee, C. C. Chen, Y. H. Lin and C. Y. Chen , "Effect of Anodization Treatment on the Thickness, Hardness, and Microstructural Characterization of Anodic Aluminum Oxide Film on AA 6061 and Critical Patent Analysis," J. Mater. Eng. Perform., vol. 31, no 1, p. 667-68. September, 2022, DOI: https://doi.org/10.1007/s11665-021-06205-1
[15] Test Methods for Tension Testing of Metallic Materials, ASTM International E8M-04, 2004.
[16] M. Keijzer, "Pickling, an excellent surface treatment for aluminium," Vecom , Hamburg, Germany, Tech. Rep .17 (2004), Sep. 2004.
[17] J. Yang, H. Huang, Q. Lin, L. Lu, X. Chen, L. Yang, X. Zhu, Z. Fan, Y. Song, and D. Li, "Morphology Defects Guided Pore Initiation During the Formation of Porous Anodic Alumina," ACS Appl. Mater. Interfaces., vol. 6, no. 4, p. 2285–2291. January, 2014, DOI: https://doi.org/10.1021/am405294x
[18] P. F. A. Bijlmer, "Influence of chemical pretreatments on surface morphology and bondability of aluminium," J. Adhes., vol. 5, no 4, p. 319-331. June, 1973, DOI: https://doi.org/10.1080/00218467308072233
[19] R. K. Choudhary, K. P. Sreeshma and P. Mishra , "Effect of Surface Roughness of an Electropolished Aluminum Substrate on the Thickness, Morphology, and Hardness of Aluminum Oxide Coatings Formed During Anodization in Oxalic Acid," J. Mater. Eng. Perform., vol. 26, no 7, p. 3614-3620. June, 2017, DOI: https://doi.org/10.1007/s11665-017-2798-0
[20] B. Wielage, D. Nickel, G. Alisch, H. Podlesak and Th .Lampke, "Effects of pre-treatment on the growth rate and morphology of hard anodic films on aluminium (EN AW-6082)," Surf. Coat. Technol., vol. 202, no 3, p. 569-576. , Dec, 2007, DOI: https://doi.org/10.1016/j.surfcoat.2007.06.052
[21] B. Jönsson and S. Hogmark, "Hardness measurements of thin films," Thin solid films., vol. 114, no 3, p. 257-269. April, 1984, DOI: https://doi.org/10.1016/0040-6090(84)90123-8
[22] A. Aryasomayajula, N. X. Randall, M. H. Gordon and D. Bhat, "Tribological and mechanical properties of physical vapor deposited alpha alumina thin film coating," Thin Solid Films., vol. 517, no 2, p. 819-823. Nov, 2008, DOI: https://doi.org/10.1016/j.tsf.2008.06.019

Amane Sahli is researcher at the nuclear research center of Draria, Algeria, she obtained his mechanical engineering diploma from the university of Saad Dahleb, Blida and Magister's degree in mechanicas of materials from the Polytechnic Military School, Algiers. Currently she is Ph.D student in the Ecole Nationale Polytechnique, Algiers.

Oussama Djema is researcher at research center in semiconductors technology for energetics (CRTSE), Algiers, Algeria. He received the degree of Engineer, Master and Ph.D. in Metallurgy from Ecole Nationale Polytechnique.

Mabrouk Bouabdallah is a professor and research director at Ecole Nationale Polytechnique, Algiers.

Djaffar Saidi is research director at the nuclear research center of Draria, Algeria.

Energy Balance Of Third Generation Bioethanol

Amina Allouache, Majda Aziza, Toudert Ahmed Zaid, and Mohammed Amouri

Abstract− Global greenhouse gas emissions are constantly increasing, despite the partial replacement of fossil fuels by renewable energies. The transport sector is responsible for almost 24% of direct CO_2 emissions from the combustion of fossil fuels, generating greenhouse gas emissions, highlighting the need for a greater focus of international policies to encourage the production and the use of biofuels. Bioethanol is the most consumed biofuel in the world; it is produced by fermentation from materials rich in sugar (glucose, starch, cellulose). However, the controversy around the use of first and second generation have forced the transition to the third generation based on marine and freshwater algae; the latter have the advantage of being abundant, even invasive, easy to cultivate with good energy potential. This study proposes a life cycle analysis (LCA) of bioethanol production from the macro algae Ulva Lactuca, it was carried out after the introduction of several data into the SimPro8.1 software (e.g. quantity of water, consumed electricity, used chemicals) using the Impact 2002+ methodology. The results show a positive energy balance reflecting high-energy efficiency since the system produces about 1.44 times the energy consumed.

***Keywords*− Bioethanol, 3rd Generation, Macro algae, LCA, Energy balance.**

NOMENCLATURE

LCA	Life Cycle Assessment
kwh	kilowatt hour
CDER	Centre de Développement des Energies Renouvelables

I. INTRODUCTION

After first-generation biofuels derived from food plant materials, and second-generation biofuels produced from lignocellulosic biomass, a third generation is now arousing great enthusiasm. These are biofuels from algae, also called "Algofuels". Algae represent a major reservoir of energy, they have a higher carbon fixation rate than that of terrestrial plants (17.5 t/ha/year against 5 to 10 t/ha/year for sugar cane) and their production price is lower than that of agrarian crops [2]. Algae represent a wide variety of species living by photosynthesis in diverse environments. They can be autotrophic or heterotrophic. Autotrophs exploit sunlight and fix atmospheric CO_2 that is then assimilated in the form of carbohydrates.

Manuscript received May 29, 2022; July 27, 2022

A. Allouache is with the Centre De Développement Des Energies Renouvelables, Bioenergies et Environnement division (Algiers) and with Ecole Nationale Polytechnique, Département de Génie Chimique, Laboratoire de Valorisation des Energies Fossiles, Algeria (e-mail: a.allouache@cder.dz)

A. Z. Toudert is with Ecole Nationale Polytechnique, Département de Génie Chimique, Laboratoire de Valorisation des Energies Fossiles. (e-mail: toudert.ahmed-zaid@g.enp.edu.dz)

M. Aziza and M. Amouri are with the Centre De Developpement Des Energies Renouvelables, Bioenergies et Environnement division (e-mail: m.aziza@cder.dz, m.amouri@cder.dz)

Digital Object Identifier (DOI): 10.53907/enpesj.v2i1.97

Heterotrophs are able to use small organic molecules present in the environment, transform them and store them in the form of fat or protein. Thus algae can produce carbohydrates, lipids and proteins quickly, which can be processed to generate biofuels.

Based on their morphology and size, algae are grouped into two categories - microalgae and macro algae -. As their name suggests, microalgae are microscopic photosynthetic organisms, many of which are single-celled. On the contrary, macro algae are composed of several cells whose structure resembles the roots, stems and leaves of higher plants. [2]

Algofuels can be made from so-called chlorophyceae algae such as *chlamydomonas*, *closterium,* or diatom algae such as *phaeodactylum, melosira* or even macroalgae such as sea lettuce. While the first efforts to produce biofuels from algae were focused on biodiesel as an end product, researchers have begun to explore the production of ethanol from algae. The large investments made in the production of ethanol and the technological innovations as a result could make the production of ethanol from the starch and cellulose of algae a viable alternative via different processes. [1]

Indeed, several major features make algae an excellent candidate for the production of bioethanol. Algae have a high conversion efficiency and are able to synthesize and accumulate large amounts of carbohydrates (14 times more than terrestrial plants); they can also tolerate and use noticeably high levels of CO_2. Therefore, they can use the CO_2 emitted during ethanol production thereby reducing greenhouse gas emissions. In addition, algae are rich in cellulose and poor in lignin or hemicellulose, the main barriers to the production of lignocellulosic ethanol. Furthermore, algal cells can be harvested in a short period compared to terrestrial plant and can therefore meet the increasing demands of ethanol production.

Algae growth is simple; it can reach high densities, and uses light, carbon dioxide, and other inorganic matter efficiently, so it can produce 6,000 gallons of ethanol a year when corn alone

produces 400 gallons of ethanol per year [3]. Algae can be easily grown in different aquatic environments such as sewage, salt or municipal water, which would allow for sustainable bioethanol production, as it decreases competition with food crops, which need fresh water for irrigation. In addition, algae can provide sustainable bioremediation of wastewater through the use of polluting molecules as nutrients for their growth such as nitrogen and phosphorus. In addition to the production of bioethanol, algae provide valuable co-products such as protein-rich waste that can be used as animal feed [4].

Many macro alga especies are known to be good candidates for bioethanol production, such as brown algae: *Laminaria*, *Saccorhiza*, *Alaria*, which store laminarin, mannitol, and red algae such as *Gelidium amansii*. The latter store cellulose, glucan and galactan, green algae: *ulva lactuca* and *rigida* characterised by interesting rates in cellulose and the absolute absence or near absence of lignin, which makes enzymatic hydrolysis easier [4].

Life cycle analysis (LCA) is an environmental assessment method that quantifies the impacts of a product (whether it is a good, a service, or even a process) over its entire life cycle, from the extraction of the raw materials that make it up to its disposal at the end of its life, passing through the distribution and use phases.

LCA, a standardized and recognized tool, is the most successful method in terms of overall assessment, it results from the interpretation of the quantified data balance (quantity of water, energy consumed, etc.) linked to each stage of the production cycle (acquisition of raw materials, transport, production, consumption, recycling or disposal). This data will be used to calculate potential environmental impacts [5].

With the aim of quantifying the impacts and avoiding possible problems related to energy consumption or significant greenhouse gas emissions, the application of life cycle analysis is therefore recommended [6].

These analyzes take into account the impacts of the entire production cycle, from the acquisition of raw materials to consumption, including transport and processing and are known as “well to wheel” or “cradle to grave ”LCAs.

This study proposes a quantification of the fossil energy consumption of an algae-based bioethanol. The results obtained made it possible to calculate the energy balance and to evaluate the efficiency of the production system.

II. LIFE CYCLE ASSESSMENT METHODOLOGY

The bioethanol produced in this study is based on a local green macro alga *ulva lacuca*, which is considered as a very promising source for production of liquid biofuels in the future.

The life cycle analysis of this bioethanol was carried out after the introduction of several data into the SimPro8.1 software (quantity of water, consumed electricity, used chemicals used…) using the Impact 2002+ methodology (see Fig.1).

To perform this analysis, the following assumptions were made:

- The reference unit considered in this analysis is 1 liter of bioethanol produced.
- The data are related to the harvesting, pretreatment, saccharification, fermentation and distillation stages. They concern a trial of bioethanol production at a small scale (laboratory scale) extrapolated to a medium scale to allow a comparison with other bioethanol made from other bioenergy resources.
- The processes used to model the manufacture of bioethanol were built from a trial made in Bioenergy an Environment laboratory (CDER) where 3.52 g/L of ethanol was produced after 48 h of fermentation. This was performed using commercial cellulase for saccharification and *Saccharomyces cerevisiae* for fermentation at 30 °C and pH 5, leading to a yield of 0.41 g of ethanol/g of glucose after 96 h of enzymatic hydrolysis at pH 5 and 45 °C [7].
- Macroalgae are not cultivated, the biomass needed for ethanol production is harvested from algal bloom on Algerian costs.
- The bioethanol produced is supposed to contain 5% water, it is therefore a hydrated ethanol, and the dehydration operation is not taken into account due to a lack of data related to the energy needed for this operation.
- The energy consumption related to the transport of bioethanol to the gasoline pumps, as well as the mixture with gasoline (15% of ethanol with 85% of gasoline) are not taken into consideration.
- Distillation energy consumption was taken from literature.

The data collected were entered into the SimaPro software, they allowed us to calculate the amount of fossil energy consumed during the production of algal bioethanol.

III. RESULTS AND DISCUSSIONS

a. TREE STRUCTURE OF THE ENTIRE CYCLE PRODUCTION

After entering the data into the software, we got the tree structure depicted in Fig.2.

The obtained results are shown in Table 1. Thus, the production of 1 liter of bioethanol from algae necessitates 14.719 MJ of nonrenewable energy. Results also show that the fermentation step is the most consuming step of the entire cycle with 6,525 MJ, which corresponds to 44.3 % of total energy consumption.

Indeed, fermentation requires an important intake in electricity and water, high-energy consumption is due to the long period of fermentation (96 h), and the temperature (30°C) needed by saccharomyces cerevisiae to ensure an effective fermentation and a high yield in ethanol.

Saccharification step is responsible of 29.5 % of the total energy consumption, corresponding to 4.34 Mj , it is mainly due to the high temperature (40° C) needed to hydrolyze cellulose into glucose even if the saccharification duration (48 h) is relatively short compared to that of fermentation.

Table 1
Data used for Energy balance of algal bioethanol production

Type of input	Nomenclature	Unit	Quantity
	Biomass preparation		
Biomass (Macroalgae)	[7]	Kg	25.5
Energy	Manual Harvest	kwh	0
Transportation	Biomass by car	km	14.5
Water	Tap water	L	12
	(Used water for washing and desalination) [7]		
Energy	Drying	kwh	0
	(air drying)		
Energy	Milling	Kwh	0.08 kwh
	Calculated from grinder electric consumption for 30 min		
	Pretreatment		
Chemicals	Sulfuric acid [7]	ml	25
Energy	Autoclaving	Kwh	0.245
	Calculated from autoclave electric consumption 20 min at 120°C		
	Saccharification		
Enzymes	Celluclast [7]	ml	55
Energy	Electricity, medium voltage (DZ) natural gas burned in gas turbine	kwh	0.350
	Calculated from shaker electric consumption at 40°C during 48h		
	Fermentation		
Microorganism	Saccharomyces cerevisiae [7]	g	50
Water	Tap water [7]	L	14
Chemicals	$(NH_4)2HPO_4$ [7]	g	18.5
Energy	Electricity, medium voltage (DZ) natural gas burned in gas turbine	kwh	0.523
	Calculated from shaker electric consumption at 30° C during 96 h kwh		
	Distillation		
Energy	Electricity, medium voltage (DZ) natural gas burned in gas turbine [7]	kwh	0.132

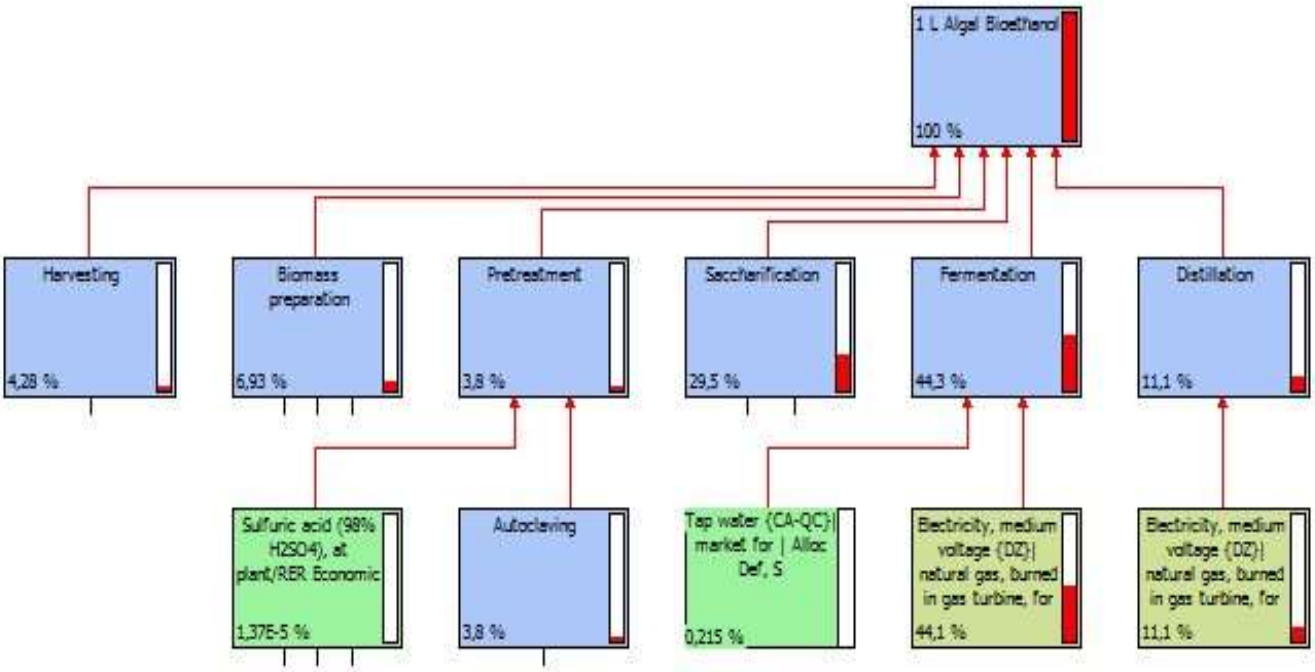

Fig. 1: life cycle steps of third generation bioethanol production

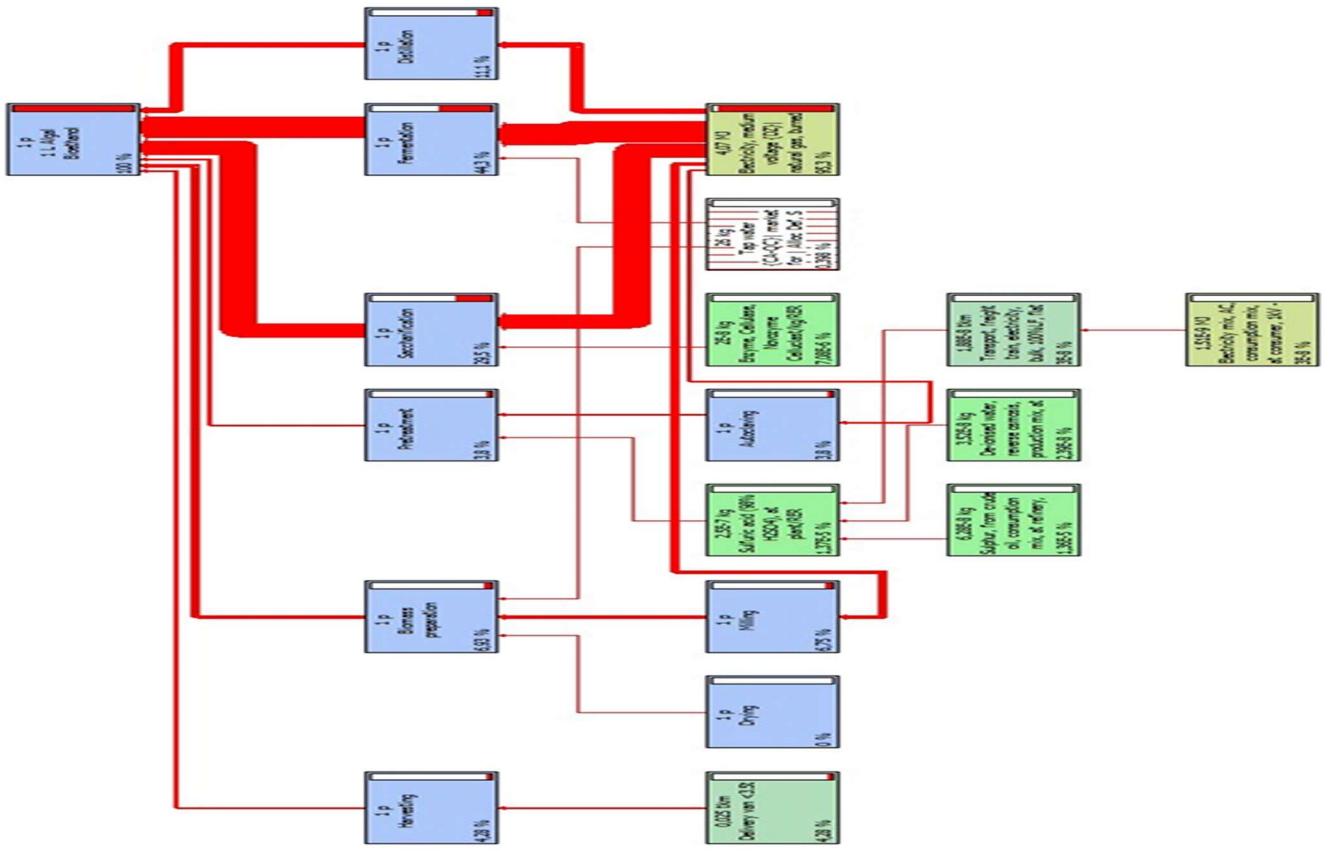

Fig. 2: Tree structure of third generation ethanol production

Table 2
Energy consumption during each algal bioethanol production step

Production steps	Non-renewable energy consumption Mj	Non-renewable energy consumption %
Biomass preparation	1,020	6.93 %
Harvesting	0,629	4.28 %
Pretreatment	0,558	3.5 %
Saccharification	4,346	29.5 %
Fermentation	6,525	44.3 %
Distillation	1,639	11.1 %
Total	14,719	100 %

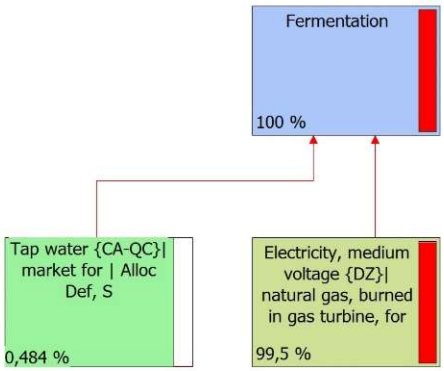

Fig. 3: Nonrenewable energy consumption during fermentation

Distillation is known to be the most consuming step of energy in bioethanol production, it can reach 60% of total consumption, when the dehydration step leading to a concentration of 99.7% ethanol is required. This step was not achieved in this study and the energy consumption was only 11.1 % of the total energy consumption, while a concentration of 95% was achieved which meets the bioethanol specifications as a gasoline fuel additive [9].

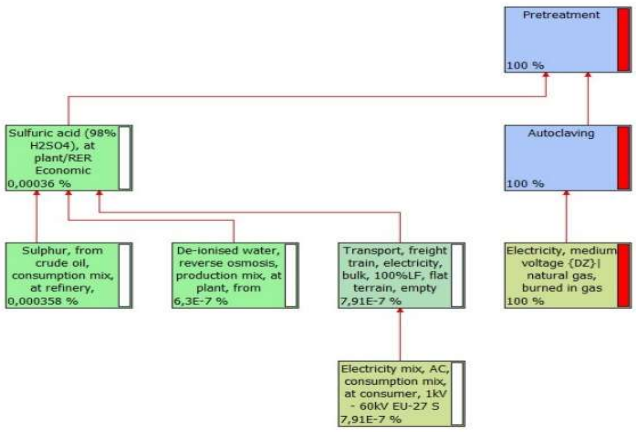

Fig. 4: Nonrenewable energy consumption pretreatment

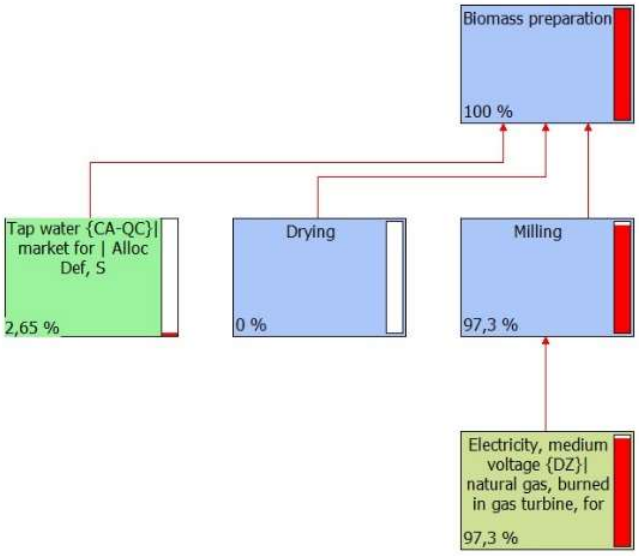

Fig. 5: Nonrenewable energy consumption during biomass preparation

Biomass preparation, harvesting and pretreatment are the less nonrenewable energy consuming steps of the process with 6.93 %, 4.28 %, and 3.5 % of the total energy consumption respectively. Indeed, important amounts of energy were saved by reducing transportation to the minimum, promoting solar drying, reducing the use of acids for pretreatment (acid makes algal sugars more accessible to enzymes) and water for desalination to the lowest possible guaranteeing good results in terms of energy saving.

b. ENERGY BALANCE

The energy balance was calculated according to the following equation:

Energy balance = Energy produced in the form of biofuel/ consumed Energy

- Produced Energy = PCI (lower calorific value of bioethanol) = 21.3 MJ/L[10]
- The energy consumed is equal to 14.719 MJ/L of bioethanol produced (given by the SimaPro 8.1 software)

Thus, the energy balance of algae-based bioethanol is equal to 21.3/ 14.719 = 1.44

The energy balance of algal bioethanol shows a good energy efficiency compared to other types of bioethanol produced from other substrates (Table 3). Indeed, the energy produced is 1.44 times higher than the energy consumed.

▪ Reduction of energy consumption related to the transport of biomass.

▪ Elimination of the dehydration step responsible for 30% of the energy consumption.

▪ The limitation of water supply specially during desalination of algae.

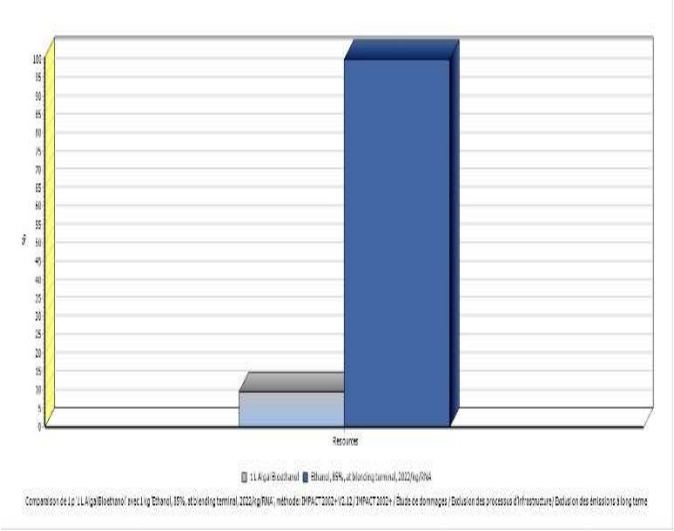

Fig. 6: Energy consumption comparison of algal ethanol and E85 (15 % ethanol, 85% gasoline)

Compared with (15 % ethanol, 85% gasoline), third generation ethanol made from macroalguae present an energy saving of 85 %. [11]

c. COMPARISON OF THE ENERGY BALANCE OF ALGAL BIOETHANOL WITH THAT OF OTHER ENERGY CROPS

SimaPro 8.1 software with its rich database allows us to compare non-renewable energy consumption and energy balance of algal bioethanol with other bioethanol made from other substrate: switchgrass, cornstover, forest residues.

Table 3
Comparison of the energy balances of several bioethanols

Production steps	**Non-renewable energy consumption Mj**	**Energy balance**	**Reference**
Algal bioethanol	14.71	1.44	Present study
Sugar beet ethanol	7.1	3	12
Corn stover bioethanol	14.77	1.44	13
Switchgrass bioethanol	14.37	1.48	14
Forest residues bioethanol	1210.66	0.017	15

Table 3 shows that the energy balance of algal bioethanol is comparable to bioethanols made from conventional substrates such as corn stover or switchgrass, it is lower than that sugarbeet bioethanol and higher than forest residue bioethanol that consumes more energy than it produces.

II. CONCLUSION

Biofuels produce and consume energy, reduce and emit greenhouse gas. Their economic and ecological impacts can be actually measured only by life cycle analyses that allow to establish precise energy and carbon balance. This study removes the uncertainty that hangs over the interest on third generation biofuels specially bioethanol whose production still need to be improved to be competitive, since it demonstrated that algae-based bioethanol produces 1.44 times more energy than its production consumes. Moreover, the main advantages of algae based bioethanol over other alternative bioethanols lie in the fact you do not need arable land to produce it. There is no competition with food and most of all the yields in bioethanol are very much higher, even if, many challenges must be taken up to make large-scale ethanol production possible and economically viable.

REFERENCES

[1] Rapport published by Oligae: Energy from Algae: Products, Market, Processes and Strategies (www.oilgae.com), Feb. 2011.

[2] T. Mata, A. Martins, N. Caetano. Microalgae for biodiesel production and other applications: a review. Renew. Sustain. 14, 217–232. 2010. DOI: 10.1016/j.rser.2009.07.020

[3] R. Harun, M. Danquah, G. Forde. Microalgal biomass as a fermentation feedstock for bioethanol production. 2010. J. Chem. Technol. Biotechnol., 85, 199 (2010). DOI: 10.1002/jctb.2287

[4] P. Rojan, A. John, G. Anisha, K. Madhavan, P. Ashoc. Micro macroalgal biomass: A renewable source for bioethanol. Institut National de la Recherche Scientifique-Eau Terre Environnement, Micro and macroalgal biomass: A renewable source for bioethanol, Bioresour. Technol., 102,186 (2011), DOI: 10.1016/j.biortech.2010.06.139

[5] Rapport Scientifique de WWF World Wide Fund, 'Conifères Méditerranéens et les Forêts Mixtes', 2008.

[6] J. Caliez et L. Nguyen, 'Les Biocarburants', Synthèse faite d'après le Rapport 'Les Biocarburants' de P. Sadones, publié dans EDEN 2006

[7] A. Allouache, A. Majda, A. Z. Toudert, A. Amrane, M. Ballesteros, cellulosic bioethanol production from ulva lactucamacroalgae. Cellulose Chem. Technol., 55 (5-6), 629-635(2021). DOI: 10.35812/CelluloseChemTechnol.2021.55.51.

[8] A. Dauriat and N. Jungbluth, 'Ethanol, 95% in H2O, from Sugar Beet Molasses, to distillery,kg/CH, Life Cycle Inventories of Bioenergy', Data Base SimaProEcoinvent UnitProcess, Vol. 28, N°2, 2008.

[9] C. Fargues, R. Lewandowski, M.L. Lameloise, 'Evaluation of Ion-Exchange and AdsorbentResins for the Detoxification of Beet Distillery Effluents', Industrial and Engineering Chemistry Research, Vol. 49, N°19, pp. 9248 – 9257, 2010. DOI: 10.1021/ie100330y.

[10] A. Dauriat, 'Le Bioéthanol', Rapport Publié par ENERS Energy Concept, Lausanne –www.eners.ch. 2003.

[11] Garvin Heath. Life cycle assessment of ethanol 85 % at blending terminal/kg. NREL. USA. 2011. From SimaPro 8.1 database 2022.

[12] J.S. Yuan, K.H. Tillier, H. Al-Ahmad, NR. Stewart, Jr.N.C. Steward, 'Plants to Power: Bioenergy to Fuel the Future', Trends Plant Science. Vol. 13, N°8, pp. 421 – 429, 2008. DOI: 10.1016/j.tplants.2008.06.001

[13] Daniel Inman, Life cycle assessment of ethanol from corn stover dry mill/kg. NREL. USA. 2013. From SimaPro 8.1 database 2022.

[14] Daniel Inman, Life cycle assessment of ethanol from switch grass/kg. NREL. USA. 2015. From SimaPro 8.1 database 2022.

[15] Daniel Inma, Life cycle assessment of ethanol from forest residues thermochemical/kg. NREL. USA. 2016. From SimaPro 8.1 database 2022.

Amina Allouache was born in Algiers, Algeria, in 1986. She received the Engineer Diploma degree from Université Des Sciences et Technologies Houari Boumediene (USTHB), Algiers, in 2009, the Master degree from Ecole Nationale Polytechnique, Algiers, in 2012. She is currently a Researcher in Centre De Developpement Des Energies Renouvelables (CDER) and Phd student at Ecole Nationale Polytechnique. Her current research interests include the production of bioethanol, seaweed characterization and life cycle assessment.

Majda Amina Aziza is Director of Research, and head of Bioenergy and Environment Research Division, at the Research Centre on Renewable Energy, in Algiers. She received her doctorate in chemistry, in 2006, from University of Rennes 1, France, and her engineer and master degrees in agronomical sciences,in 1996 and 2000, respectively, from Algerian Institute of Agronomy.
Most of Dr. Aziza's papers and reports deals with issues related to microorganisms cultures improvement on bioreactors, biofuels production and food technology.

Toudert AHMED ZAID, born on August 15, 1954 in Ain El Hammam (TiziOuzou), is Professor at the Chemical Engineering Department, Ecole Nationale Polytechnique, Algiers. He has an experience of 20 years in the domain of surfactants and dispersed systems. He has authored or co-authored more than thirty papers mainly in this research area.

Mohammed Amouri was born in Chlef, Algeria in 1984. He received the Engineer Diploma degree from Université Ibn Khaldoun, Tiaret, the Master and Phd degree from Ecole Nationale Polytechnique, Algiers, in 2012 and 2019 respectevly. He is currently a Researcher in Centre De Developpement Des Energies Renouvelables (CDER). His current research interests include the production of biodiesel, life cycle assessment and microalgae culture.

Correlations between Physico-Chemical Properties and Dielectric Behavior of Thermally aged XLPE Cables Insulation

Yasmina Sebbane, Ahmed Boubakeur, and Abdelouahab Mekhaldi

Abstract−The carried out investigations aim at clarifying the correlations between physico-chemical properties and the variation of dielectric losses of Cross-Linked Polyethylene (XLPE) as Medium Voltage cable insulation during thermal aging. The used cables were manufactured by ELSEWEDY CABLES. They have been installed in Algeria where they must resist high temperatures that could exceed 50 degrees in the south of the country. For this aim, thermal aging measurements were performed on XLPE cables samples at 80, 100 and 140 °C for aging time of 5000 hours. The chemical properties were evaluated through Fourier Transform Infrared Spectrum (FTIR). In addition, the effect of aging on the crystallinity ratio, the lamellar thickness and the melting peak temperature was assessed using Differential Scanning Calorimetry (DSC). Frequency domain dielectric spectroscopy has been conducted on the aged XLPE cables in order to study the evolution of the dielectric losses. The obtained results showed that the principal aging mechanism is thermal oxidation which heads to deteriorate the morphology and increase both the polarization and losses, principally at low frequencies. It has been found that the color changes caused by the chains scission indicate the increase of interfaces between the cable insulating and semi-conductive layers, which could head to increase the dielectric losses due to the interfacial polarization.

***Keywords*− Cross-linked Polyethylene, Cristallinity, Thermal aging, Dielectric losses.**

I. Introduction

The Cross-linked polyethylene (XLPE) is used as an electrical insulating material in underground and transmission and distribution cables, due to its prime dielectric strength, low dielectric permittivity and losses factor [1]. Therefore, cross-linked polyethylene (XLPE) remains a material of choice for medium and high-voltage cables [2]. It has also a high operating temperature of about 90 °C [3]. However, it is now understood that irreversible changes may happen after the exposure of the cable to severe environmental conditions. The thermal constraint considered as the most impacting factors leading to irreversible chemical and/or morphological changes that affect the properties of XLPE, and produce a limit to the effective service life of the power cables [4].To address these issues, many researchers have focused on the relationship between structural changes and dielectric strength of cables insulation under thermal oxidative aging [5, 6]. These studies showed that the dielectric parameters (dielectric losses factor and dielectric permittivity) are completely linked with the physical, chemical and structural changes of XLPE insulation occurring during service or accelerated testing [7]. However, further research is needed on the dielectric behavior of the aged cables.

This paper aims to evaluate the Physico-chemical and dielectric properties of the cable insulation samples before and after aging to investigate the degree of XLPE degradation. Besides, we aim to study the correlations between these different properties, leads to elucidate aging and degradation mechanisms.

Manuscript received June 30, 2022; revised July 27, 2022.

Y. Sebbane, A. Boubakeur and A. Mekhaldi are with Ecole Nationale Polytechnique
(e-mail: yasmina.sebbane@g.enp.edu.dz, ahmed.boubakeur@g.enp.edu.dz, abdelouahab.mekhaldi@g.enp.edu.dz).

Digital Object Identifier (DOI): 10.53907/enpesj.v2i1.102

II. Setup of Experiments

A. Samples preparation and thermal aging procedure

Taking into account the dimensions of the ovens intended for the thermal aging, it was therefore necessary to prepare cables samples into 0.5 m long segments. Fig 1 shows the dimensions of the tested XLPE cable samples.

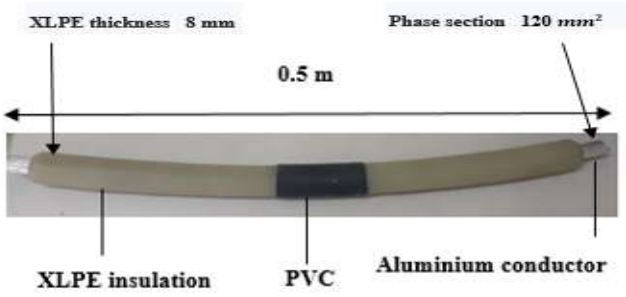

Fig 1: Dimensions of the tested XLPE cable samples.

Samples of 18 kV XLPE cable furnished by Elsewedy Cable were cut into 0.5 m in length taken as specimens for thermal aging tests. The samples consist of XLPE insulation (thickness~8mm).

The choice of the test temperatures derives from cable design and the need to obtain thermal degradation in a rational time. The maximum temperature assigned to conductive core of the cable in steady conditions is 90 °C. Also, higher temperatures are allowed in Short-circuit conditions (up to 250 °C) according to the cable technical sheet. All cable samples were aged in an air oven at three of aging temperature 80°C, 100°C and 140°C. Aging time of 5000 hours was selected for two level of temperatures 80°C and 100°C.While 1500 hours were used for 140°C.

B. Analytical measurement

B.1. FTIR spectroscopy measurements

The chemical properties brought about in XLPE insulation after the degradation generated by thermal aging were analyzed by a spectrometer (FTIR spectrum two 100302) with PerkinElmer software.

The XLPE films for FTIR analysis were cut up longitudinally on a slitting machine. In this method, the insulation layer of the cable was sliced into thin wedges to form a loop, as shown in Fig 2.

Fig 2*:* Cutting of cable insulation.

B.2 .DSC measurement

DSC analysis was performed using PERKIN ELMER PYRIS device under nitrogen gas flow.

B.3. SEM analysis

We analyze the surface morphology of aged and unaged XLPE samples by Scanning Electron Microscopy (SEM) using SU-8230 Electron Microscope.

To obtain smooth surfaces, we immerse the aged and unaged samples in a liquid Nitrogen bath at a temperature of -30°C, and then we cut them using a LeicRM2265 microtome.

B.4. Dielectric measurement

Two sets of devices were put for the characterization of the cables samples.

B.4.1. Dielectric spectrometer

The dielectric measurement (dielectric losses factor tanδ) was performed with the Broadband Dielectric Spectroscopy (BDS) using a spectrometer Type Novocontrol (high resolution Alpha-N dielectric analyzer) with WinDETA software. The cable samples were covered with copper tape in order to increase the surface of the electrode and reduce the connection resistance; then, the measurement was started after calibrating the device at low capacity and the measurement frequency range from 100 Hz to 1 MHz

B.4.2. Schering Bridge

The dielectric losses factor (tan δ) was measured in function of the voltage by using a Schering bridge (AG type TG-3MOD) under the ambient temperature and the frequency of 50 Hz. A test cell consisting to place the conductive core on the HV terminal of the transformer and the metal screen to earth, then gradually increase the test voltage up to the specific cable voltage, which is 18 kV. A filter containing an inductor and two parallel capacitors was used to reduce background noises and a layer of semi insulating paint was applied through the surface of the cable ends to reduce the leakage currents.

III. Experimental Results and Discussion

A. Color changes

In Fig 3, we present the obtained changes in aspect of XLPE films from cutting of cable at different aging phases. We remark that the color changed from gray before aging to light yellow after 5000 h at 80 °C, to light brown after 5000 h at 100 °C and then a dark brown after 1500 h at 140 °C.

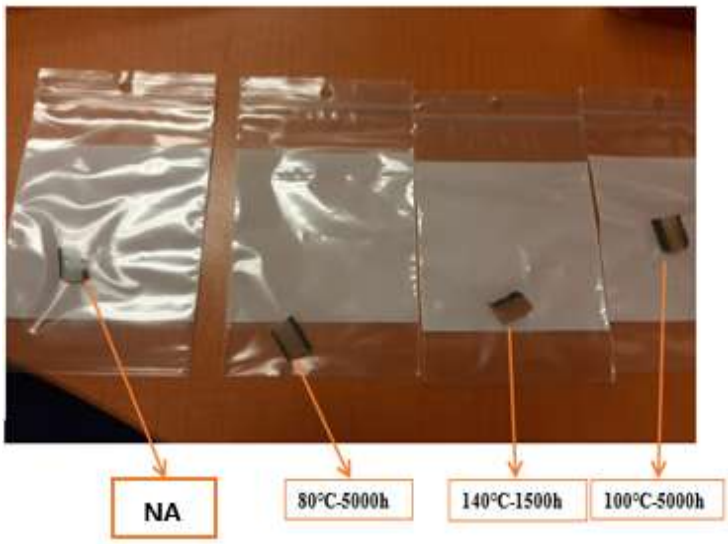

Fig 3*:* Color change of XLPE films.

These color changes have been ascribed to the formation of vinylidènes and vinyl groups caused by thermal oxidation [8, 11]. It could attribute to the antioxidant reaction during the oxidation [12].

B. FTIR spectroscopy analysis

In Fig 4, we present the FTIR spectra of XLPE samples before and after thermal aging.

The group CH_2 manifest at a wavenumber of 720 cm^{-1}, and it is affirmed by its peaks appeared at 730 cm^{-1}, 1463 cm^{-1}, 2848 cm^{-1} and 2915 *c* [13, 14].

After aging, an increase of the absorption peaks intensities in the XLPE characteristic bands (720, 1463, 2848 and 2915 cm^{-1}), could be attribute to the molecular chains scission. At the aging temperature of 140 °C we remark that the formation of C=O carbonyl groups and an increase of the IR absorption band between 1500 cm^{-1} and 1800 cm^{-1}.In addition, the C=C bond of the vinylene group responsible for the color change can be found between 1560 $cm^{-1}$and 1600 cm^{-1} [15]. Moreover, a slight increase in the absorption of the -OH function of the hydroxyl groups could be observed after aging in the region between 3000 and 3500 cm^{-1} [16]. The significant increase of the carbonyl groups observed in the case of the aging temperature of 140°C. It is known in the literature that at the temperatures higher than the melting point of XLPE (105 °C) ease the oxygen diffusion between the macromolecular chains, which led to accelerate thermo-oxidative reactions.

The acceleration of chemical reactions after thermal aging, the aging rate can be supposed proportional to the rate of chemical reactions. It can easily be anticipate that the thermo-oxidation phenomenon in the thermally aged XLPE cables may influence their dielectric behavior.

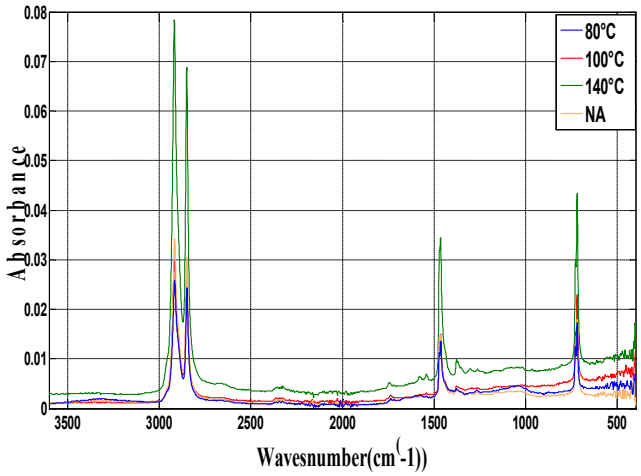

Fig 4: FTIR spectrum of XLPE samples plotted in different ranges after 5000 hours for the aging temperatures of 80°C, 100°C and after 1500 hours for the aging temperature of 140°C.

Enlargements of various partial spectral ranges of Fig 4 are presented in Fig 5, 6 and 7.

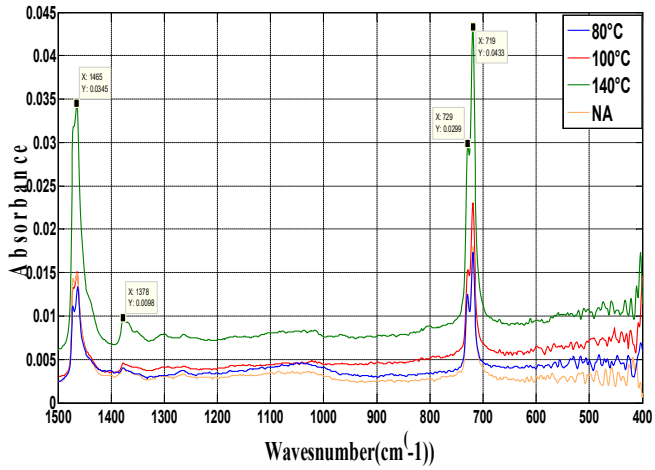

Fig 5: Partial FTIR spectrum from 400 to 1500 cm^{-1}.

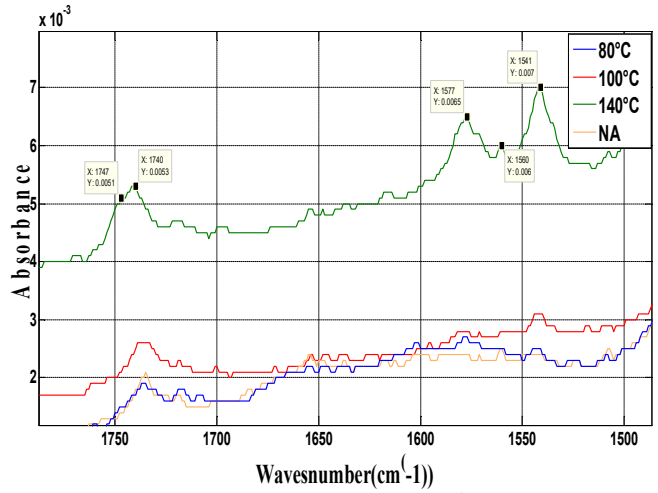

Fig 6: Partial FTIR spectrum from 1500 to 1750 cm^{-1}.

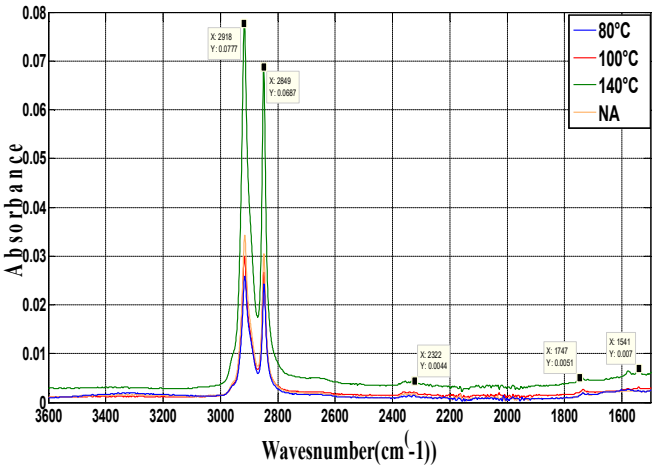

Fig 7: Partial FTIR spectrum from 1600 to 3600 cm^{-1}.

C. *SEM analysis*

Fig 8 show the micrographs of unaged and aged XLPE samples at aging temperatures of 80°C, 100°C and 140°C, using Energy Dispersive Spectroscopy technique.

The SEM micrographs show many micro-cracks on the XLPE surface after thermal aging. These micro-cracks are more accentuated when the aging temperature increases; therefore, the unaged XLPE has a smooth surface. We also notice that these cracks take the form of needles which appear on the surface of the thermo-oxidized material at all aging temperatures 80°C, 100°C and 140°C [17].

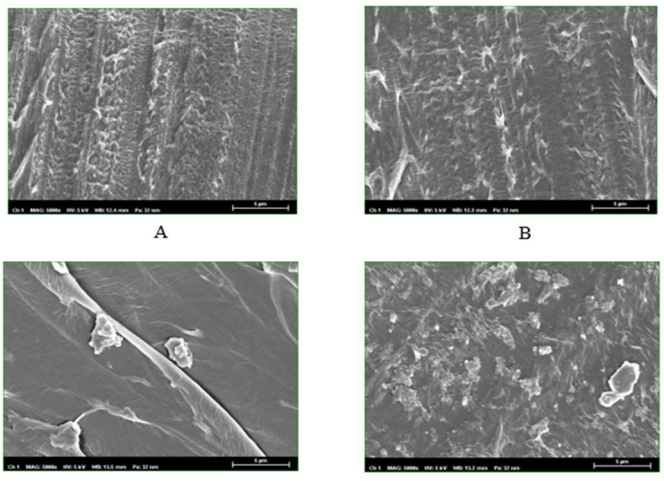

Fig 8: SEM-EDS micrographs of the samples.(A) NA, (B) Aged at 80°C for 5000 h ,(C) Aged at 100°C for 5000 h ,(A) Aged at 1400°C for 1500 h.

D. *DSC Results*

The thermograms of the heating and cooling cycles of unaged and aged samples are presented in fig 9, 10 and 11.

The critical parameters are listed in Tables 1 and 2, where T_C is the crystallizing peak temperature, T_m is the melting peak temperature, and χ (%) is the crystallinity ΔH_m is the melting enthalpy and ΔH_c is the crystallization enthalpy.
The lamellar thickness was calculated based on Thompson-Gibbs equation as follows [13]:

$$T_m = T_{m0}\left(2\sigma_e / \Delta H_m \cdot L\right) \quad (1)$$

Where L is the lamellar thickness; σ_e is the surface-free energy per unit area of basal face; ΔH_m is the melting enthalpy of an ideal polyethylene crystal per unit volume T_{m0} is the equilibrium melting temperature of an infinitely thick crystal. The values used for calculation were as follows [13]: $\Delta H_m = 2.88 \times 10^8 J.m^{-3}$ $T_{m0} =$ 414.6 K, and $\sigma_e = 93 \times 10^{-3} J.m^{-2}$.

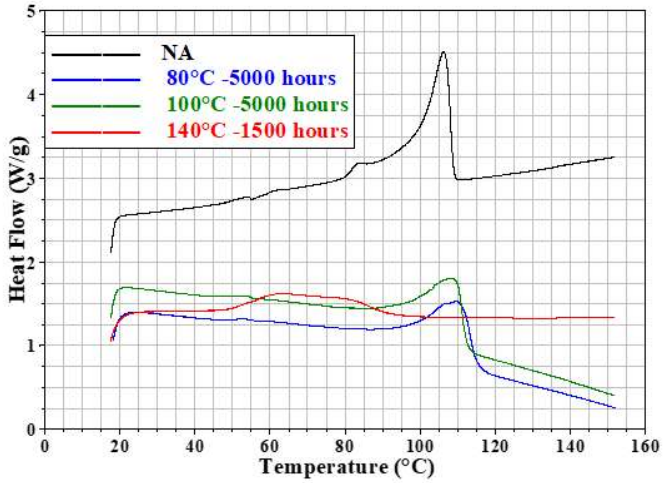

Fig 9: DSC heating thermograms of unaged and aged samples (first heating cycle).

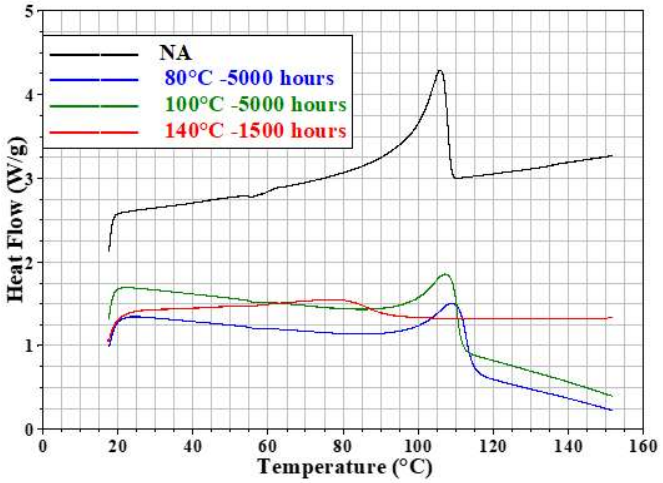

Fig 10: DSC heating thermograms of unaged and aged samples (second heating cycle).

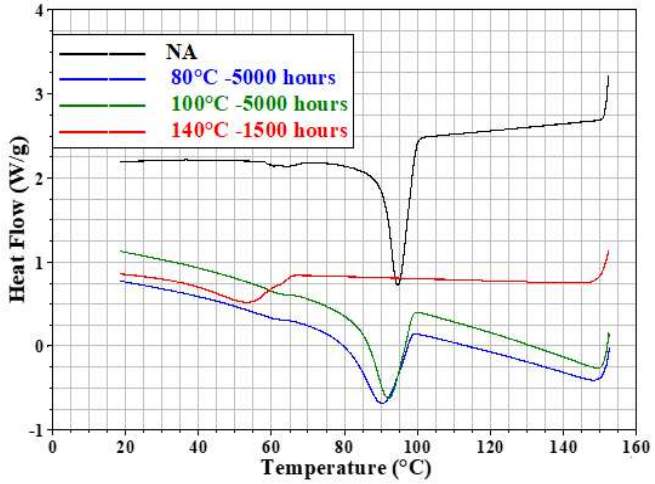

Fig 11: DSC heating thermograms of unaged and aged samples (first cooling cycle).

Table I
RESULTS OBTAINED FROM DSC MEASUREMENTS (First cycle)

Parameters	NA	80°C-5000 h	100°C-5000 h	140°C-1500 h
T_m(°C)	106.26	111,36	109.04	63.99
T_c(°C)	94.59	92.65	92.08	53.48
ΔH_m(J. g^{-1})	95.42	94,29	56.45	41.98
ΔH_c(J. g^{-1})	-108	-92.73	-57.9	-42.66
X (%)	33.21	32,81	20.00	17.04
L (mm)	70,60	69,60	70.00	41.83

Table II
RESULTS OBTAINED FROM DSC MEASUREMENTS (Second cycle)

Parameters	NA	80°C-5000 h	100°C-5000 h	140°C-1500 h
T_m(°C)	105.93	110.57	107.00	78,77
T_c(°C)	94.58	92.66	92.06	52.99
ΔH_m(J. g^{-1})	86.41	86.80	40,50	27.16
ΔH_c(J. g^{-1})	-62.70	-92.63	-55.36	-42.44
X (%)	30.07	30.21	14.00	9.40

We remark in (Fig 9) that the melting peak widens and shifts toward lower temperatures. This phenomenon is ascribed to the chain scission caused by the oxidation process at high temperatures [13].

We remark in (Fig 10) that the ridges appeared during the first heat cycle disappear.

For the cooling cycle (Fig 11), we remark that at the aging temperature of 140°C the depression in crystallization temperature suggests that the cable sample underwent severe deterioration, due to the chain scission [13].

We can distinguish two phase according to the aging temperatures. The first one matches to aging temperatures below the melting point (80 and 100 °C) where the oxidation mainly affects the amorphous regions. However, oligomers could seem in the amorphous regions due to the chain scission. These latter crystallize. This is named as a post-cross-linking phenomenon [18]. The second phase matches to the higher aging temperatures (140 °C), the oxygen diffusion is accelerated and the crystalline parts disappear [18].

E. Dielectric behavior

To study the correlation between the dielectric behavior of the thermally aged XLPE cables and the physico-chemical changes, the samples aged at 80°C, 100°C and 140°C were taken to measure their dielectric losses factor, in the frequency range from 10 Hz to 300 kHz and in the voltage from 5kV to 18kV.

Fig 12 presents the plot of tanδ versus frequency for the unaged and aged XLPE cable samples of thermal aging at 80°C.100°C and 140 °C in the range from 10 Hz to 300 kHz.

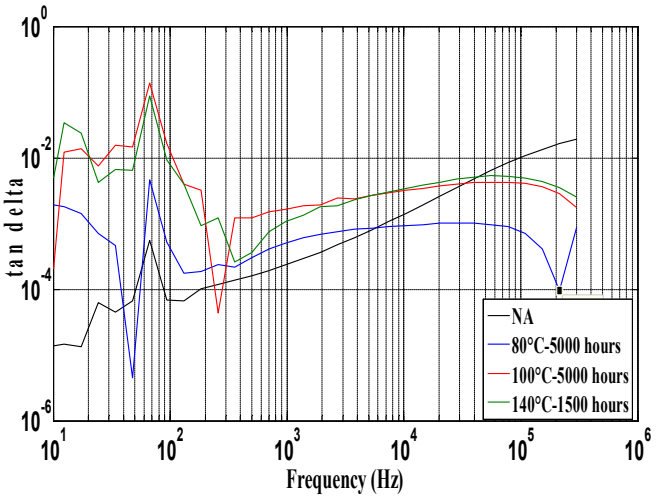

Fig 12 : Plot of tanδ versus frequency for the unaged and aged XLPE cable specimens at 80°C.100°C and 140 °C in the range from 10 Hz to 300 kHz.

Enlargements of various partial plot frequencies ranges of Fig 12 are presented in Fig 13, 14 and 15.

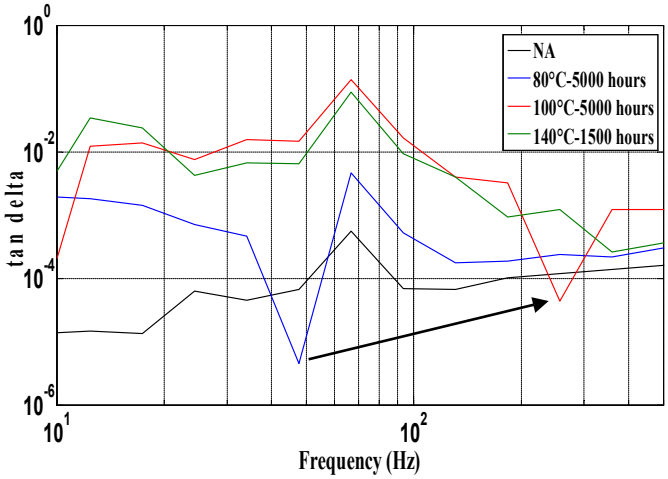

Fig 13: Tan delta versus frequency in the range from 10 Hz to 500 Hz.

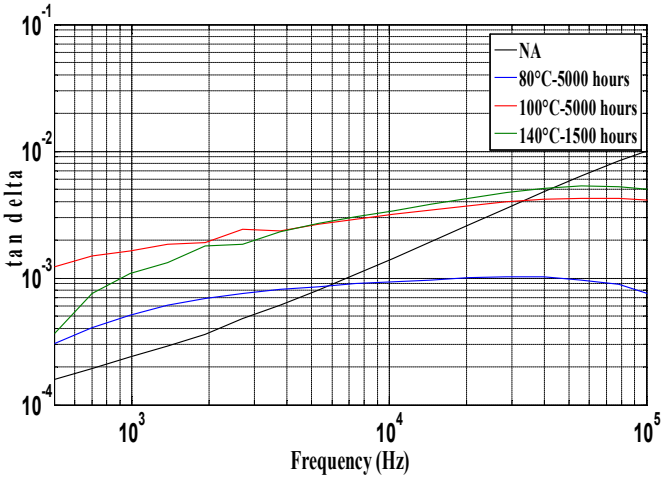

Fig 14: Tan delta versus frequency in the range from 500 Hz to10 kHz.

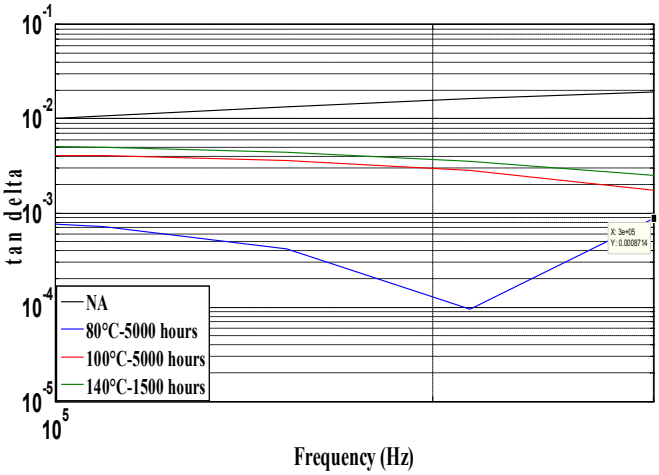

Fig 15: Tan delta versus frequency in the range from 10 kHz to 300 kHz.

We remark from the Fig 12 that dielectric losses factor of the thermally aged cable samples in the frequency ranging from 500 Hz to 10 kHz becomes higher with the aging temperatures and the fast decrease of tanδ in the frequency range between 100 kHz and 300 kHz.

We observe in Fig 13 that a dielectric losses peak appears in the frequency domain from 10 Hz to 500 Hz. As the aging temperatures becomes higher, the dielectric losses peak make higher and its position shifts to the higher frequency region.

The higher peaks of the dielectric losses factor of the cable samples aged at 100°C for 5000 hours and 140°C for 1500 hours can be due to its carbonyl groups confirmed by FTIR results and the displacement of the dielectric losses peak towards high frequencies (as indicated by arrow Fig 13) could be attributed to the morphology of the material (Fig 8) [19]. The change of the XLPE color seems to indicate the effect of increasing the interfacial zones between XLPE insulation and semi conductive layers and then promoting the interfacial polarization.

According to the reference [20] the presence of relaxation peak reveals the existence of several absorption bands. The dielectric losses peak in the frequency domain from 10 Hz to 500 Hz may be related on the one hand, to the presence of the interfaces (interfacial polarization) between XLPE insulation and semi conductive layers, on the other hand, to the thermo oxidation.

Mecheri and *al* [21] showed that the rapid decrease in the dielectric losses factor can be probably caused by the improvement of the crystal morphology of the XLPE and the volatilization of the crosslinking. For example, as confirmed in our DSC results, the thickness of the crystalline lamella remains practically the same compared to that of the sections of not aged cables (for the aging temperature of 80°C the thickness is 69.6 mm and for not aged cable it is 70.6 mm).

It is known, tanδ is strongly influenced by the oxidation phenomenon in the case of Polyethylene [22]. Therefore, the tanδ depends on the losses polarization such as dipole polarization [23].The increase of tanδ can be attributed to the formation of electrically asymmetric carbonyl compounds due to the oxidation, these later are the mainly factor in increasing of dielectric losses [24].

This dielectric behavior may be ascribed to the presence of the carbonyl groups confirmed by FTIR analysis and the spatial charges due to the thermo-oxidation in the XLPE insulation [7].The increase in dielectric losses factor for a not aged sample cable in overall frequency range is due to the ohmic effect.

Fig16 presents plot of tanδ versus voltage levels for the unaged and aged XLPE cable specimens at thermal aging of 80°C, 100°C and 140°C in the range from 5kV to 18 kV.

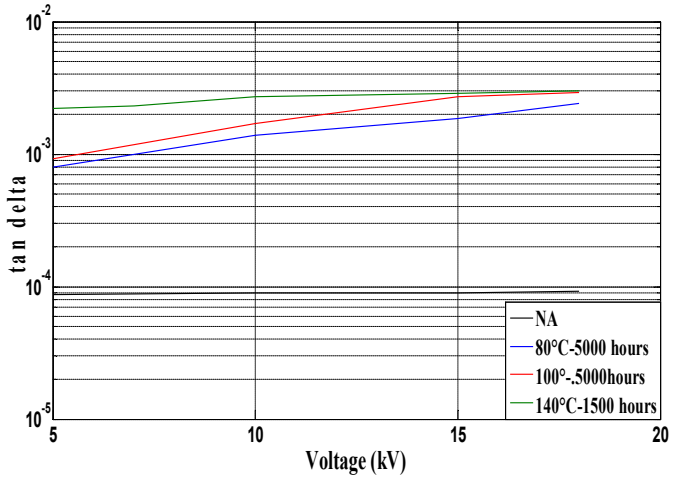

Fig 16: Plot of tanδ versus voltage levels for the unaged and aged XLPE cable specimens at 80°C, 100 °C and 140°C in the range from 5kV to 18 kV.

We remark in Fig 16 that the tanδ increases with respect to voltage levels and this increase is accentuated when the aging temperature increases.

The increase is attributed to the losses caused by partial discharges occurring in the material [24].The tanδ increase can be attributed to the great mobility of charge carriers. According to [25], thermo-oxidation plays a predominant role by the formation of polar groups and the chain scission lead to a decrease in the viscosity of the polymer and then, polar groups promote the mobility of charge carriers.

Tanδ increases considerably from a voltage level of 15kV which would be the ionization threshold, at beyond which partial discharges arise in the material yielding significant dielectric losses [26].

IV. Conclusion

In this paper, we have investigated the evolution of thermal, chemical, morphological and dielectric behaviors of XLPE MV cables insulation under thermal aging. The obtained results led to the main conclusions listed as below:

- The experimental results suggest that dielectric losses factor is strongly responsive to thermal aging effects and that it can be contemplated as a diagnostic parameter for guessing the degree of thermally aged XLPE cables deterioration,
- FTIR characterization results show that the chemical degradation is accompanied by the generation of polar groups like that carbonyl and hydroxyl groups,
- The color change of XLPE to dark brown may throw back the beginning of the material deterioration. This change is ascribed to the formation of vinylidene and vinyl groups,
- The low frequencies range seems more adequate for assessing the advanced degradation of XLPE cables samples,
- At low frequencies , the interfacial polarization due to the space charge accumulated between the XLPE insulation and the semi-conductive layer is the origin of dielectric losses,
- The color changes that show an increase of interfaces in the material could conduct to an increase of the dielectric losses,
- Micrographs obtained by the SEM analysis show that the deterioration of the dielectric properties is directly related to the thermo oxidation phenomenon,
- DSC results show that the recrystallization of many parts of XLPE leads to enhance the thermal and dielectric properties for the aging temperature of 80°C.

References

[1] T. Liu, “Dielectric Spectroscopy of Very Low Loss Model Power Cables,” PhD dissertation, Dept. of Eng., University of Leicester, England, Feb. 2010.

[2] G. Teyssedre and C. Laurent, “Advances in High-Field Insulating Polymeric Materials Over the Past 50 Years,” IEEE Electr. Insul. Mag., vol. 29, no.5, pp. 26-36, Oct. 2013.

[3] I. A. Metwally, “The Evolution of Medium Voltage Power Cables,” IEEE Potentials., vol. 31, no. 3, pp. 20-25, May. 2012.

[4] M. Nedjar, ““Effect of thermal aging on the electrical properties of crosslinked polyethylene,” J. Appl. polymer Sci., vol. 111, no. 4, pp. 1985-1990, Feb. 2009.

[5] W. Zhan, et al. "Study on aggregation structure and dielectric strength of XLPE cable insulation in accelerated thermal-oxidative aging." *Proceedings of the CSEE,* vol. 36, no. 17, pp. 4770-4778.2016.

[6] S. Nakamura, T. Ozaki, N. Ito and J. Kawai, "Change of dielectric property with water-treed region." IEEE Trans. Dielectr. Electr. Insul. vol. 9, no 3, pp. 329-334.

[7] C.Kim, et al. "Investigation of dielectric behavior of thermally aged XLPE cable in the high-frequency range." *Polymer testing,* vol. 25, no. 4, pp. 553-561,2006.

[8] J. Li, H. Li, Q. Wang, et al, “Accelerated inhomogeneous degradation of XLPE insulation caused by copper-rich impurities at elevated temperature,” IEEE Trans. Dielectr. Electr. Insul.vol. 23, no. 3, pp. 1789-1797, Jun. 2016.

[9] C. C. Zhang, Y. F. Li, M. Y. Hu, F. L. Ma, H. Zhao and B. Z. Han, “Conductivity properties of XLPE insulation used for HVDC cable after accelerated thermal aging,” 12th Inter. Conf. Prop. Appl. Dielect. Mater. (ICPADM), Xi'an, 2018, pp. 500-503.

[10] Guide for the determination of thermal endurance properties of electrical insulating materials. Part 1: General guidelines for aging procedures and evaluation of test result, IEC Standard 60216, 1991.

[11] Y. Kemari, A. Mekhaldi and M. Teguar, “Experimental investigation and signal processing techniques for degradation assessment of XLPE and PVC/B materials under thermal aging,” IEEE Trans. Dielectr. Electr. Insul. vol. 24, no. 4, pp. 2559-2569, Sep. 2017.

[12] G. Teyssedre and C. Laurent, “Semi-quantitative analysis of photoluminescence in thermoelectrically aged cables: I-identification of optical signatures,” IEEE Trans. Dielectr. Electr. Insul. vol. 16, no. 4, pp.1180-1188, Aug. 2009.

[13] L. Boukezzi, A.Boubakeur. C.Laurent, “Observations on structural changes under thermal ageing of cross-linked polyethylene used as power cables insulation,”*J. Iranian polymer*, vol. 17, no. 8, pp.611-624, 2008.

[14] E. Gaudichet-Maurin, F. Thominette, J. Verdu, “Water sorption characteristics in moderately hydrophilic polymers, Part 1: Effect of polar groups concentration and temperature in water sorption in aromatic polysulfones,” *J. Applied Poly*mer Science, vol.109, no.5, pp. 3279-3285, 2008. DOI: 10.1002/app.24873

[15] Y. Liu, H. Liu, L. Yu, Y.LI and L.Gao “Effect of thermal stress on the space charge distribution of 160 kV HVDC cable insulation material,” IEEE Trans. Dielectr. Electr. Insul. vol. 24, no. 3, pp. 1355-1364, Jun.2017. DOI: 10.1109/TDEI.2017.006196

[16] A. M. Nobrega, M.L.B. Martinez and A.A. A. de Queiroz, “Investigation and analysis of electrical aging of XLPE insulation for medium voltage covered conductors manufactured in Brazil,” IEEE Trans. Dielectr. Electr. Insul. vol. 20, no. 2, pp. 628-640, Apr. 2013.

[17] G. C. Montanari, “Chemical, Physical and Microstructural Properties of Thermally Aged Cables Models” IEEE International Symposium on Electrical Insulation, pp. 764 -768, 1988.

[18] B. Ouyang, H. Li, X. Zhang, S. Wang and J. Li, “The role of microstructure changes on space charge distribution of XLPE during thermooxidative aging,” IEEE Trans. Dielectr. Electr. Insul. vol. 24, no. 6, pp. 3849-3859, Dec. 2017. DOI: 10.1109/TDEI.2017.006523

[19] Y. Kemari, A.Mekhaldi, G. Teyssèdre and M.Teguar,. “Correlations between structural changes and dielectric behavior of thermally aged XLPE”. IEEE Trans. Dielectr. Electr. Insul. vol. 26, no. 6, pp. 1859-1866, 2019.

[20] J.C.Dubois, Plastiques, “Propreites dielectrique, Technique de lingenieur, ”A3140, pp.1-19, August, 1984.

[21] Y.Mecheri, A.Medjdoub, A. Boubakeur and M. Boumerzoug, “Influence du mode de vieillissement thermique sur les propriétés du polyéthylène

réticulé chimiquement," Annales de Chimie, Sciences Des Matériau, Lavoisier, Paris, vol.31, no.5, pp.571-582.
[22] N.Hirano et al,"Diagnosis of the aged XLPE cable using frequency and temperature characteristics of tanδ.II."21th IEEE,Symp on Elect and Insul materials,pp.179-182,Japan, Sept 26,1988,
[23] B.X.Du and J.Li, "Electrical and mechanical ageing behaviors of used heat-shirinkable insulation tubes," IEEE Trans Dielectr Electr Insul, vol. 21, pp. 1875–1881, August, 2014. DOI: 10.1109/TDEI.2014.104324
[24] A.Motori, G.C.Montarari and S.Gubanski, "Low-frequency dielectric properties for diagnosis of ageing in polymeric cables,"*J.App Polym Sci*, vol.59, pp.1715-1724, March, 1996.
[25] A. Boubakeur Y. Mecheri, M. Boumerzoug, "Influence of continuous thermal ageing on the properties of XLPE used in medium voltage cables." 12th Int Symp Hig Vol Eng, 22-27 August, 1999.
[26] J. K. Nelson, "Breakdown strength of solids," in *Engineering Dielectrics Volume IIA Electrical Properties of Solid Insulating Materials: Molecular Structure and Electrical Behavior,*ASTM International,1983

Yasmina Sabbane received the Master's and Engineer's degrees in Electrical Engineering from Ecole Nationale Polytechnique (ENP) of Algiers in 2014. She is currently a Ph.D. student at the Electrical Engineering Department at the same Engineering School.

Ahmed Boubakeur received in 1975 the degree of Engineer in electrical engineering from Ecole Nationale Polytechnique (ENP) of Algiers, and in 1979 he obtained the Doctorate in Technical Sciences from the Institute of High Voltage Engineering of the Technical University of Warsaw of in Poland. He is currently a professor at ENP of Algiers where he has been giving lectures and supervising research in the field of High Voltage Engineering since 1982. His principal research areas are discharge phenomena, insulators pollution, lightning, polymeric cables insulation, transformer oil ageing, neural network and fuzzy logic application in HV insulation diagnosis, and electric field calculation and measurement. He is an IEEE senior member, member of IEEE/DEIS and a member of the Algerian HV Power Systems Association ARELEC (National Algerian Comity of CIGRE and ENP Elders Association ADEP). He has been member of the Editorial Board and Associate Editor of IET/SMT.

Abdelouahab Mekhaldi received the degree of Engineer in 1984 in electrical engineering, the MSc degree in 1990 and a Ph.D. in high voltage engineering in 1999 from Ecole Nationale Polytechnique (ENP) of Algiers. He is currently a Professor at ENP. His main research areas are in discharge phenomena, outdoor insulators pollution, polymeric cables insulation, lightning, artificial intelligence application in high voltage insulation diagnosis and electric field calculation.